An investigation of the nature of Pc5 pulsations using SuperDARN and magnetometer data

by

Zolile Mtumela

A thesis submitted in partial fulfilment of the academic
requirements for the degree of
Doctor of Philosophy
in the School of Physics,
University of KwaZulu-Natal
Durban

05 January 2015

As the candidate's supervisor I have/have not approved this thesis for submission

Signed: ..... Name: ..... Date: .....

As the candidate's co-supervisor I have/have not approved this thesis for submission

Signed: ..... Name: ..... Date: .....

Abstract

Pc5 pulsations are global magnetohydrodynamic events in the magnetosphere. We employed an Automated Pulsation Finder program to identify significant Pc5 pulsation events in SuperDARN data. Those events for which a resonance of similar frequency band was observed in more than one HF radar were selected. The three events presented here are such that a similar resonance was observed in Goose Bay, Saskatoon and Pykkvibaer HF radars, located in the northern polar region. One event was isolated in which the resonance was observed at the conjugate hemisphere at Sanae, Antarctica. Those events have a good data from magnetometer chains within the field of view of HF radars are chosen for analysis. These two instruments complement each other. We combined these two instruments to investigate the nature of the pulsation, determining its qualitative polarization characteristics. Observations of a resonance that extend over a large fraction of the polar region are rarely reported. A complex demodulation technique was employed to determine the amplitude and phase relationship between field components observed by the radars and magnetometer chains, this in turn, affords resolution of other characteristics of pulsations such as wave number and phase velocity. We present results in a graphical form and discuss them in the context of MHD theory of magnetic pulsations, speculating on their generation mechanism.

Preface

The experimental work described in this thesis was carried out in the School of Chemistry and Physics, University of KwaZulu-Natal, Durban from March 2011 to July 2014, under the supervision of Dr J.A.E. Stephenson and Professor A.D.M. Walker.

These studies represent original work by the author and have not otherwise been submitted in any form for any degree or deploma to any tertiary institution. Where use has been made of the work of others it is duly acknowledged in the text.

DECLARATION 1 - PLAGIARISM

I, Zolile Mtumela, declare that

1. The research reported in this thesis, except where otherwise indicated, is my original research.

2. This thesis has not been submitted for any degree or examination at any other university.

3. This thesis does not contain other persons' data, pictures, graphs or other information, unless specifically acknowledged as being sourced from other persons.

4. This thesis does not contain other persons writing, unless specifically acknowledged as being sourced from other researchers. Where other written sources have been quoted, then:(a) Their words have been re-written but the general information attributed to them has been referenced (b) Where their exact words have been used, then their writing has been placed in italics and inside quotation marks, and referenced.

5. This thesis does not contain text, graphics or tables copied and pasted from the Internet, unless specifically acknowledged, and the source being detailed in the thesis and in the References sections.

Signed:.....

DECLARATION 2 - PUBLICATIONS

DETAILS OF CONTRIBUTION TO PUBLICATIONS that form part and/or include research presented in the thesis (include publications in preparation, submitted, in press and published and give details of the contributions of each author to the experiment work and writing of each publication)

Data collection and analysis was done by the student (Zolile Mtumela). Guidance, ideas and suggestions were formulated by Dr. J.A.E. Stephenson and Prof. A.D.M. Walker in preparation of the following publications.

Publication 1

- Z. Mtumela, J.A.E. Stephenson and A.D.M. Walker: An investigation of the nature of a Pc5 pulsation event using SuperDARN and magnetometer data. Accepted revised paper submitted to South African Journal of Science, 2014.

Publication 2

- Z. Mtumela, J.A.E. Stephenson and A.D.M. Walker: An investigation of the nature and generation mechanism of a Pc5 pulsation event using SuperDARN, magnetometer and satellite data. To be submitted to Annales Geophysicae.

Signed:.....

Acknowledgements

I would like to extend my thanks to the profound undermentioned persons, each of whom has made this research work possible.

Firstly, I would like to thank my supervisors Dr. J.A.E. Stephenson and Prof. A.D.M. Walker for their time, patience, ideas, guidance, suggestions, well-organised inspiring research environment with meetings and all the necessary insight throughout the work.

Special thanks to Dr. L. Magnus for introducing me to IDL and help me understand APF program. I would like to thank the IDL newsgroup, *comp.lang.idl-pvwave* particularly Dr. David Fanning for his assistance.

My sincere thanks to my family for giving me an opportunity to proceed with my studies and their unfailing support and to my friends and colleagues for their encouragement, motivation and assistance, particularly Mr. Makhamisa Senekane for his tireless assistance for lyx editor.

Many thanks to the space physics group (SANAE HF radar group) for their motivation, and fruitful time I have spent with them since 2008 and the UKZN for giving me an opportunity to study here.

My great thanks to South African National Space Agency (SANSA) for the financial support. I would like to thank the National Space Institute at the Technical of Denmark (DTU Space) for providing Greenland Magnetometer data, CARISMA and IMAGE Magnetometer Array teams for making data available on www.carisma.ca and http://space.fmi.fi/image, respectively.

I thank you!! (Ndiyabulela!!).

Contents

List of Figures

List of Tables

Chapter 1

Introduction

This chapter outlines the background of geomagnetic pulsation observations. The scientific motivation, goals of the thesis and an outline of the thesis follow.

1.1 Background outline

Ultra low frequency (ULF) hydromagnetic waves, often referred to as geomagnetic pulsations, have been observed for many years in magnetometer data and are endemic with the magnetosphere. The first observations of ultra low frequency fluctuations of magnetic field were made on the ground in 1861 by Stewart [59]. It was almost a century before their links to plasmas in near-earth space were established. Early studies of the magnetic pulsations measured by ground-based observers noted that waves could be grouped into classes that appeared to differ in fundamental ways. Some oscillations were continuous pulsations, quasi-sinusoidal in waveform, and each with a well-defined spectral peak were called Pc pulsations. Those with waveforms that were more irregular were called irregular pulsations (Pi). Dungey [17][18] was the first to propose that magnetohydrodynamic (MHD) waves in the outer atmosphere were the sources of the pulsating magnetic fields observed on the surface. The distinct periods of Pc pulsations suggested a resonant process. Dungey proposed that the pulsations were caused by waves standing along magnetic field lines and reflected at the ionosphere at the two ends. That idea was generally supported by the studies of both ground based and spacecraft data. Consequently, the classification of geomagnetic pulsations was accepted by the International Association for Geomagnetism and Aeromy (IAGA) in 1964 [29]. They were classified on the basis of their period as shown in Table 1.1. Since then it has become clear that, a subset, pulsations in the Pc5 band (1-5 mHz) are global scale magnetohydrodynamic (MHD) events in the magnetosphere.

	Label	Period range (s)	Frequency range (mHz)
Continuous pulsations	Pc1	0.2 - 5	200 - 5000
	Pc2	5 - 10	100 - 200
	Pc3	10 - 45	22 - 100
	Pc4	45 - 150	6.7 - 22
	Pc5	150 - 600	1.67 - 6.7
Irregular pulsations	Pi1	1 - 40	25 - 1000
	Pi2	40 - 150	6.7 -25

Table 1.1: IAGA magnetic pulsation frequency bands.

Since 1970s there has been a large contribution to the understanding of geomagnetic pulsations from VHF and HF radar experiments [66]. In a uniform cold magnetohydrodynamic medium (such as the magnetosphere), two characteristic oscillations can occur. Take z as the direction of the ambient magnetic field and x-z plane as containing the wave vector $\mathbf{k}$. The transverse Alfvén or slow wave is polarised with the magnetic field perturbation in the x-direction. Its dispersion relation is $\omega = \pm k_z V_A$ where $V_A^2 = \frac{B^2}{\mu_0 \rho}$. V_A is the Alfvén speed and ρ the mass density. Since the dispersion relation is independent of k_x, the direction of energy propagation is exactly along the magnetic field and a suitable Fourier synthesis of components with different values of k_x allows the wave to be confined to a single field line to a precision of the order of the gyroradius of the ions. The fast wave is polarized with magnetic perturbations in the y-z plane. Its dispersion relation is $\omega = \pm k V_A$ and is thus isotropic. It cannot be confined to a field line.

In a dipole field the two characteristic waves are coupled. If the azimuthal behaviour in the θ direction is given as $e^{im\theta}$, then the waves are decoupled in two extreme cases: $m = 0$ and $m \to \infty$. In the case $m = 0$, toroidal oscillations can occur which correspond to the shear Alfvén wave. Each magnetic shell defined by a particular L value, its equatorial radius, oscillates toroidally and independently with its own frequency, determined by the Alfvén velocity and field line length. The other mode is the poloidal mode, which is a breathing mode with magnetic field perturbations in the magnetic meridian. When m is small but finite, the two modes are coupled. In the case $m \to \infty$, the poloidal oscillations are decoupled and each field line oscillates at its own natural frequency determined by the Alfvén velocity and the field line length. This mode of oscillation is often called the guided poloidal mode because the disturbance is confined to the field line. The value of m, and phase velocity, can be determined for a resonance observed by a radar from the relationship between phase and longitude.

1.2 Scientific motivation

As discussed earlier, a subset of observed pulsations, those in the Pc5 band (1-5 mHz) are global scale magnetohydrodynamic (MHD) events in the magnetosphere. Numerous papers have reported the observation of Pc5 pulsations with the power at discrete and stable

frequencies; the most commonly occurring being 1.3 mHz, 1.9 mHz, 2.6 mHz and 3.3-3.4 mHz [51][48][22][57][67][42]. The quantization of the resonance frequencies is predicted by the cavity mode theory which was first developed by Kivelson and Southwood [32] and later modified into waveguide theory [51][70] to account for the azimuthal propagation of the compressional mode. However, Ziesolleck [71] showed that the waveguide/cavity mode frequencies do not necessarily represent a unique set of frequencies. In order to understand the stability and reproducibility of these frequencies, many authors have focused on investigating possible excitation mechanisms [32][52][19][57][64].

A field line resonance (FLR) is essentially a standing shear Alfvén wave on a magnetic field line between the two points on a conducting ionosphere [16]. They can arise from an external influence in the solar wind such as Kelvin-Helmholtz instability, or abrupt change in solar wind dynamic pressure, coherent waves in the solar wind, which in turn that can excite field lines inside the magnetosphere into compressional oscillation [62]. The field lines on the L-shell with the same characteristic frequency will resonate and large oscillations will be set up over a narrow range of latitudes. The theory of Southwood [53] and Chen & Hasegawa [11] predicted that an enhancement in amplitude at the resonance L-shell is accompanied by a phase change of approximately 180 degree. This behaviour is the result of the fact that L-shells nearer the earth have higher frequencies than the driver and lead it in phase and those that are near the magnetopause have lower frequencies than driver and lag it in phase. Walker et al. [66] provided compelling evidence in favour of this theory, where they used STARE radar data to plot amplitude and phase of an electric field. FLRs generated by all these mechanisms tend to have small azimuthal wave numbers m. The generation mechanism remains in debate. All the mechanisms mentioned above and more including some in the magnetotail [20], have been shown to be present.

Another type of pulsation in the Pc5 band can be generated by drift-bounce resonance with energetic ring current particles. These are often compressional in the nature and tend to have large values of m. The drift-bounce resonance occurs when a particle drifts in one bounce period by an integral number of azimuthal wavelengths Doppler shifted by the azimuthal phase velocity of the wave. The high energy particles which constitute the bulk of ring current may be responsible for exciting compressional Pc5 through drift bounce resonance [54][12]. The resonant particle has a drift path which oscillates between L shells at the same characteristic frequency as oscillations in perpendicular, parallel and total kinetic energy.

The drift-bounce resonant interaction of energetic ring current particle with Alfvén waves have been proposed as possible excitation mechanisms [55].

1.3 Goals of this thesis

The main goal of this work is to employ an Automated Pulsation Finder program to identify suitable Pc5 pulsation events that occur simultaneously in multiple radars of the

SuperDARN network and to use these for the determination of the physical characteristics of the Pc5 pulsation. In this work three SuperDARN HF radars (Goose Bay, Saskatoon and Pykkvibaer) together with ground-based magnetometers are used to study Pc5 pulsation events. SuperDARN is an international project of which the South African radar at Sanae, Antarctica is a part. Our emphasis in this thesis is the determination of the physical characteristics of the Pc5 pulsation, using HF radar and magnetometer ground-based instruments. These two instrument types have a synergy. One has a high temporal resolution (magnetometer) and the other has good spatial resolution (HF radar). Furthermore, ionospheric conditions not conducive to observing pulsations in radar data, are favourable for observations in magnetometer data, and vice vesa. The pulsation finder highlights a significant pulsation in one HF radar. We then proceeded to search for a similar resonance in other radars and magnetometers at similar magnetic latitudes. A complex demodulation technique was applied to determine the amplitude and phase relationship between field components observed by the radar and magnetometer chains. Further, by determining their qualitative polarization characteristics and investigation amplitude and phase information, other characteristics like wave number and phase velocity were determined.

Pc5 pulsations are global magnetohydrodynamic events and, as such, HF radars are superior observers of them due to their extensive fields of view. However, very few pulsation events whereby multiple radars and coordinated magnetometers simultaneously observing a pulsation over extensive fraction of global longitude have been presented and analysed in the literature. The work presented in this thesis provides three such events. In order to illustrate such events unique maps of the observations by radars and magnetometers (for example Figure 7.5) have been generated.

1.4 Outline of this thesis

The background of the geomagnetic pulsations is provided in Chapter 1 along with the important concepts of this study such as field line resonances and several key concepts such as Kelvin-Helmholtz instabilities, cavity/wave mode.

Chapter 2 is one of the key chapters that provide more understanding on the derivation of MHD equations using basic ideas of electromagnetic theory, Newtonian mechanics and thermodynamics. MHD approximation is used to derive set of equations which govern the dynamics of fluids. Equations of motion are developed for each fluid species under the action of electrodynamic forces arising from the motions of all the species and include mechanical forces arising from the pressure gradients.

The study of propagation in a uniform medium is seldom applicable to real problems, except in a qualitative way. Spatial gradients in unbounded plasma introduce some complexities. Gradients of pressure and magnetic field perpendicular to the field lines and the associated field line curvature mean that the characteristic waves in a uniform plasma are

not propagated independently, which is one of the natural complexities. In Chapter 3, we derive sets of equations that can be used in a variety of circumstances. We use the box model where the magnetic field lines are straightened and bounded by conducting planes to study wave propagation in the magnetosphere. To study waves in such a system, it is necessary to linearize the MHD equations including the products of zero-order gradients with first order wave perturbations. Sets of first order differential equations have been derived for box model. Second order differential equations have been found together with approximate forms appropriate for near singularities.

Chapter 4 is one of the most important chapters in this study. It provides more details on the key concepts such as field line resonances, cavity mode, latitude profiles of amplitude and associated phase and how the ULF wave interacts with the ionosphere.

Chapter 5 provides an understanding of SuperDARN radars that produce line-of-sight Doppler velocities, field of view plots and range time summary plots. Chapter 6 provides an explanation of ground-based magnetometer data that measure the Earth's magnetic field that are used in this study.

The core of this study lies in the chapters 7, 8 and 9, where the observations are presented with details of how the observations were obtained and analysed. The observations are evaluated there and presented in a graphical form and discussed in the context of MHD theory of magnetic pulsations. These chapters include reasoning behind the interpretation of the observations and their significance.

Chapter 10 presents the conclusion regarding this work. Some possible future work is suggested.

Chapter 2

MHD wave equations

2.1 Introduction

The MHD equations are derived using the basic ideas of electromagnetic theory, Newton's mechanics and thermodynamics. The Maxwell's equations for the electric and magnetic fields have two independent solutions. In addition, a sound wave in a gas like the atmosphere is produced by a change in pressure at the source of the wave, the pressure perturbation travel through the atmosphere. In a magnetized plasma the two electromagnetic waves are coupled to the sound wave by the "frozen in" magnetic field, and there are three solutions to the basic equations. The low frequency approximation to the basic equations is called magnetohydrodynamics (MHD). The wave solutions to these equations are called MHD waves. Through some assumptions of the system and simplifications, it can be demonstrated that the differential equations that result are of the same form as the differential equation for a travelling wave.

The wave equations were derived using Walker's text [65]. We present the significant steps for the understanding of the wave equations. For a more thorough discussion of the derivation the reader is referred to the text.

2.2 Basic Equations

The MHD waves are found as solutions to express conservation laws and Maxwell's equations.

The continuity equation

$$\frac{\partial \rho}{\partial t} + \nabla . \rho \mathbf{v} = 0. \tag{2.1}$$

The momentun equation

$$\rho\frac{d\mathbf{v}}{dt} = \mathbf{J} \times B - \nabla p. \tag{2.2}$$

Adiabatic law

$$\frac{dp}{d\rho} = \frac{\gamma p}{\rho}. \tag{2.3}$$

Solenoidal condition

$$\nabla.\mathbf{B} = 0 \tag{2.4}$$

Ohm's law

$$\mathbf{E} \times \mathbf{v} \times B = 0. \tag{2.5}$$

Maxwell's equations

$$\nabla \times \mathbf{E} = -\frac{\partial \mathbf{B}}{\partial t} \tag{2.6}$$

$$\nabla \times \mathbf{B} = \mu_0 \mathbf{J}. \tag{2.7}$$

The Maxwell's equations, continuity and momentum equations, the adiabatic law and Ohm's law complete a set of four vector and two scalar equations.

2.3 Reduced set of MHD Equations

It is convenient to eliminate some of the variables from the set of equations to get a reduced MHD equations as follow.

Equation (2.7) was used to eliminate **J** from the momentum equation (2.2).

$$\rho\frac{d\mathbf{v}}{dt} = -\nabla\left\{p + \frac{B^2}{2\mu_0}\right\} + \frac{\mathbf{B}}{\mu_0}.\nabla\mathbf{B}. \tag{2.8}$$

This shows that the forces acting on a plasma will derive from pressure gradients, thermal and magnetic pressure, gradients in the magnetic field and motion through magnetic field.

The continuity equation may be rewritten in the form:

$$\frac{d\rho}{dt} = -\rho\nabla.\mathbf{v}. \tag{2.9}$$

The adiabatic law may be combined to give:

$$\frac{dp}{dt} = -\gamma p \nabla . \mathbf{v}. \tag{2.10}$$

The electric field may be eliminated from (2.6) by using Ohms law (2.5):

$$\frac{d\mathbf{B}}{dt} = \mathbf{B}.\nabla\mathbf{v} - \mathbf{B}\nabla.\mathbf{v}. \tag{2.11}$$

2.4 Derivation of the wave equations

For simplicity, the wave perturbations studied here are assumed to be small amplitude perturbations. If the perturbations of the medium are small, we can linearise the reduced MHD equations by neglecting second order terms in the perturbations. The magnetic field, mass density and pressure will change and the background velocity of the plasma will be zero, so that

$\mathbf{B} \to \mathbf{B} + \mathbf{b}$

$\rho \to \rho_0 + \rho$

$p \to P + p$

$v \to v$

where $\mathbf{B}$, ρ_0 and P are unperturbed variables describing the equilibrium state and $\mathbf{b}$, ρ, p and v are small perturbations of these quantities.

The linearised first order MHD equations are given as

$$\rho_0 \frac{\partial \mathbf{v}}{\partial t} = -\nabla \left\{ p + \frac{\mathbf{B}.\mathbf{b}}{\mu_0} \right\} + \frac{\mathbf{B}}{\mu_0}.\nabla\mathbf{b} \tag{2.12}$$

$$\frac{\partial p}{\partial t} = -\gamma p \nabla . \mathbf{v} \tag{2.13}$$

$$\frac{\partial \mathbf{b}}{\partial t} = -\mathbf{B}\nabla.\mathbf{v} + \mathbf{B}.\nabla\mathbf{v}. \tag{2.14}$$

If (2.12) is differentiated with time and (2.13) and (2.14) used to eliminate p and $\mathbf{B}$, we get

$$\rho_0 \frac{\partial^2 \mathbf{v}}{\partial t^2} = \nabla \left\{ \left(\gamma p + \frac{B^2}{\mu_0} \right) \nabla . \mathbf{v} \right\} - \nabla \left\{ \frac{\mathbf{B}}{\mu_0} . (\mathbf{B}.\nabla)\, \mathbf{v} \right\} - \frac{1}{\mu_0} (\mathbf{B}.\nabla) \left\{ \mathbf{B}\nabla.\mathbf{v} - (\mathbf{B}.\nabla)\, \mathbf{v} \right\}. \tag{2.15}$$

If we assume that the zero-order quantities do not vary in space then

$$\frac{\partial^2 \mathbf{v}}{\partial t^2} = \left(V_A^2 - V_S^2\right) \nabla \left(\nabla . \mathbf{v}\right) - \nabla \left(\mathbf{V}_A . \nabla\right) \left(\mathbf{V}_A . \mathbf{v}\right) - \mathbf{V}_A \left(\mathbf{V}_A . \nabla\right) \left(\nabla . \mathbf{v}\right) + \left(\mathbf{V}_A . \nabla\right) \left(\mathbf{V}_A . \nabla\right) \mathbf{v} \tag{2.16}$$

where

$$\mathbf{V}_A = \frac{\mathbf{B}}{\sqrt{\mu_0 \rho_0}}; V_S = \sqrt{\frac{\gamma p}{\rho_0}} \tag{2.17}$$

The above equation (2.16) is the wave equation governing small amplitude velocity perturbations in a uniform magnetised plasma. The quantity $\mathbf{V}_A$ is called the Alfvén velocity and V_S will be recognised as speed of sound.

We assume that a harmonic wave solution can be made up of a sum of sine and cosine waves of various amplitudes. We define the wave number as $\mathbf{k}$ having the direction of the wave normal and a magnitude equal to the wavenumber $2\pi/\lambda$. A complex plane harmonic wave behaviour is given by

$$A \exp\left\{i \left(\mathbf{k}.\mathbf{r} - \omega t\right)\right\} \tag{2.18}$$

The operators ∇ and $\frac{\partial}{\partial t}$ can be replaced by $i\mathbf{k}$ and $-i\omega$ respectively so that (2.16) becomes

$$\left\{\omega^2 - \left(\mathbf{k}.\mathbf{V}_A\right)^2\right\} \mathbf{v} - \mathbf{k} \left(V_A^2 + V_S^2\right) \mathbf{k}.\mathbf{v} + \left(\mathbf{k}.\mathbf{V}_A\right) \left\{\mathbf{k} \left(\mathbf{V}_A.\mathbf{v}\right) + \mathbf{V}_A \left(\mathbf{k}.\mathbf{v}\right)\right\} = 0. \tag{2.19}$$

In magnetic field aligned coordinates, in which the ambient magnetic field is in the z-direction and wavevector $\mathbf{k}$ is in the xz-plane, this equation can be written in component form using as

$$\begin{pmatrix} \omega^2 - k_z^2 V_A^2 - k_x^2 \left(V_A^2 + V_S^2\right) & 0 & -k_x k_z V_S^2 \\ 0 & \omega^2 - k_z^2 V_A^2 & 0 \\ -k_x k_z V_S^2 & 0 & \omega^2 - k_z^2 V_S^2 \end{pmatrix} \begin{pmatrix} v_x \\ v_y \\ v_z \end{pmatrix} = 0. \tag{2.20}$$

If this expression is transformed to wave aligned coordinates, we get

$$\begin{pmatrix} \omega^2 - k^2 V_A^2 cos^2\theta & k^2 V_A^2 cos^2\theta \\ -k^2 V_A^2 sin^2\theta & \omega^2 - k^2 \left(V_A^2 cos^2\theta + V_S^2\right) \end{pmatrix} \begin{pmatrix} v_T \\ v_L \end{pmatrix} = 0 \tag{2.21}$$

$$\left(\omega^2 - k^2 cos^2\theta\right) v_y = 0. \tag{2.22}$$

These equations have a non-trivial solution if the determinant of the coefficient matrix is zero, giving the dispersion relations.

Wave type	$\theta = 0°$	$\theta = 90°$
Shear Alfven	$v_p = V_A$	0
Magnetosonic	$v_p = V_A$or V_S	0 or $v_p = \sqrt{V_A + V_S}$

Table 2.1: Limiting cases for shear Alfven and magnetosonic phase velocity

$$\omega^2 - k^2 V_A^2 cos^2\theta = 0 \tag{2.23}$$

$$\omega^4 - k^2 \left\{V_A^2 + V_S^2\right\} \omega^2 + k^4 V_A^2 V_S^2 cos^2\theta = 0. \tag{2.24}$$

If the above two equations are divided by k^2 and k^4 respectively, we get

$$v_p^2 = V_A^2 cos^2\theta \tag{2.25}$$

$$v_p^2 = \frac{1}{2}\left\{\left(V_A^2 + V_s^2\right) \pm \sqrt{\left(V_A^2 + V_S^2\right)^2 - 4V_A^2 V_S^2 cos^2\theta}\right\}. \tag{2.26}$$

which are the equations governing the phase velocity of the various waves.

There are three types of waves permitted by this set of dispersion relations. They are transverse or shear Alfvén and magnetosonic waves. The magnetosonic waves are divided into two waves, namely, fast and slow magnetospheric waves respectively, which are coming from the positve and negative solutions of the quadratic equation.

Table (2.1) shows the limiting cases where the waves is either travelling parallel to the magnetic field ($\theta = 0°$) or travelling perdendicular ($\theta = 90°$ to the field.

2.5 Summary

For simplicity, we have assumed that the perturbations carried by the waves are small amplitude. Magnetohydrodynamic and small amplitude wave approximations were made for the equation describing a uniform magnetised plasma. The differential equation in the velocity perturbation parameter v in both space and time is given. This differential equation is the same form as that for a travelling wave, indicating that the perturbation will propagate through the medium as a plasma wave. There are characteristic waves possible in the medium, namely Alfvén wave, fast and slow magnetosonic waves. The Alfvén wave is a wave in which the perturbation is an oscillation perpendicular to the plane containing the wave normal and unperturbed magnetic field. The fast and slow magnetosonic waves are compressional waves with perturbations in the plane containing the wave normal and the unperturbed magnetic field. The fast wave is approximately isotropic. This Chapter gave a basic qualitative view of the types of MHD waves that are observed.

Chapter 3

MHD waves in the magnetosphere

3.1 Introduction

In the previous chapter we have been mainly concerned with the behaviour of MHD waves in a homogeneous plasma. In this chapter we abandon the assumption of bounded medium and consider a model of an unbounded MHD medium and compare of how this differs from homogenous medium discussed earlier. The perturbations that propagate through the magnetosphere, encounter two regions of interest, the turning and the resonance points.

3.2 The magnetosphere

A planet's magnetosphere is defined as the region of space around which the planet's magnetic field dominates over interplanetary effects. The layer that separates the interplanetary medium from the magnetosphere is called the magnetosheath. These regions are graphically shown for Earth in Figure 3.1. The magnetosheath is the region of interaction between the solar wind and the Earth's magnetic field. It exhibits high particle energy flux, where the direction and magnitude of the magnetic field vary, which is caused by the solar wind dynamic pressure. The magnetosheath is an ideal region for studying the effects of inhomogeneity which has a crucial effect on the generation and propagation of the ultra low frequency (ULF) waves.

A field line is termed closed if it forms a closed loop inside the magnetosphere. In order to model the behaviour of the magnetosphere many authors including Southwood [53], have made use of the box model. The sketch of a cross section of the magnetosphere on the flank, at dawn or dusk is shown on the left in Figure 3.2. The region of closed field lines in the magnetosphere is represented by the unshaded region. The magnetosphere is bounded by magnetosheath plasma along CDE, which represents the magnetospause, by polar cap plasma along the BC and EF, and by the ionosphere along FGAB. The points A and G coincide at the equator where at its apex, a dipole field line is tangential to the surface

of the Earth. The magnetopause boundary is characterized by discontinuities in density, pressure, magnetic field and velocity. At the polar cap boundaries discontinuities are less pronounced, the characteristics of the plasma change but do not affect the MHD properties strongly. There are changes in the electric field associated with plasma convection processes.

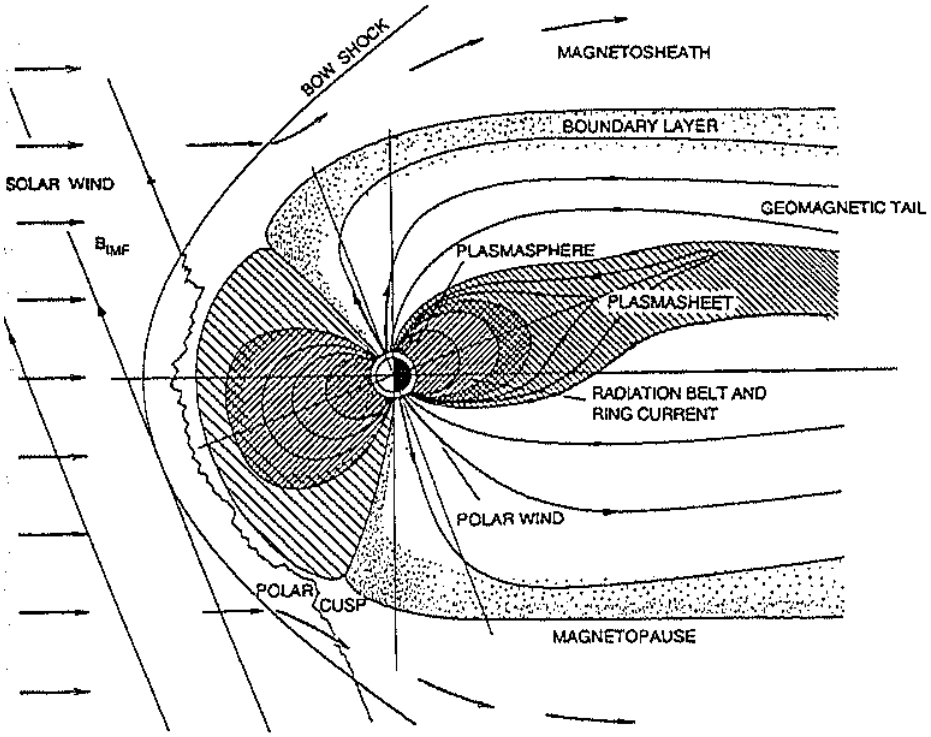

Figure 3.1: Schematic illustration of the magnetosphere showing various regions source from the internet [4].

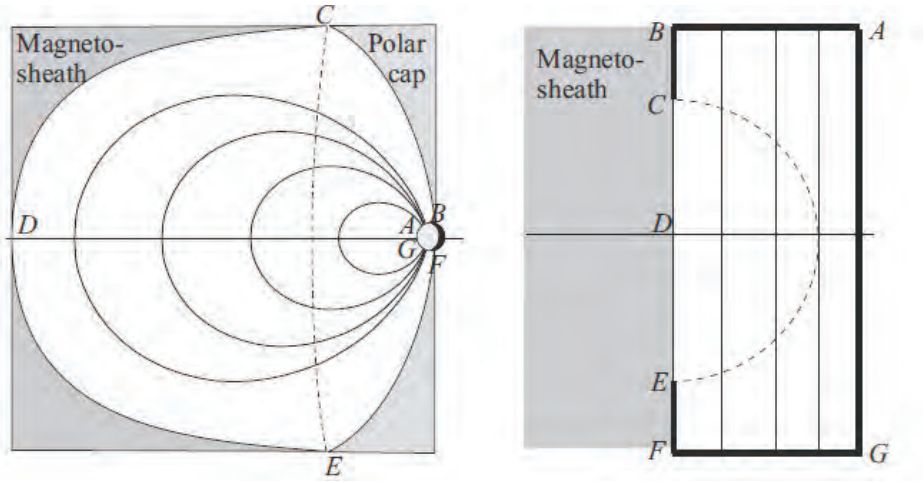

Figure 3.2: Modelling the magnetosphere illustration from Walker [65].

3.3 The MHD equations for the magnetosphere

The magnetosphere described above is not homogenous, but it allows variations in the x-direction. In the box model of the magnetosphere, the x -axis is along the Sun-Earth line (positive earthward), the z -axis is along the magnetic field lines and y -axis represents the east-west component. The density ρ_0, pressure P, and the magnitude and direction of $\mathbf{B}$ are assumed to be dependent on x. The pressure balance condition depends only on the magnitude of $\mathbf{B}$, not on its direction. The wave fields vary with y, z, and t as

$$\exp\left\{-i\omega + ik_y y + ik_z z\right\} \tag{3.1}$$

so that in the differential equation we can substitute $\frac{\partial}{\partial t}$ with $-i\omega$, $\frac{\partial}{\partial y}$ with ik_y and $\frac{\partial}{\partial z}$ with ik_z

The equations to be introduced describe the waves in an infinite medium with such a gradient. Boundaries perpendicular to the field lines, such as the ionosphere, are represented by conducting planes. There may also be boundaries taking the form of tangential discountinuities perpendicular to the directiond of the gradients.

The wave variables at these boundaries are the normal components of displacement ξ and the generalized pressure $\psi = p + \frac{\mathbf{B}.\mathbf{b}}{\mu_0}$ are continuous across the boundary. When the fields are varying with x, then the independent variables in the equation are continuous even at the discontinuity. The derivation equations are using the pressure ψ, normal displacement ξ and η, the component of the plasma displacement in the direction perpendicular to $\hat{x}$ and $\mathbf{B}$.

The displacements are related to the perturbation velocity components by

$$v_x = -i\omega\xi \tag{3.2}$$

$$v_\perp = -i\omega\eta \tag{3.3}$$

The direction of $\mathbf{B}$ rotates in the yz -plane as x advances. After linearising the MHD waves equations (2.8), (2.10) and (2.11) in considering the spatial variation in x, and after some algebra this gives

$$\frac{d\psi}{dx} = F(x)\,\xi \tag{3.4}$$

$$\frac{d\xi}{dx} = \frac{G(x)}{F(x)}\psi \tag{3.5}$$

where

$$F(x) = \rho_0 \left[\omega^2 - (\mathbf{k}.\mathbf{V}_A)^2\right] \tag{3.6}$$

$$G(x) = \frac{\omega^4}{\omega^2\left(V_A^2 + V_S^2\right) - (\mathbf{k}.\mathbf{V}_A)^2 V_S^2} - k_y^2 - k_z^2 \tag{3.7}$$

These two equations describe the behaviour of the magnetosonic waves in the varying medium. The equation governing the perturbation displacement η is given by

$$\eta = i\frac{k_\perp \psi}{\rho_0\left(\omega^2 - (\mathbf{k}.\mathbf{V}_A)^2\right)} \tag{3.8}$$

where $k_\perp$ is the component of $\mathbf{k}$ in the direction of η, which is the transverse Alfvén wave. It is driven by the magnetosonic waves but does not influence the solution of the other two above equations. It is convenient to take the direction of the magnetic field to be in the z -direction, $k_\perp = k_y$ and $(\mathbf{k}.\mathbf{V}_A)^2 = k_z^2 V_A^2$.

Either ξ or ψ may be eliminated from (3.4) and (3.5), giving rise to second order differential equations

$$\frac{d^2\xi}{dx^2} + \frac{(F/G)'}{F/G}\frac{d\xi}{dx} + G\xi = 0 \tag{3.9}$$

$$\frac{d^2\psi}{dx^2} - \frac{F'}{F}\frac{d\psi}{dx} + G\psi = 0 \tag{3.10}$$

These differential equations are typical in wave equation problem. If the medium is homogeneous, then the coefficient of $\frac{d\xi}{dx}$ is zero and resulting equation will be the spatial part of the standard wave equation.

$$F(x) = \rho_0\left(\omega^2 - k_z^2 V_A^2\right) \tag{3.11}$$

$$G(x) = \frac{\omega^2}{V_A^2} - k_y^2 - k_z^2 \tag{3.12}$$

It is always possible to solve these equation numerically, and the physical insight is best obtained by considering analytic solutions of various approximation forms.

3.4 Singular points in the magnetosphere

The poles and zeros of (3.9) are controlled by the zeros of (3.11) and (3.12) i.e. when

$$\omega^2 = k_z^2 V_A^2 \text{and} \frac{\omega^2}{V_A^2} = k_y^2 + k_z^2. \tag{3.13}$$

The first equation in (3.13) gives the values in F and the second gives the values of ω for a zero G.

Approximations are developed that apply over the range of the turning and resonance points in the magnetosphere. The differential equation (3.10) has a turning point where $G = 0$ and singularities where $F = 0$.

At the turning point we get

$$k_x^2(x) = \frac{w^2}{V_A^2(x)} - k_y^2 - k_z^2, \tag{3.14}$$

where V_A is monotonically increasing with x. The phase intergral solution of a perturbation propagating from 0 to x is represented by

$$\exp\{\pm i \int_0^x k_x(x)dx\}. \tag{3.15}$$

The lower and upper signs correspond to waves propagated in both positive and negative x-directions. At the point where $G = 0$ the second equation in (3.13) determines that $k_x = 0$. When x is smaller than this point, k_x is real and the wave propagates, however, when x is larger than this point, k_x becomes imaginary and so the wave cannot propagate.

At the resonance point, a zero of F occurs at point $x = x_R$, where $\omega^2 = k_z^2 V_A^2(x_R)$. If V_A is assumed to be an analytic function of x which is real on the x-axis, then it can hold for a complex value of x .

3.5 Away from singular points

Consider the second order wave equation (3.10), we write it in the form

$$\psi'' - \frac{F'}{F}\psi' + k^2 q^2(x)\psi = 0, \tag{3.16}$$

where $k^2q^2(x) = G(x)$ with k a constant and q a dimensionless function that depends of x. The WKBJ method was applied which gives

$$\psi(x) = (\frac{F(x)}{q(x)})^{\frac{1}{2}} \exp\{ik \int^x q(x)dx\}. \tag{3.17}$$

This approximate solution breaks down when $G \to 0$ and $F \to 0$, and at such level reflection takes place.

3.6 Approximate form near $G = 0$

The zero of G is a turning point occuring at $x = x_T$, then by expanding F and G to first order in $|x - x_T|$ we get

$$G = G_0' (x - x_T) + O\left[(x - x_T)^2\right] \tag{3.18}$$

$$F = F_0' + O(x - x_T) \tag{3.19}$$

If we ignore higher derivatives of G and F , then equations (3.9) and (3.10) are approximately.

$$\frac{d^2\psi}{dx^2} + G_0' (x - x_T)\psi = 0 \tag{3.20}$$

$$\frac{d^2\xi}{dx^2} = \frac{1}{x - x_T}\frac{d\xi}{dx} + G_0' (x - x_T)\xi = 0. \tag{3.21}$$

if we let $\varsigma = -\left(|G'(x_T)|\right)^{1/3}(x - x_T)$ then

$$\frac{d^2\psi}{d\zeta^2} = \zeta\psi \tag{3.22}$$

$$\frac{d^2\xi}{d\zeta^2} - \frac{1}{\zeta}\frac{d\xi}{d\zeta} - \zeta\xi = 0. \tag{3.23}$$

Equation (3.22) is known as Stokes's equation. It has a general solution

$$\psi = AAi(\zeta) + BBi(\zeta). \tag{3.24}$$

The special functions Ai and Bi are the Airy functions. The Stokes equation has no singularities for finite ζ, it has solutions that are finite and single valued for finite ζ. These solutions are real for all the real ζ.

3.7 Approximate form near $F = 0$

The zero of F is a resonant point occuring at $x = x_R$. If we make the substitution $\zeta = k_y (x - x_R)$ then

$$\frac{d^2\xi}{d\zeta^2} + \frac{1}{\zeta}\frac{d\xi}{d\zeta} - \xi = 0 \tag{3.25}$$

$$\frac{d^2\psi}{d\zeta^2} - \frac{1}{\zeta}\frac{d\psi}{d\zeta} - \psi = 0 \tag{3.26}$$

The first of these equation is the modified Bessel equation of order zero with solution I_0 and K_0. Its solutions are the modified Bessel function $I_0(\zeta)$ and $K_0(\zeta)$. The first few terms of the series solutions of I_0 and K_0 are

$$I_0(\zeta) = 1 + \frac{1}{4}\zeta^2 + \frac{\left(\frac{1}{4}\zeta^2\right)^2}{(2!)^2} + \frac{\left(\frac{1}{4}\zeta^2\right)^2}{(3!)^2} + \cdots \tag{3.27}$$

$$K_0(\zeta) = -\left[ln\frac{1}{2}\zeta + \gamma\right] I_0(\zeta) + \frac{1}{4}\zeta^2 + \left(1 + \frac{1}{2}\right)\frac{\left(\frac{1}{4}\zeta^2\right)^2}{(2!)^2} + \cdots \tag{3.28}$$

where γ is Euler's constant.

3.8 Summary

The magnetosphere has a magnetic field which is approximately dipolar. The magnetic field and density are functions of position, therefore their gradients cannot be ignored. The wave equations do not separate into equations describing modes that can be identified with the transverse Alfvén and isotropic Alfvén waves. The magnetosphere perturbation is either magnetized or plasma parameters near the magnetosheath which give rise to a fast magnetosonic wave that will propagate at the Alfvén velocity equally in all directions. The nature of the WKBJ solutions is that they separate waves propagating in opposite direction. The behaviour of the perturbation is approximated by the Airy function Ai. In this chapter we considered various approximations of the wave equations (3.9) and (3.10) where the turning and resonance points are well separated. In these circumstances, near the turning point the equations were reduced to Stokes equation with the solution being the Airy function. Near the resonance point, the equations reduced to the modified Bessel equation. The wave beyond the turning point will be evanescent if the resonance is sufficiently removed from the turning point. Otherwise, an inhomogeneous wave will transfer the energy to the resonance.

Chapter 4

ULF resonance

4.1 Introduction

ULF waves are prevalent in the magnetosphere and are a useful tool in space weather studies. Waves created outside the magnetosphere must pass through the magnetopause to be seen at the ground. The ULF waves seen on the ground are not usually the same waves that enter the magnetosphere from the solar wind because the wave energy is transformed and amplified by processes inside the magnetosphere such as field line resonance and other cavity resonances. The cavities between various boundaries act like resonant cavities or waveguide [31]. Many of the pulsations seen at the ground are radiated from the ends of field lines set into motion by a complex process such as the coupling of the waves to resonant cavities and they have both internal and external sources.

4.2 Field line resonance

Closed field lines of the Earth's magnetic field dipole behave like vibrating strings as shown in Figure 4.1. Each end of the field lines is fixed to the conducting ionosphere, although they can bend. In the absence of the force the field lines attain equilibrium. However, if some processes that may develop in the magnetosphere happen to displace them, a tension force would develop and try to restore them back to their equilibrium position. Because the field line is loaded with gyrating particles, it picks up momentum that causes it to overshoot the equilibrium and thus oscillate until other processes damp them.

There are two primary modes of oscillation of a dipole field line that can exist [56]. The toroidal mode is a displacement in the azimuthal direction creating an azimuthal magnetic perturbation as shown in the right panels of Figure 4.1. On the other hand, the poloidal mode is a radial displacement with radial magnetic perturbations as shown in the middle panels of the same Figure. The field lines of a dipole (middle panels) may be approximated as stretched strings (left panels). The dipole may be displaced and oscillate in two

orthogonal directions in the radial (center panels) and azimuthal (right panels). The oscillation may consist of odd (top row) or even (bottom row) harmonics. The field lines are anchored at the ends (ionosphere) and are nodes of a field line displacement, but antinodes of the magnetic perturbation. In the diagram ξ represents the field line displacement and b_x and b_y are components of the magnetic perturbation. Field line resonance is associated with toroidal oscillation mode. At the high geomagnetic latitudes the field line resonant frequency can be in the Pc5 pulsation band [69].

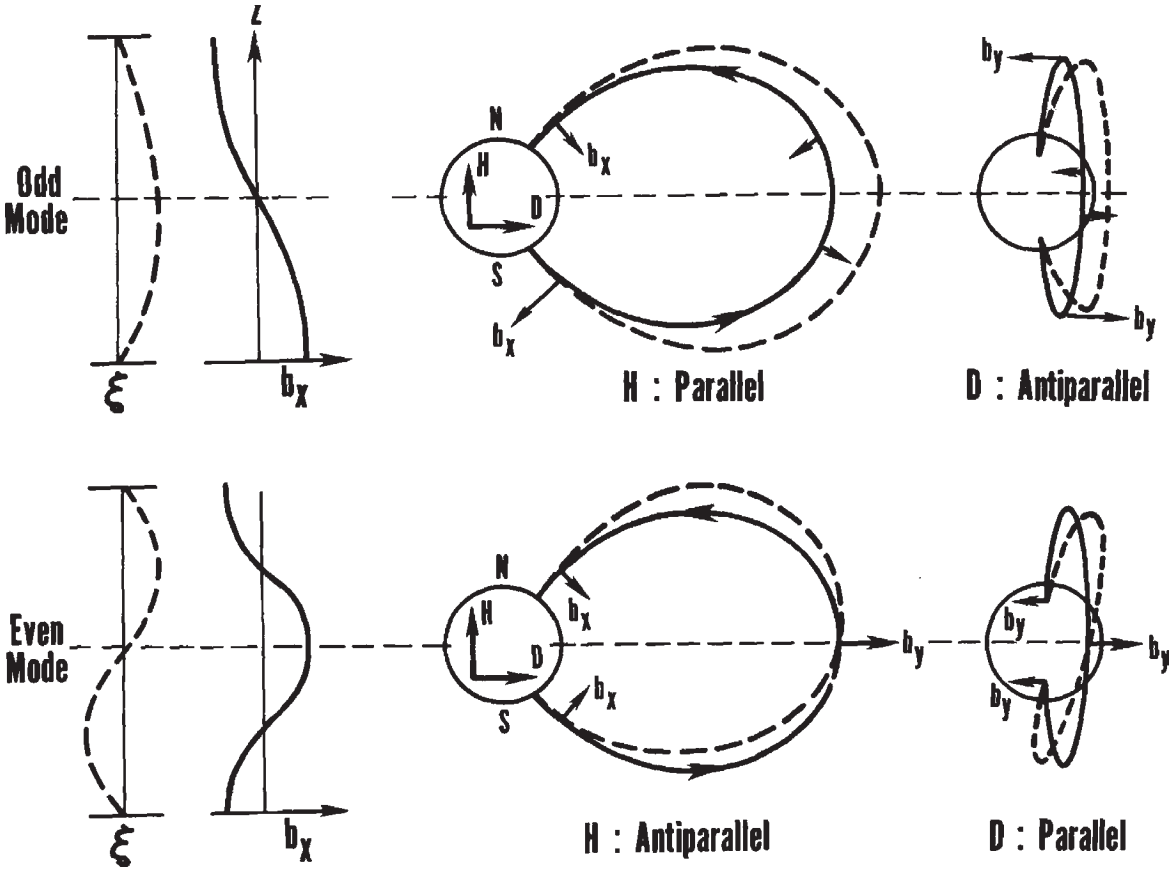

Figure 4.1: The field line of a dipole (middle panels) may be approximated as stretched strings (left panels). The dipole lines displaced and oscillate in two directions, radial (center panels) and azimuthal (right panels) illustration from McPherron [41].

The toroidal mode of field line resonance is most commonly observed in space. The reason is that azimuthal perturbations do not change the field magnitude or cause plasma density changes. The field line azimuthal adjacent to the vibrating line has nearly the same resonant frequency and can vibrate in phase with the initial disturbed line. This mode of field line corresponds to the Alfvén mode. The poloidal mode is harder to excite because field lines are oscillating in the radial direction and radially adjacent field lines have different frequencies, which leads them to oscillate out of phase and there will be compression. These properties identify this mode as fast mode. The frequency and the

Alfvén velocity of the field lines are dependent on the length of the field lines and strength of the magnetic field and plasma density such that longer field lines as well as with more, or heavier particles will resonate with low frequencies. This behavior of the Alfvén velocity and resonant periods is shown in Figure 4.2.

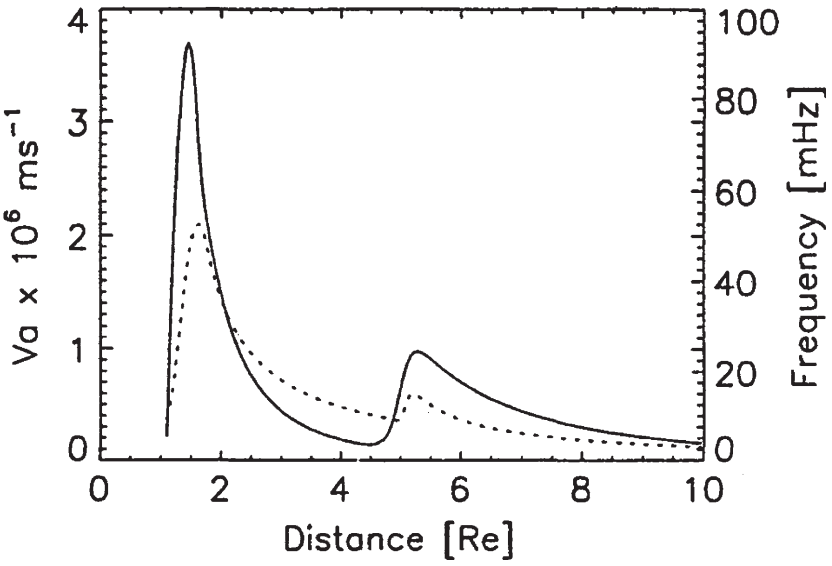

Figure 4.2: The radial profile of Alfvén velocity (solid line) and field line resonance frequency (dotted line) in magnetosphere illustration from Waters [68].

In this model the magnetopause is located at 10 Re, plasmapause at 5 Re, and the ionosphere at 1.1 Re. The frequency and Alfvén velocity are expected to increase smoothly from the magnetopause to ionosphere but there are some deviations in the plasmasphere region as well as in the ionosphere. The sudden decrease in velocity and frequency at about 5 Re is due to the increase in plasma density going inward across the plasmapause. Another decrease in the ionosphere is caused by the presence of heavy particles such as oxygen ions in the upper ionosphere.

The field line resonance can be excited by any process that displaces the field lines. The most common source is ULF waves propagating through the magnetosphere after transmitted through the magnetopause.

4.3 Latitude profiles of the amplitude and phase resonant pulsations

External influences such as Kelvin-Helmholtz instability or abrupt changes in solar wind dynamic pressure can excite field lines inside the magnetosphere in oscillation [62]. Field lines at a L-shell (e.g. L-shell D in Figure 4.3) with the same frequency will resonate and large oscillations will be set up over a narrow range of latitudes. The schematic representation of this mechanism is shown in Figure 4.3 , where Kelvin-Hemholtz instabibility is

responsible for the excitation of the field lines into resonance.

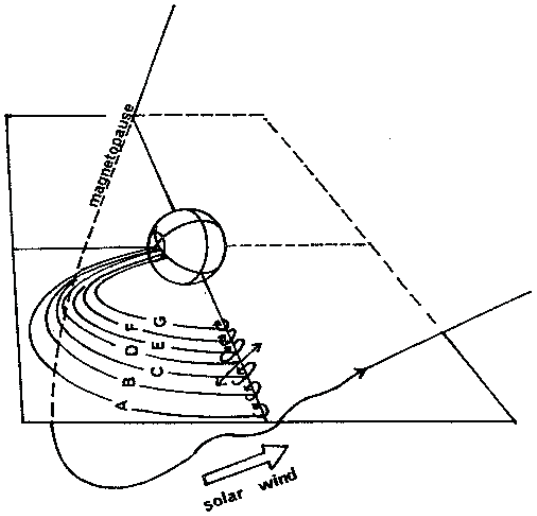

Figure 4.3: Schematic representation of a Pc5 resonance showing how a Kelvin-Helmholtz wave on the magnetospause excites a particular L-shell into resonance illustration from Walker [62].

This Figure illustrates, the theory of Chen and Hasegawa [11] and Southwood [53] which predicted that an enhancement in amplitude at the resonance L-shell is accompanied by a phase change approximately 180 degrees. This behaviour is the result of the fact that L-shells nearer the earth have higher frequencies than the driver and lead it in phase and those that are near the magnetopause have lower frequencies than the driver and lag it in phase. Walker *et al* [66] provided the compelling evidence in favour of this theory, where they used STARE radar data to plot amplitude and phase of an electric field of a FLR as shown in Figure 4.4.

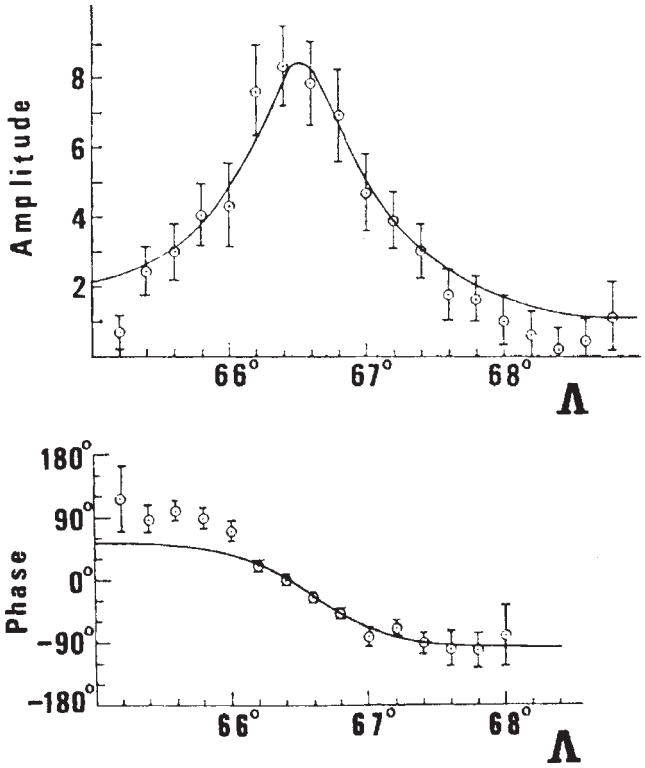

Figure 4.4: The theoretical prediction of resonance theory (solid line) compared with STARE radar (points) observations. The top panel shows the signal amplitude, the bottom panel shows the phase illustration from Walker [66].

The solid lines represent the theoretical prediction and the points represent the real data. The common source of ULF wave energy on the ground is field line resonance. It is necessary to understand the structure of the resonance in space, and how the ionosphere changes this structure. The phase of this wave on the ground changes rapidly in the North-South direction. More explanation is given in the next section.

4.4 Interaction of ULF wave with the ionosphere

The ionosphere is the ionized region of the upper atmosphere lying between about 90 and 500 km. It forms a shell of electrons and electrically charged atoms and molecules that surrounds the Earth and the inner boundary of the magnetosphere. The upper atmosphere was the most probable location of the electric currents that produce the solar-controlled variation in the magnetic field measured at the surface of earth. The conductivity along the magnetic field lines is expected to be very good, but there is also conductivity perpendicular to $\mathbf{B}$, as a result of collisions between the charged particles and the neutral atmosphere. The two types of current produced: the Pederson current is in the parallel direction to $\mathbf{E}$, and the Hall current is perpendicular to $\mathbf{E}$, in the direction of $-\mathbf{E}\times\mathbf{B}$. The Pederson current results from the acceleration of the ions and electrons in the direction of $+\mathbf{E}$ or$-\mathbf{E}$ after each collision. The Hall current results from the fact that both ions and

electrons try to $\mathbf{E} \times \mathbf{B}$ drift in response to an electric field applied perpendicular to $\mathbf{B}$.

The non-zero ionospheric field drives a Pederson current which shields the magnetic field displacements from the ground. The components of this current can be detected in the line of sight Doppler shift in echoes from HF coherent radars such as SuperDARN network and coverage by more than one radar allows the Pederson current in the plane normal to the magnetic field to be determined. HF coherent radars rely on the Bragg scattering of radio waves by small-scale ionospheric, magnetic field-aligned irregularities [35].

The ionosphere has a variety of effects on the waves seen on the ground [26]. The signal seen on the ground is an electromagnetic wave radiated from currents induced in the ionosphere, and not the hydromagnetic wave that was incident. The ionosphere can have a strong effect on the polarization of the wave. The incident toroidal mode will have its magnetic polarization in the East-West direction. The field-aligned current (FAC) driven by the Alfvén wave will close both North and South of the resonant shell via Pederson currents as shown in Figure 4.5. These currents produce ground perturbations that nearly cancel the ground perturbations of the field-aligned current [24].

The waves that have reached the high latitude ionosphere can cause perturbations propagating along the ionosphere to the middle and low latitudes. The ULF waves in the ionosphere possess a large skin depth scale many times larger than the characteristic vertical scale of the ionosphere. The magnetic effect of the Hall currents can be observed above the ionosphere, the magnetic field determined by a system of longitudinal currents closed in the ionosphere by the Pederson currents [24].

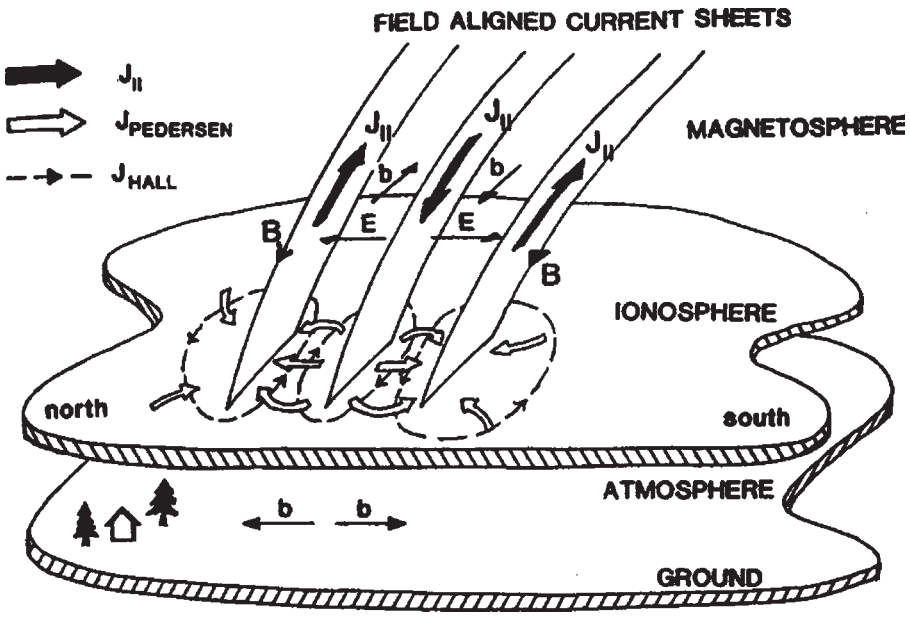

Figure 4.5: The ionospheric currents driven by a toroidal resonance illustration from McPherron [41].

The $\mathbf{J} \times \mathbf{B}$ force from the Pederson closure drives a vertical flow in the ionosphere. However

the ions suffer more collisions than electrons, then there is a Hall current in the opposite direction as shown by dashed lines in the Figure 4.5. The magnetic field effects of the Hall current are seen on the ground as a magnetic perturbation that has rotated 90° counter clockwise (CCW) relative to the field of the incident wave. Then the toroidal modes in the magnetosphere will have a North-South polarization on the ground. Another effect of the ionosphere is a consequence of a resonant cavity. The rapid increase in molecular weight from the top of the ionosphere down causes a reduction in Alfvén velocity from magnetospheric values. At the bottom of the ionosphere, the rapid decrease in electron and ion density causes an increase in Alfvén velocity up to the speed of light.

4.5 Cavity resonance

The boundaries within the magnetosphere form cavities that may resonate in response to external excitation. The modern concept of magnetospheric cavity mode was introduced by Kivelson [31], who proposed a simple box geometry with perfectly reflecting boundaries, in which the magnetosphere rings as a whole at its own eigenfrequency. Allan *et al* [6] suggested that, impulsive stimuli at the magnetopause can set up compressional cavity resonances which drive field line resonance (FLR) within the magnetosphere. The model was further developed for more realistic conditions. The cavity mode eigenperiods are determined by the cavity dimensions. The cavity has normal modes which are standing both radially and azimuthally as well as along field lines. However, because of the tail, the magnetosphere is more like a waveguide than cavity. Waves "stand" radially, but will propagate azimuthally and be lost down the tail. The real magnetosphere is extremely complex because of the asymmetric magnetic field with strong gradients in field and plasma. Its dimensions are continually changing in response to the solar wind so that cavity properties are very dynamic and as such, this cavity is unable to support stable eigen modes.

4.6 Summary

In the magnetosphere, the fast and Alfvén mode can interact to generate azimuthal standing waves. In this case the amplitude of the wave azimuthal component is enhanced. However as a result of the ionospheric rotation, the occurrence of such resonance processes should lead to an enhancement of the H-wave amplitude in the ground observations. The Pc5 ULF pulsations are a high-latitude phenomena, usually observable between $60 - 75°$.

Chapter 5

The SuperDARN HF Radars

5.1 Introduction

In this chapter, we introduce the HF radar. Data from this instrument will be used extensively in this thesis. The SuperDARN HF radar measures line-of-sight Doppler velocity, a parameter which can be employed to observe geomagnetic pulsations in the ionosphere.

5.2 The SuperDARN HF radars

The Super Dual Auroral Radar Network (SuperDARN) is an international collaborative network of HF radars that monitors ionospheric plasma convection over a major portion of the northern and southern polar regions. The SuperDARN network consists of 32 operational radars [5]. The names and locations of the SuperDARN radars are listed in Table 5.1 and the fields of view of the radars are shown in Figure 5.1. The SuperDARN radar network's vast coverage extends longitudinally over more than 18 hours of local time in the northern hemisphere and latitudinally from equatorward of the auroral electrojet to well into the polar cap, thus sampling the ionospheric footprint of many magnetospheric regions. The SuperDARN radar operation is divided into three different modes, namely, Common, Special and Discretionary time modes.

In the Common and fast common mode, the entire network operates in a mode that is accepted by all the Principal Investigators (PI's) as the most useful to the SuperDARN community. The common modes make up atleast 50% of the total operating schedule.

In Special mode, the radars are set into an agreed upon mode that seeks to address one specific scientific goal (e.g. Rocket launches, ULF pulsations, E-region measurements, satellite conjunction etc.). Special mode time is limited to 20% of the radar schedule.

Dicretionary mode, this time radars are allowed to operate independently from each other if there are specific needs of the individual PI's. Discretionary mode is limited to 30% of the radar schedule.

The "Scheduling Working Group" has the responsibility for acting on scheduling requests and drawing up a monthly operations schedule which is approved by the PI's. If a PI has no specific use for the radar in discretionary mode, it is usually set into the common mode operation.

Northern Hemisphere						
Name	Code	Geographic		AACGM		Boresite heaing
Adak East	ade	51.88	-176.62	47.31	-111.85	46.00
Adak West	adw	51.83	-176.62	47.26	-111.84	-28.00
Blackstone	bks	37.10	-77.95	47.03	-1.54	-40.00
Christmas Valley East	cve	43.27	-120.36	48.85	-57.14	54
Christmas Valley West	cvw	43.27	-120.36	48.85	-57.14	-20
Clyde River	cly	70.49	-68.50	78.49	19.03	-55.60
Fort Hays East	fhe	38.86	-99.39	48.14	-31.04	45.00
Fort Hays West	fhw	38.86	-99.39	48.14	-31.04	-25.00
Goose Bay	gbr	53.32	-60.46	60.50	23.66	5.00
Hankasalmi	han	62.32	26.61	59.20	104.75	-12.00
Hokkaido	hok	43.53	143.61	36.70	-143.84	30
Inuvik	inv	68.42	-133.50	71.63	-83.41	29.50
Kapuskasing	kap	49.39	-82.32	59.51	-7.00	-12.00
king Salmon	ksr	58.68	-156.65	57.42	-97.88	-20.00
Kodiak	kod	57.60	-152.20	57.08	-93.65	30.00
Prince George	pgr	53.98	-122.59	59.38	-62.97	5.00
Pykkvybaer	pyk	63.77	-20.54	64.40	67.42	30.00
Rankin	rkn	62.83	-92.11	72.45	-23.12	5.70
Saskatoon	sas	52.16	-106.53	60.56	-42.51	23.10
Stokkseyri	sto	63.86	-22.02	64.71	66.25	-59.00
Schefferville	sch	54.80	-66.80	63.16	15.79	15.00
Wallops Island	wal	37.93	-75.47	47.56	1.95	35.90
Southern Hemisphere						
Name	Code	Geographic		AACGM		Boresite
Dome C East	dce	-75.09	123.35	-88.73	50.27	115.00
Falkland Islands	fir	-51.83	-58.98	-38.92	10.38	178.20
Halley	hal	-75.52	-26.63	-62.18	29.97	165.00
Kerguelen	ker	-49.35	70.26	-58.63	123.64	168.00
Mcmurdo	mcm	-77.88	166.73	-79.95	-31.07	263.40
Sanae	san	-71.68	-2.85	-61.92	44.32	173.20
Syowa South	sys	-69.00	39.58	-66.60	72.45	165.00
Syowa East	sye	-69.01	39.61	-66.61	72.45	106.50
Tiger	tig	-43.38	147.23	-54.19	-132.43	180.00
Tiger Unwin	unw	-46.51	168.38	-53.99	-105.47	227.90
Zhongshan Station	zho	-69.38	76.38	-75.00	97.07	72.50

Table 5.1: Names and locations of the SuperDARN radars.

A complete description of the SuperDARN radar instrumentation is given in Chisham [13]. The HF radars of the system each operate on a frequency selected between 8 and 20 MHz band, and phasing matrix is used to sweep the beam through successive positions with azimuthal separation of 3.24° roughly depending on the operating frequency. Each SuperDARN radar runs through a 16 beam scan with a dwell time of between 3 and 7 s (depending on radar) which gives a full 16-beam scan that covers 52° in azimuthal once every 1 or 2 minutes, respectively. For each beam the backscatter power, line-of-sight Doppler velocity, and spectral width is gated up to 75 cells which are 45 km long in standard operation although there is an initial distance of 180 km for backscatter from the radar. The spatial coverage of each radar is around 2000 $\times$ 2000 km^2. HF radars operate by utilizing coherent scatter from field aligned irregularities of electron density in the E and F -regions of the ionosphere. They "see" the electric field perturbation associated with the pulsation and not the magnetic field. This has implications as to which kind of pulsations (compressional or Alfvén) are seen by the different beams. Their spatial coverage makes them ideal tool for resolving the resonance structures. The ultra low frequency (ULF) oscillations in these ionospheric regions are observable in the line-of-sight Doppler velocity, with the magnitude of the measured flow oscillations being dependent upon the direction of the flow oscillations relative to the beam direction.

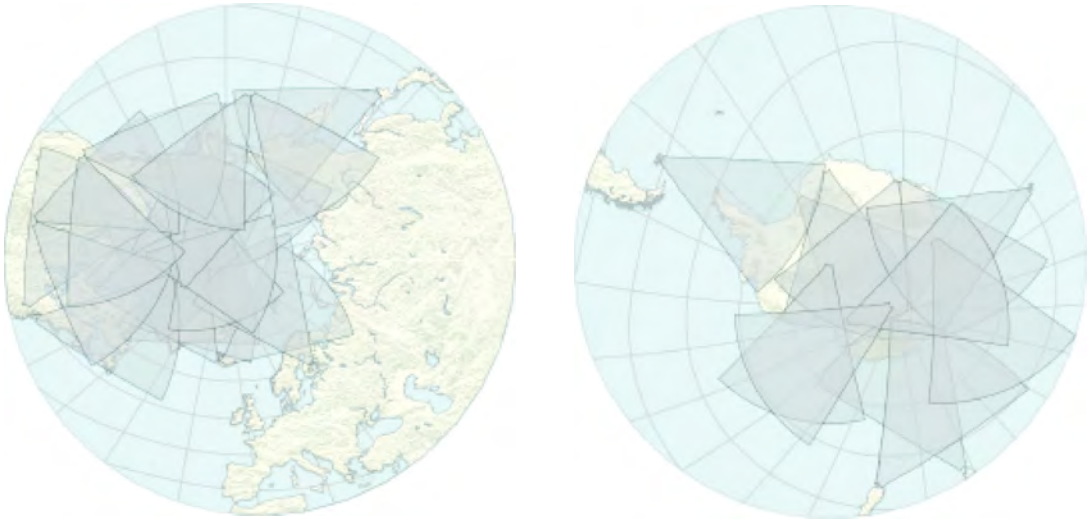

Figure 5.1: Fields of view of the northern and southern hemisphere SuperDARN radars source from the internet [5].

Each SuperDARN radar has a line of 16 line individual equal-spaced antennas constituting the main array that is used for transmission and reception of radio signal. Each radar site also has an inferferometer array of 4 similar antennas which is separated by 100 m from the main array and is parallel to it. Antennas have a height of 15.4 m above the ground and between each array the distance is also 15.4 m. Most of the SuperDARN radars have an additional array of four antenna interferometers that are used to make angle-of-arrival of radio wave measurements as shown in Figure 5.2. This is important for identifying the

HF propagation mode.

Figure 5.2: An example of antenna taken from kodiak radar site illustration from Parris [10].

Radar is an electronic system used to radiate electromagnetic signals for the purpose of detecting and locating a target. Depending on the radar transmission: there are two types of radar: continuous and pulsed. Pulsed radar is the type of radar that transmits electromagnetic signals in pulses by amplitude modulating an RF signal with a rectangular function. Continuous wave radar is the type of radar that transmits continuous electromagnetic signals. Depending on the targets, there are two types of radar incoherent and coherent.

5.3 Incoherent scatter radars

Incoherent scatter radar transmits into the ionosphere, each of the millions of electrons in the ionosphere illuminated by the beam acts as a very small target. The incoherent scatter radar uses frequencies well above the plasma frequency in the atmosphere. Large amounts of RF power at MW levels, are transmitted at UHF frequencies towards the ionosphere. The higher the density of the ionospheric plasma, the larger the returned power. Therefore it is the small amount of energy scattered by the ionospheric electrons which is detected by the incoherent scatter radar method. The principle between the mechanism of backscatter between incoherent scatter radars and HF radars of the SuperDARN network is the same.

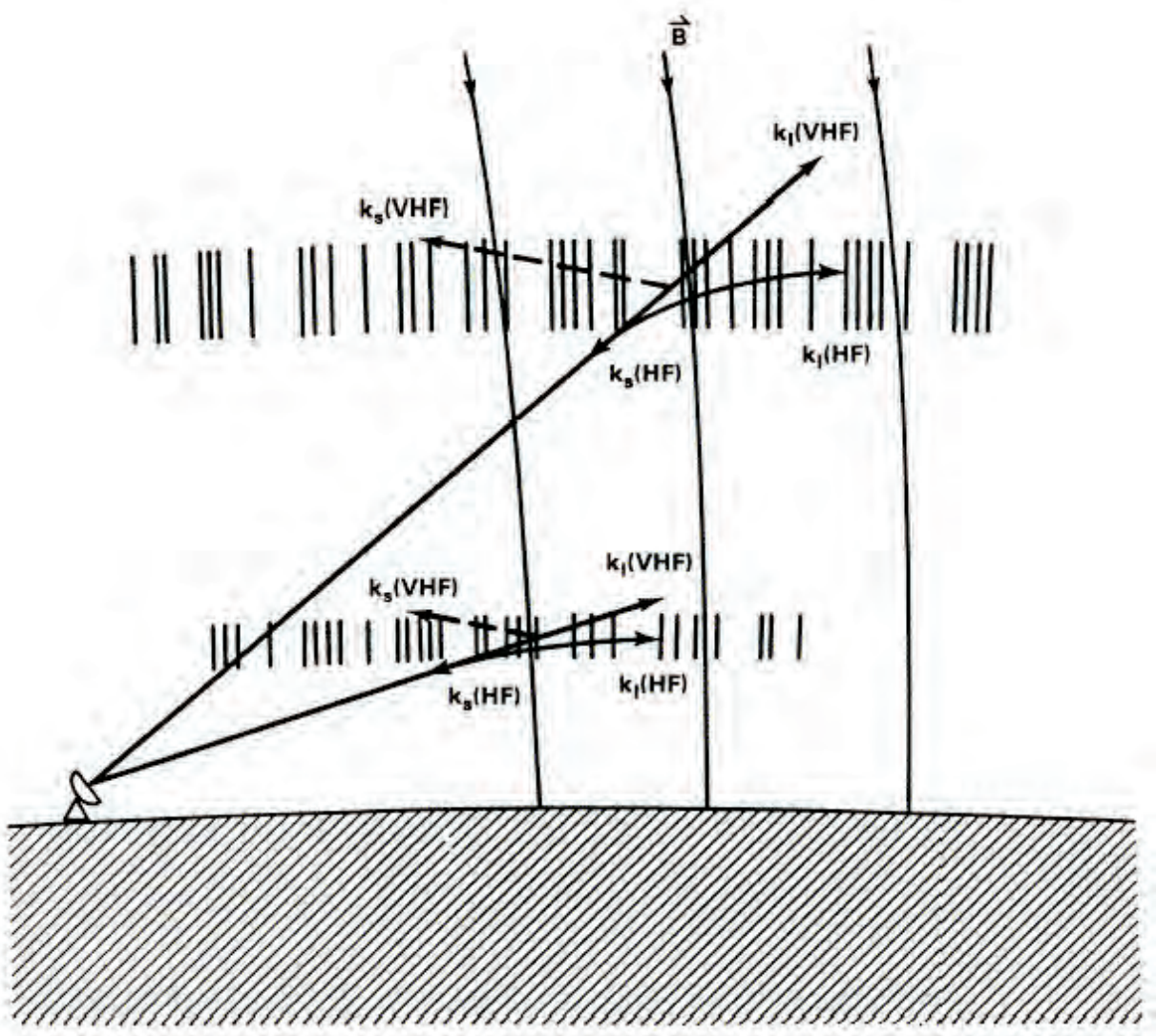

Figure 5.3: VHF and HF scatter from coherent ionospheric irregularities illustration from Greenwald [25].

5.4 Coherent scatter radars

Coherent-scatter radars are sensitive to Bragg scattering from small-scale electron density irregularities in the ionosphere. The scattering wavelength is one half the transmitted wavelength, meaning that backscatter occurs when the ionospheric irregularities have a separation of approximately one half of the radar wavelength (constructive interference).

An example:

A medium frequency radar operating at 10 MHz. This gives wavelength

$\lambda = \frac{c}{f} = \frac{3.10^8 m/s}{10MHz} = 30m$

which means that this radar will give backscatter when the ionospheric irregularities are in the size of $\sim$ 15 metres.

Ionospheric irregularities are noted for their magnetic field-aligned structure, and the radar wave vector must be very nearly orthogonal to the magnetic field. In the case of coherent radars, the targets are not the ionosphere vertically above the radar but rather the signal is directed horizontally towards the scattering regions where coherent interference from partially scattered signals constitutes significant backscatter power.

At the lower frequencies, ionospheric refraction allows the orthogonality condition to be satisfied in both E and F-region of the ionosphere as shown in Figure 5.3. The Figure illustrates that the nearly vertical magnetic field scattering at high latitudes leads to non orthogonal scattering at VHF and high frequencies with scattered signal propagation into space. The refraction that occurs at HF causes the radar signals to become orthogonal to the magnetic field lines and can thus be returned to the radar.

For a particular angle of incidence, an HF ray is refracted along a curved path as shown in Figure 5.4. Along of its path the scatter from the irregularities is at an angle to the incident ray as seen in points A and C, however it does not return to the location of the radar. At point B, the incident ray is at right angles to the magnetic field, and the backscatter signal is returned along the same path to the radar receiver. If the transmitted signal is a beam with a wide range of angles in the vertical plane, then reflection occurs from many different ranges corresponding to the different angles of incidence in the beams.

The focus in this thesis is on the geomagnetic pulsation signatures observed in the scatter and not on the causes of irregularies.

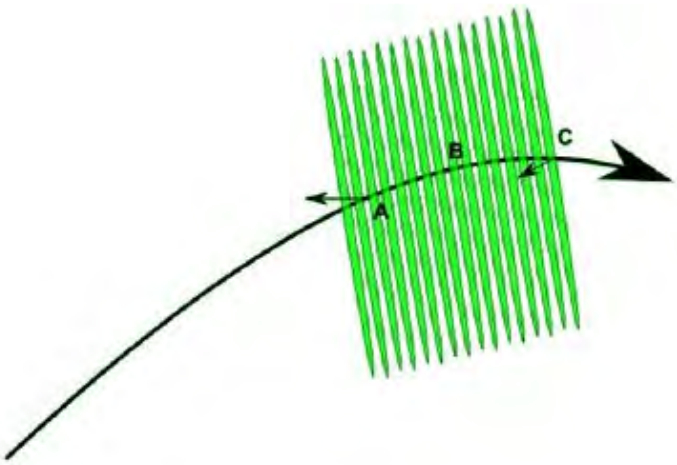

Figure 5.4: Effect of ionospheric reflection on direction of backscatter. The signal is orthogonal at B but not A and C illustration from Walker [62].

5.5 Ionospheric sounding by pulsed radars

The three principal parameters determined by the radars are the line-of -sight component of the Doppler velocity along the beam, the backscatter power and the spectral width

of the signal. The complex autocorrelation function (ACF) of the received signal is used to determine these parameters in each of the SuperDARN range cells. The technique by which this is achieved utilises a multi-pulse transmission sequence. During the common mode of operation, the radars transmit a seven-pulse sequence of the form illustrated in Figure 5.5.

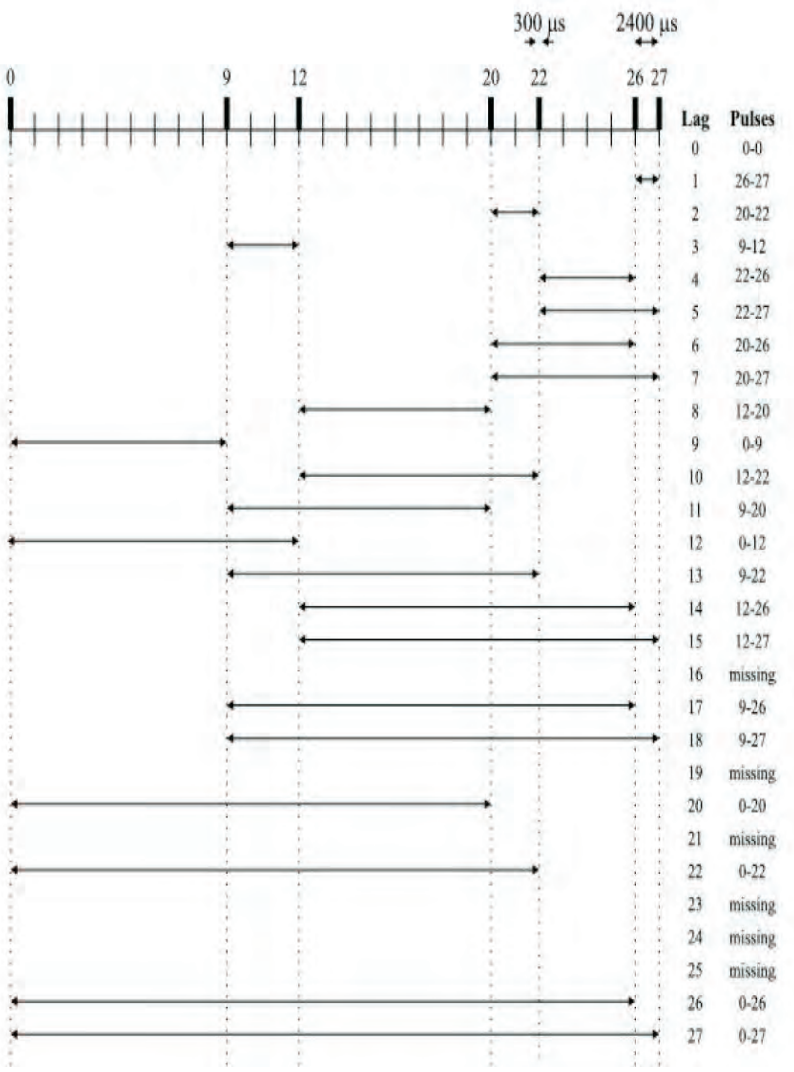

Figure 5.5: The staggered pulse pattern showing how various ACF lags can be created from 7 -pulses. The pulses are $300\mu s$ long and they are separated by integral multiples of the lag time, τ, which is normally set to $2400\mu s$.

Each transmitted pulse has a duration of 300 µs that determines the length of range gate. During the common mode of operation the radars transmit their seven-pulse pattern (0, 9, 12, 20, 22, 26, 27) during a 100 ms transmission window. After each pulse is transmitted

the radars switch to receiver mode and the return signal is sampled periodically and processed in order to reduce the ACF for each range, each a function of the lag time. For a 7 second dwell time the multi-pulse sequence is usually repeated 70 times at each beam position and the 70 resulting ACFs are integrated and averaged to increase the signal to noise ratio.

The pulse separation of a multi-pulse pattern is chosen in such a way as to maximise the number of unique lags between the pulses. For example, the seven-pulse pattern illustrated above has lags for all integral multiples of the lag times except for 16τ, 19τ, 21τ, 23τ, 24τ and 25τ, which are missing. For this reason, SuperDARN uses only the first 18 lags to determine the ACFs for the pulse sequence. Once the pulse sequence has been completed, an auto correlation function is generated for each range.

5.6 Pulsation in radar data

The range-time summary plot is given in Figure 5.6. The plot gives a good indication of the operation of the radar for a given time on a specific beam. This Figure illustrates the range-time plot for Doppler velocity as a function of time for beam 12 of the Sanae radar. The strong backscatter is received over a range of latitude between 65.4° and 68.7° over the period shown. In this period the pulsation activity was strongest. Pc5 pulsations can be seen as alternating bands of positive and negative (shades of blue and red) Doppler velocity.

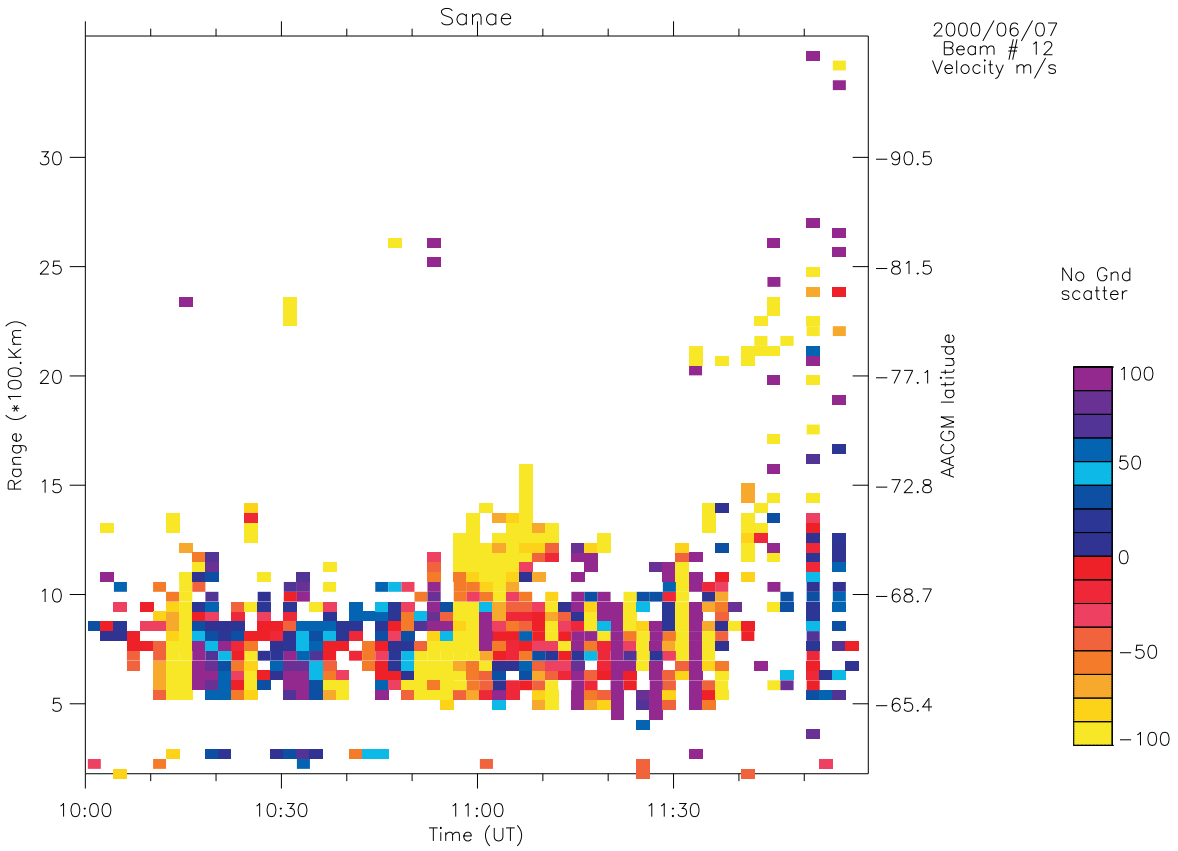

Figure 5.6: SANAE Range-time summary plot for 7 June 2000. A two hour subset of Beam 12 Doppler velocity is plotted to illustrate pulsations.

5.7 Summary

If a field line pulsation occurs on the magnetic field lines that pass through the ionosphere being monitored by the SuperDARN HF radars, then the associated pulsating E field will cause the local bulk ionosphere to move with an E×B drift. The field aligned irregularities at ionospheric heights will also experience this force and will move with varying veloocity. This movement is manifested as a periodic variation in the line of sight Doppler velocity recorded by SuperDARN radar.

Chapter 6

Ground-based magnetometers

6.1 Introduction

The setting-up of ground-based magnetometers made a qualitative change in the way that magnetic field data could be used to understand geomagnetic pulsations. The key to understanding wave phenomena is a data set consisting simultaneous spatial and temporal information. The ground-based magnetometer instruments used in this study comprised fluxgate magnetometers from Greenland, Canadian Array for Realtime Investigations of Magnetic Activity (CARISMA) and International Monitor for Auroral Geomagnetic Effects (IMAGE).

6.2 Magnetometers

Magnetometers have been used for studies of currents in the close Earth for more than a century. They monitor variations of the Earth's magnetic field of the time scale from a fraction of a second to a daily variation. The ground-base magnetometer signatures are the Biot-Savart integral of the ionospheric and non-ionospheric currents. The ground based magnetometer responds to ionospheric currents over a large area since the magnetic field from each source region only falls off inversely with distance. There are two basic types of magnetometer: one for measurements of relative changes of the geomagnetic field (fluxgate magnetometer) and the other one for measurements of absolute values of geomagnetic field (proton magnetometer). Ground based magnetometers are technically a remote sensing system as they measure the Earth's magnetic field.

The fluxgate magnetometer is ideal for the study of ULF waves since the sampling frequency of either 1 Hz or 0.1 Hz is at least an order of magnitude higher than mHz frequencies of interest. A resolution of 1nT is usually sufficient for detecting ULF waves on the ground. Early work on ULF pulsation analysis was done using magnetometers [59][52]. Although magnetometers are limited in their spatial resolution [28], they can still provide

a mechanism for corroborating the occurrence of pulsation events as well as providing pulsation data when radars have data gaps due to lack of ionospheric scatter.

6.2.1 Greenland

Danish Meteorological Institute (DMI) operates the Greenland magnetometer array, including 17 variometer stations and 3 geomagnetic observatories. The array consists of a West Coast chain with 12 stations including three observatories between 77.47° and 61.16° geographic north. On the East Coast variometer stations are located between 81.6° and 65.6° geographic north. The Greenland array covers polar cap, cusp and auroral regions. These data allow the monitoring of electromagnetic processes in the polar ionosphere and magnetosphere, and are a significant contribution to global databases e.g. SuperMAG. Figure 6.1 shows a map of the locations of the East and West Coast Greenland magnetometers.

The vast majority of the sensors employed are three axes line-core fluxgate magnetometers. They are optimised for long-term stability rather than high sensitivity. During setup, the components are magnetic north (H), local magnetic east (E) and vertical down (Z). The instruments run fully automatically and require no manual intervention. The sampling rate is 20s, and the magnetic components have a resolution of 0.01nT, as stated by DMI. The magnetic observatories (□ boxes) are those that are of interest for analysis in this thesis.

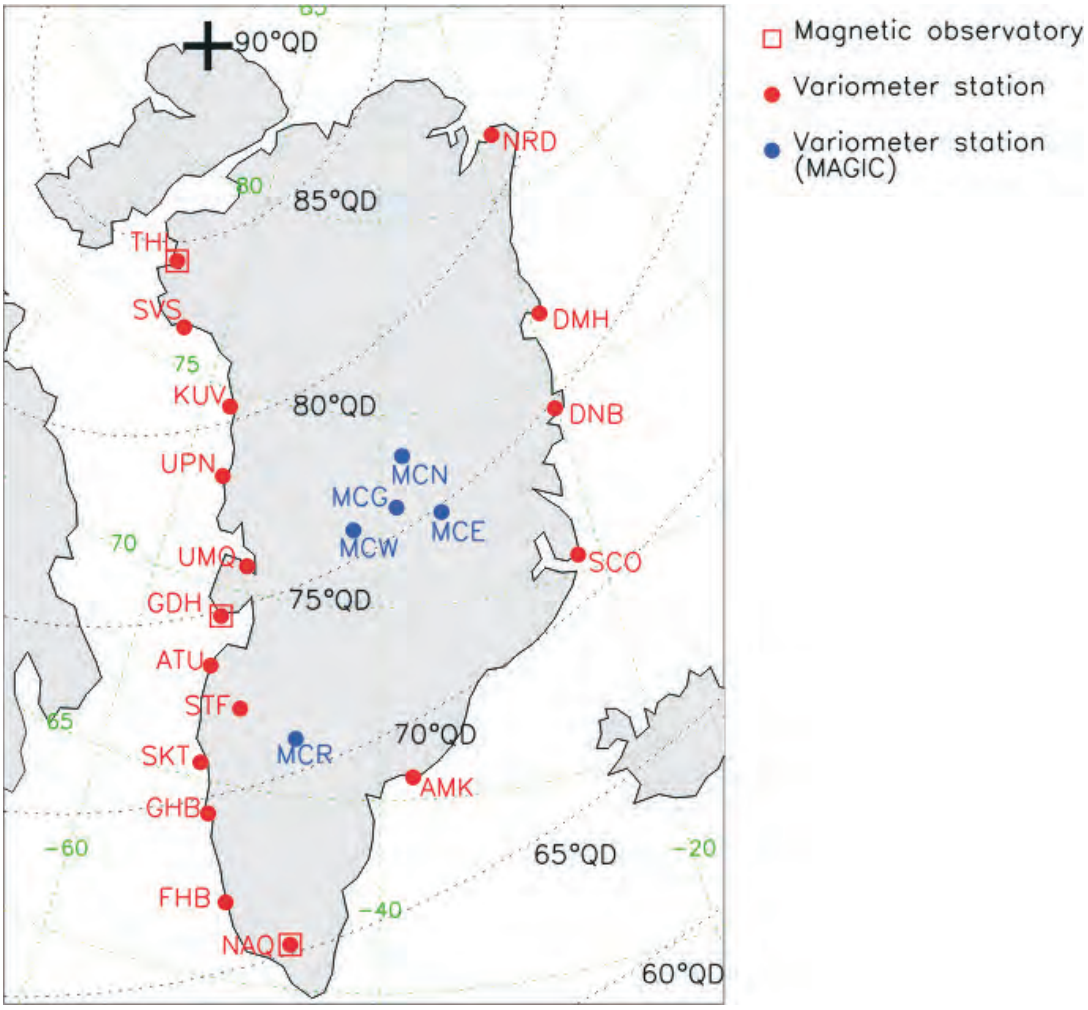

Figure 6.1: Location of the Greenland ground-based magnetometers source from the internet [2].

6.2.2 CARISMA

The Canadian Array for Realtime Investigations of Magnetic Activity (CARISMA) is the continuation of the CANOPUS magnetometer array which ran from 1986 to 2005. The operation of the magnetometers and collection of the data is now the responsibility of the Space Physics Group at the University of Alberta. The data are collected and stored locally on a data logger before being transmitted to the University of Alberta via CGSM information infrastructure(ITI) and satellite internet link.

The fluxgate magnetometer measures 3 components of the Earth's magnetic field in the geographic frame of reference, namely X (geographic north), Y (geographic east) and Z (vertical downward). Figure 6.2 shows a map of the locations of these magnetometer stations. The data sampled at 8 Hz and the instruments bandwidth is 0-2 Hz with an amplitude resolution of 0.025 nT. The sampling rate of CARISMA data is a 5 second resolution.

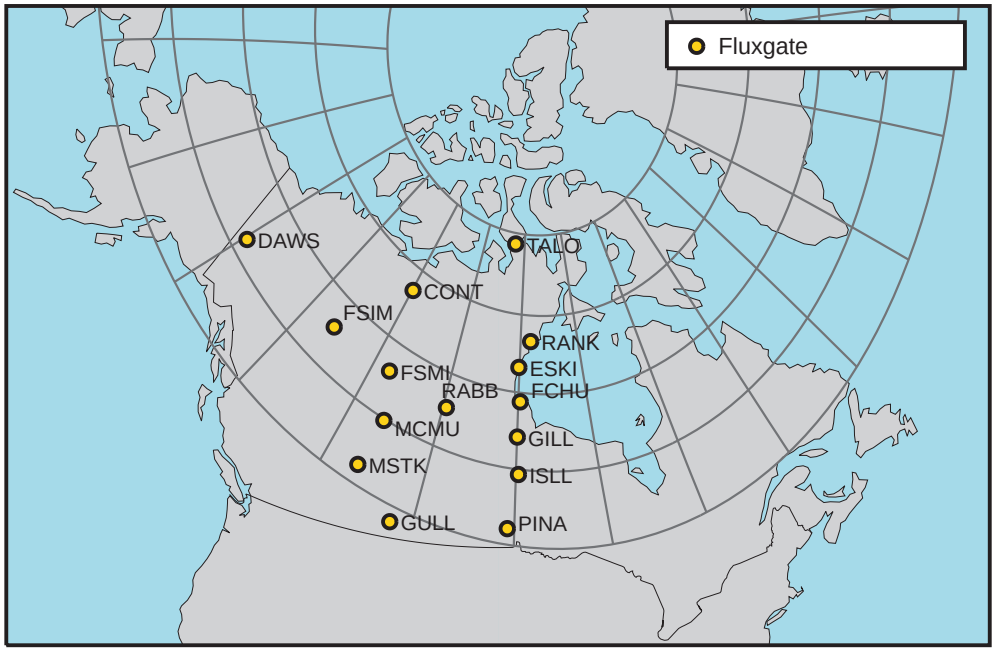

Figure 6.2: Location of the Canadian CARISMA magnetometers source from the internet [1].

6.2.3 IMAGE

The International Monitor for Auroral Geomagnetic Effects (IMAGE) consists of 31 magnetometers maintained by 10 institutes from Finland, Norway, Russia and Sweden as shown in Figure 6.3. The prime objectives of IMAGE are to study auroral electrojects and two-dimensional current systems in the northern auroral zone. The long profile covering geographic latitudes from 58 and 79 degrees is especially favourable for electrojects studies. Together with other ground-based recordings (by radars, riomatere, all-sky cameras) and satellite observations, IMAGE is an essential part in the investigations of high-latitude magnetospheric physics. About ten IMAGE stations are permanent observatories fulfilling international standards for absolute values of the field components. The other stations are considered as variometers with occasionally performed absolute measurements.

The IMAGE data are sampled every 10 s in geographic (X, Y and Z) components and are rotated into the geomagnetic (H, D and Z) components before analysis.

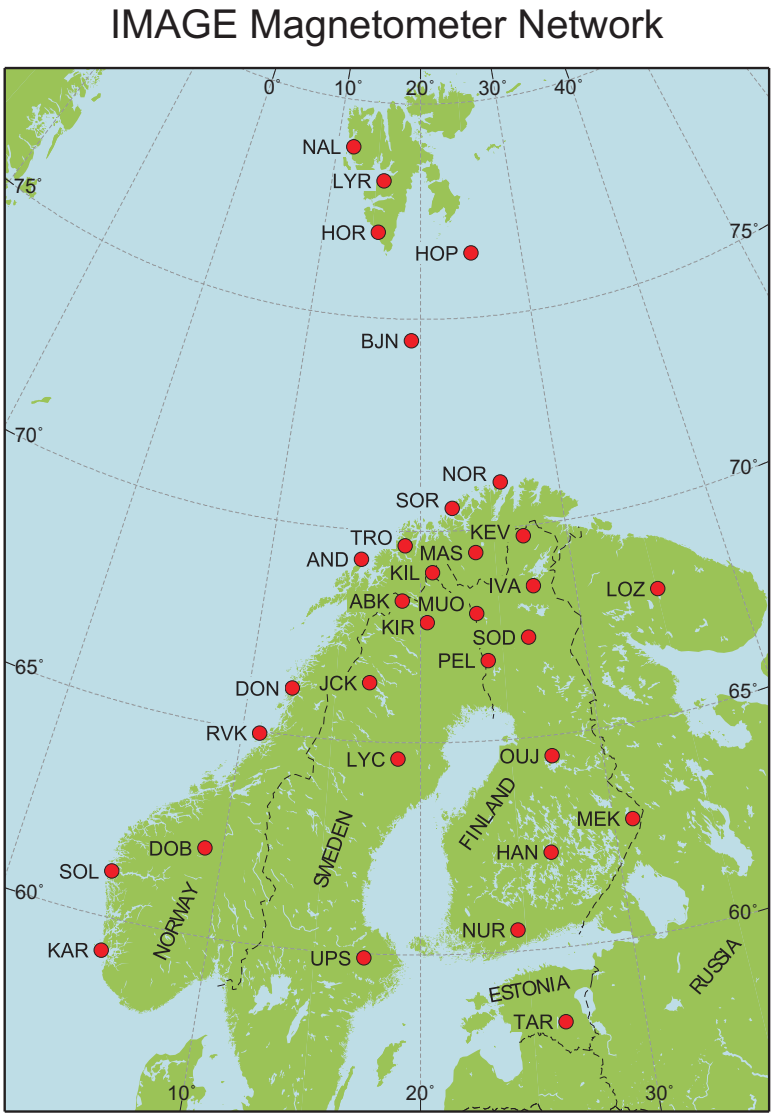

Figure 6.3: Location of the IMAGE ground-based magnetometer network source from the internet [3].

6.3 Summary

In this thesis we perform a data search of the SuperDARN HF radars by employing the Automated Pulsation Finder (APF) program. This highlights significant pulsation events. The nature and characteristics of the pulsation are then confirmed by correlating the data events seen in the HF radar with ground-based magnetometer chains. Although ground-based magnetometers are limited in their spatial resolution [28], they can still provide a mechanism for corroborating the occurrence of pulsation events as well as providing data when, due to lack of scatter the HF radar system cannot observe.

Chapter 7

HF radar observations

7.1 Introduction

In this section we present three Pc5 pulsation events observed using SuperDARN HF radars together with magnetometer data. Events are identified by using the pulsation finder to find a significant pulsation in one radar and then proceeding to search for a similar resonance in other radars at the similar magnetic latitudes. The events occurred on 06 October 2006 at 20:00-22:00 UT, 06 October 2006 at 16:00-18:00 UT and 14 September 2006 at 18:00-20:00 UT. The events are presented in order of good data quality, starting with the best. All three events are analysed in the same detail, by combining data from both instruments in order to determine their wave number, phase velocity and other characterictics.

7.2 The Event of October 06, 2006 (20:00-22:00 UT)

7.2.1 Pulsation finder results

The SuperDARN FIT data were used as the primary data source for this analysis. The pulsation finder was used to locate pulsation events in the SuperDARN data. First clean the data, the data cleaning were two step process. First noise was removed from the data then all non-suitable radar scatter was removed. A noise filter was used to remove spurious data points. The noise limit was determined by taking the average of all the data points $\pm$ three standard deviations. If the value was greater or less than the noise limit it was recarded. The process was repeated until there were no outliers. Ground scatter was not excluded from the analysis as it has been shown that pulsations may be visible in such scatter [45]. The SuperDARN radar produces a FIT file every two hour, that means there are $16\times75=1200$ possible two hour data series. After cleaning the data, check how full data series are; outliers have been removed, echoes with a spectral width of

greater than 150 m/s have been removed. For each data series, the remaining data series fill more than 80% of the two hour cell record, interpolate the missing points using cubic spline interpolation. Re-sample the data series so that there are 7200 samples between the first and the last samples of a two hour record. The value of 7200 was chosen so that there would be at most 1 second between the re-sampled data series in the two records. Re-sampling of the original data series do not change the spectrum in window of interest because the upper limit of window of interest follows below the Nyquist frequency of the original data. Filter the re-sampled data between 1mHz and 5mHz data using a windowed filter based on the Kaiser window. Create a spectrum of the filtered data using the IDL FFT routine and use the peak-detecter to determine if there is any significant peak in the spectrum in the frequency 1-5mHz band. The significant level was then set to be average plus three standard deviations of the data. If there were any amplitude values in the 1-5 mHz that fall above the significant level then the frequency that corresponded to the amplitude was considered a significant.

The investigation started by using an Automated Pulsation Finder program [36]. The Pulsation Finder highlighted a significant peak in beam 10 and range gate 32 of the Goose Bay radar. Although the pulsation was initially detected in beam 10, we chose to only analyse cells that were aligned along specific magnetic latitude. Each record of data corresponding to a beam number and the range gate to be processed by Automated Pulsation Finder has an uneven sampling period, due to periods of no backscatter, and the original data record is not always suitable for pulsation analysis. The temporal resolution of the data used in the pulsation finder is 1 s. This higher time resolution has no impact on the frequencies of interest here. The results of the Pulsation Finder are shown in Figure 7.1 which shows the line-of-sight Doppler velocity recorded at the Goose Bay, filtered in the Pc5 band, and its corresponding power spectrum.

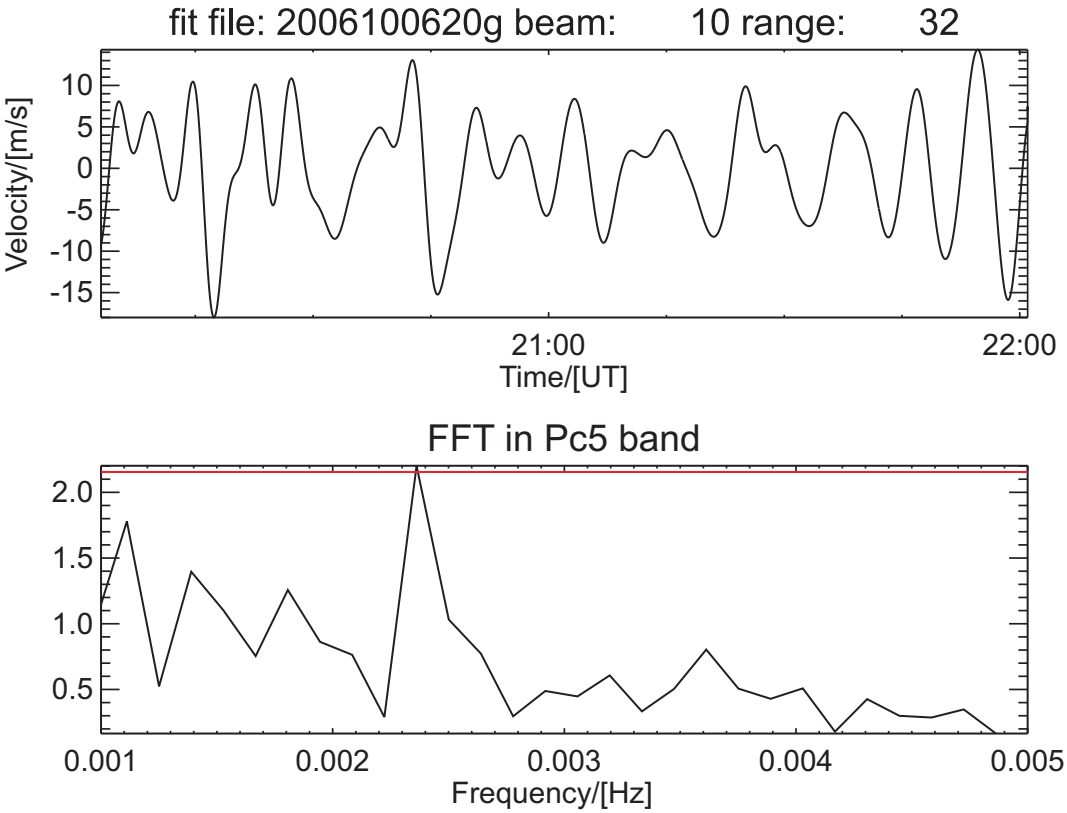

Figure 7.1: The top panel shows Pc5 band filtered data and the bottom shows the corresponding power spectrum and the significant limit level from filtered data. The peak detector recorded the peak in frequency band 2.2-2.5 mHz as significant.

The red line shows the level at which peaks in the spectrum are significant. In our data the detector recorded a significant resonance in the frequency band 2.2-2.5 mHz in beam 10 in range gate 32.

7.2.2 Time range summary plot

Figure 7.2 shows a full scan of the Goose bay radar field of view (fov). The range gates are presented in kilometers (km). Doppler velocities are colour coded. The beams are numbered from west to east in the field of view of the radar. The solid ellipse indicates the place where the Pc5 pulsation event was first highlighted.

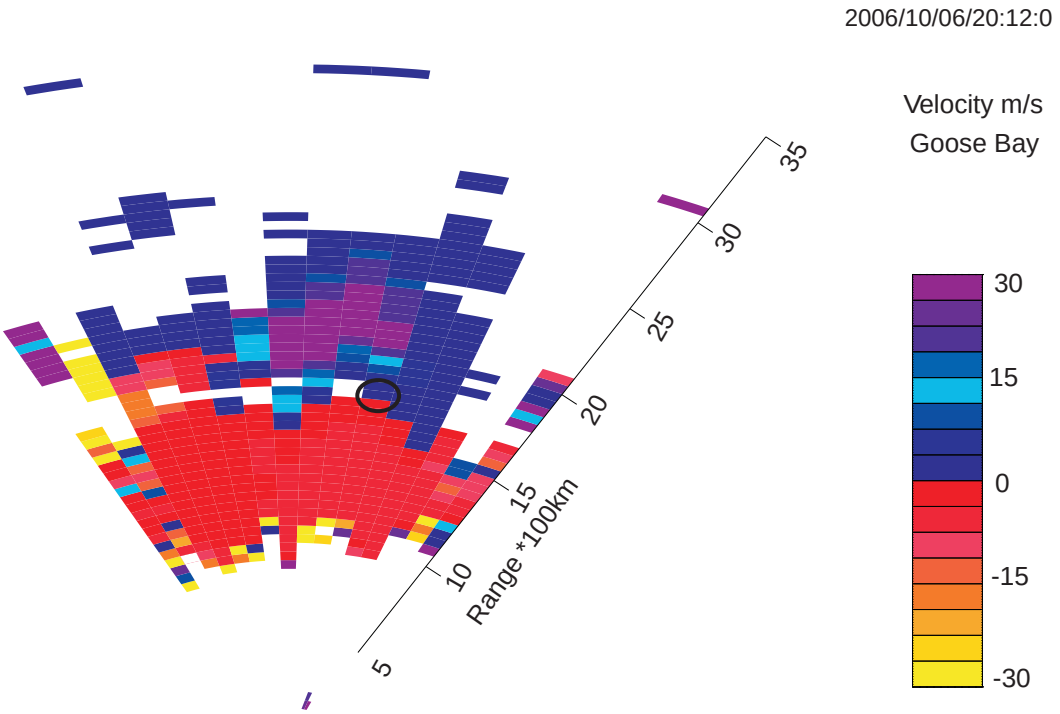

Figure 7.2: A beam-range of Doppler velocity in the field of view of Goose Bay radar, for the scan at 20:12 UT.

The range-time summary plot of line-of-sight Doppler velocity of beam 10 of the Goose bay radar is shown in Figure 7.3. The line-of-sight Doppler velocity is indicated by the colour bar on the right of the Figure. Blue indicates velocities moving toward the radar, while red corresponds to the velocities moving away from the radar.

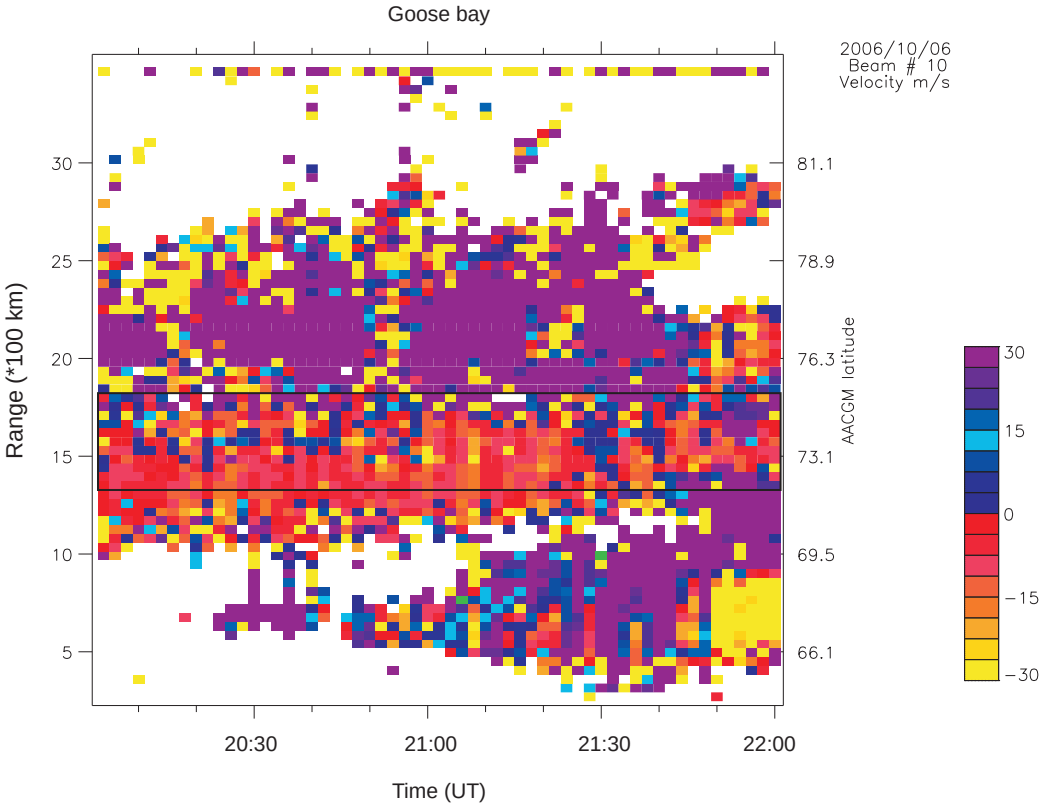

Figure 7.3: A time-range summary plot of Doppler velocity measured by beam 10 showing range gates and AACGM latitude.

The time-range plot is a reliable source to check pulsation activities. The solid rectangle shows the location of pulsation activity in this beam. The ionospheric perturbations visible in the range-time plot as bands of alternating positive and negative (shades of blue and red) Doppler velocities, are characteristic of Pc5 pulsations.

7.2.3 Latitude profiles of the amplitude and phase of the resonance

Figure 7.4 shows latitude profile of amplitude and phase along beam 10 of Goose Bay. This plot is derived from range gates 28 to 34 data excluding range gate 30 from beam 10. This is done using an analytic signal. From the analytic signal the amplitude and phase of the signal were extracted. More explanation about analytic signal is given in Chapter 9. In this event, we used the frequency band 2.2-2.5 mHz in calculating the analytic signal. The solid line represents the fitted curve, which shows the characteristics of field line resonances (FLRs). The region of resonance is clearly visible as a narrow peak in amplitude around 73.7 degree magnetic latitude with a standard phase change with increasing latitude, i.e., a decrease in phase as the resonance is crossed. Beam 10 is selected for analysis as it is meridionally aligned. In the case of the other radars we could not plot the latitude profile of amplitude and phase because there were not enough cells that were meridionally aligned or close to each other.

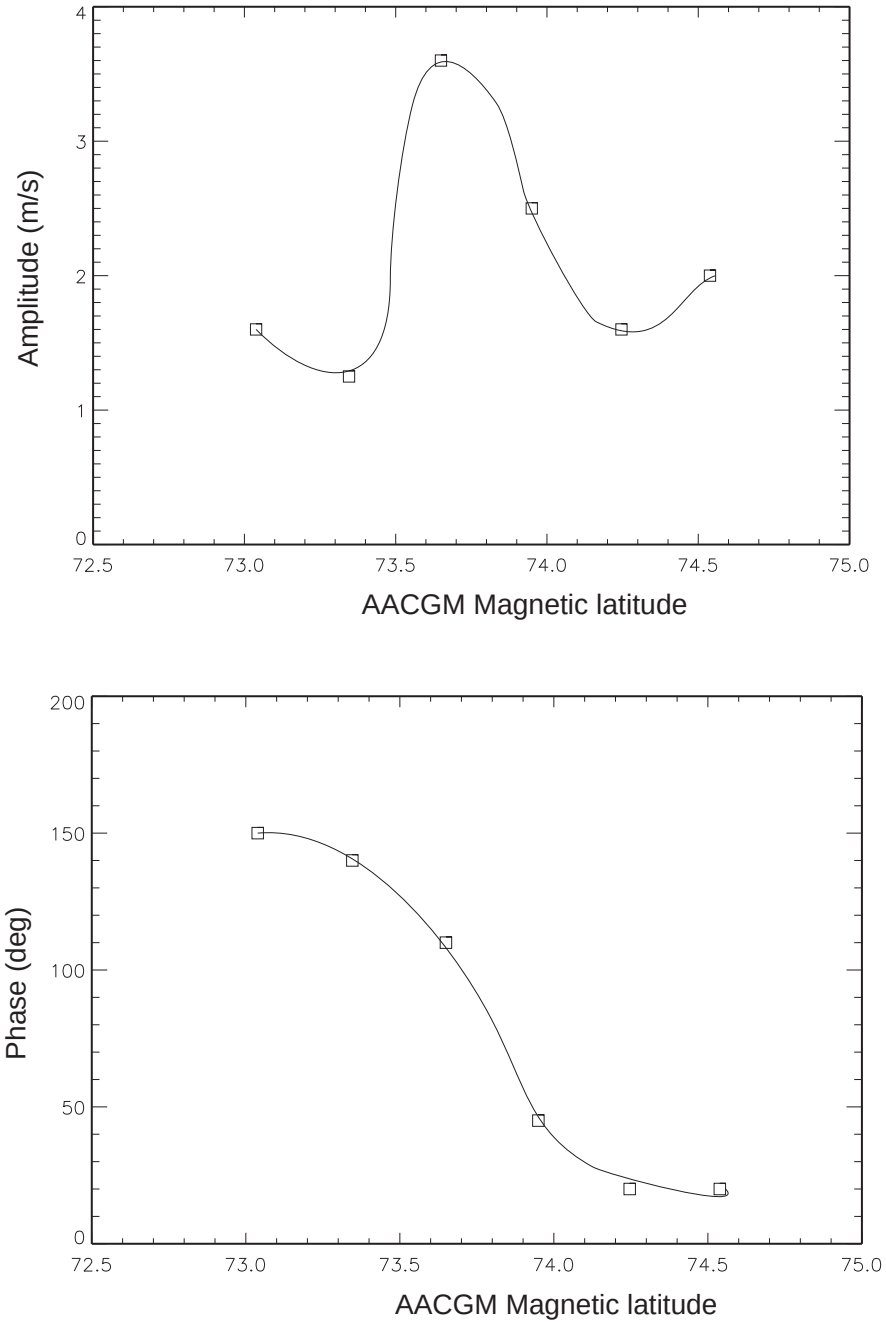

Figure 7.4: Latitude profile of amplitude and phase along beam 10 (beam most aligned with the magnetic meridian) of Goose Bay.

7.2.4 Map of HF radars used

In Figure 7.5, we show a geographic map outlining the field of view of the three SuperDARN radars; Saskatoon, Goose Bay, and Pykkvibaer, and locations of the magnetometer stations of the CARISMA, Greenland and IMAGE arrays. The analysis of data from magnetometer stations will be discussed in the next chapter. These radars have a good spatial resolution over a large range of magnetic latitude and longitude. Once we identified the

Pc5 ULF pulsation event in one radar (Goose Bay), we then proceeded to analyse all the beams and range gates of the Saskatoon and Pykkvibaer radars which were located within the same range of magnetic latitudes (i.e. within the solid red lines of Figure 7.5).

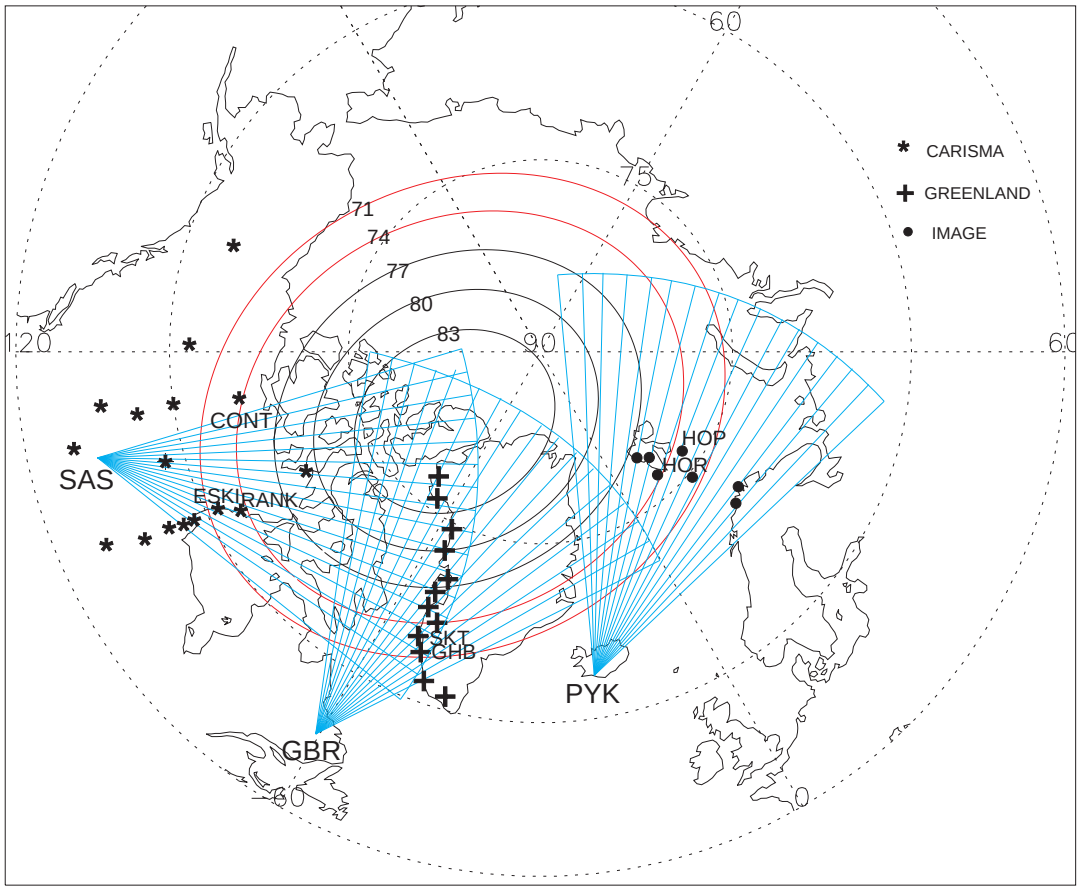

Figure 7.5: Fields of view of the SuperDARN radars at the Saskantoon (SAS), Goose Bay (GBR) and Pykkvibaer (PYK) plotted in geographic coordinates. The solid lines are AACGM magnetic latitude. AACGM stands for 'altitude adjusted corrected geomagnetic'.

7.2.5 Time series and their corresponding spectra

Figures 7.6 and 7.7 show time series of Doppler velocities for different beams and range gates at the magnetic latitudes of interest of the Goose Bay and Saskatoon radars. Before the time series analysis, the data were interpolated for the missing data. The Hanning window was applied to minimise the leakage. The Fourier analyser was applied through IDL FFT to compute the spectrum. The time series were analysed to obtain power spectra that are similar to the one observed using APF as shown in Figure 7.8. The beam and range gate plots presented here are in the same range magnetic latitude and showed peaks in the 2.2-2.5 mHz range frequency band.

The data used in these plots have a time resolution of 120 s. This puts an upper frequency limit of 4.17 mHz on the pulsation that can be observed.

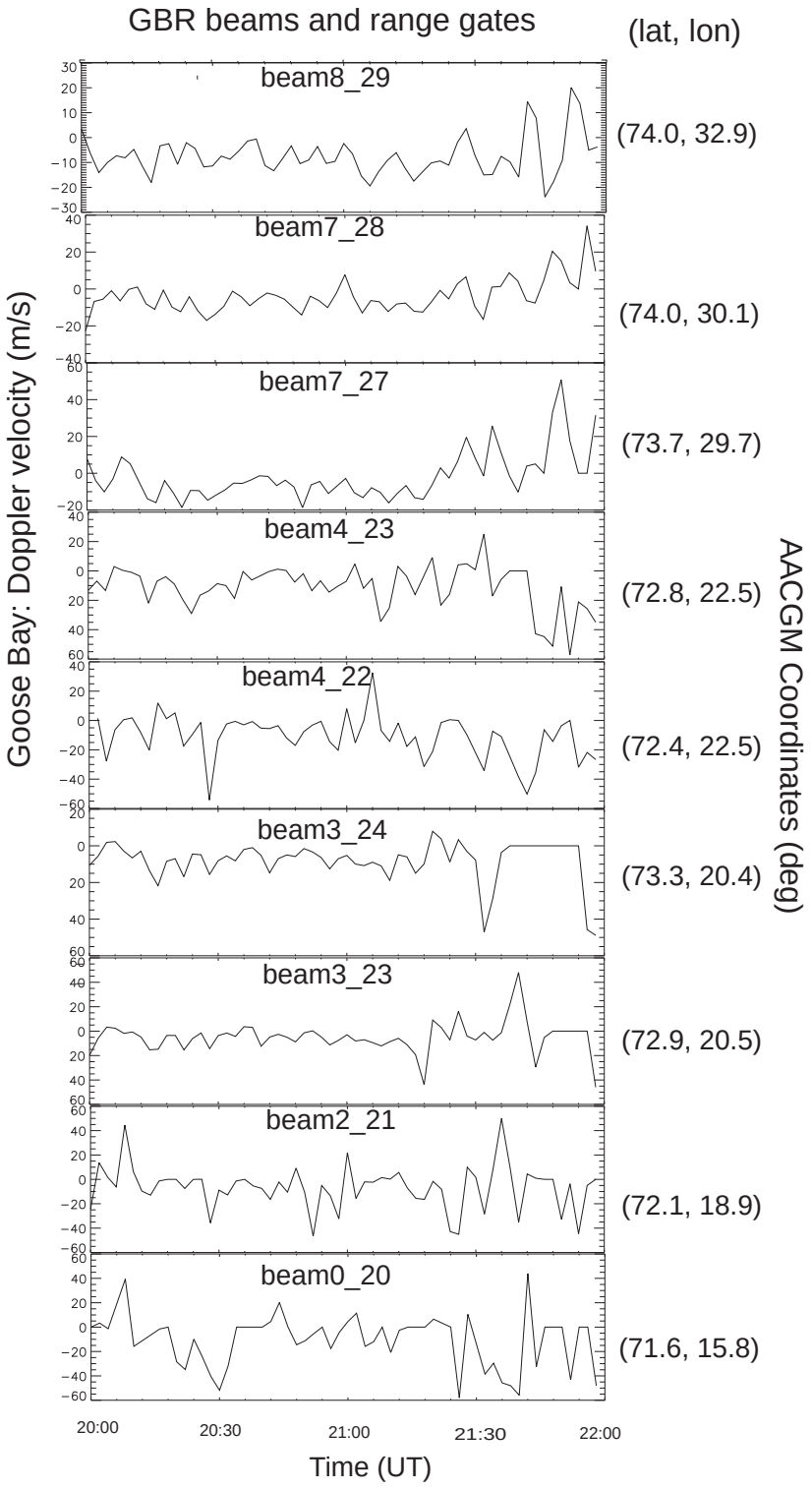

Figure 7.6: Doppler velocities, as functions of time, measured in the indicated beams and range gates of the Goose Bay radar.

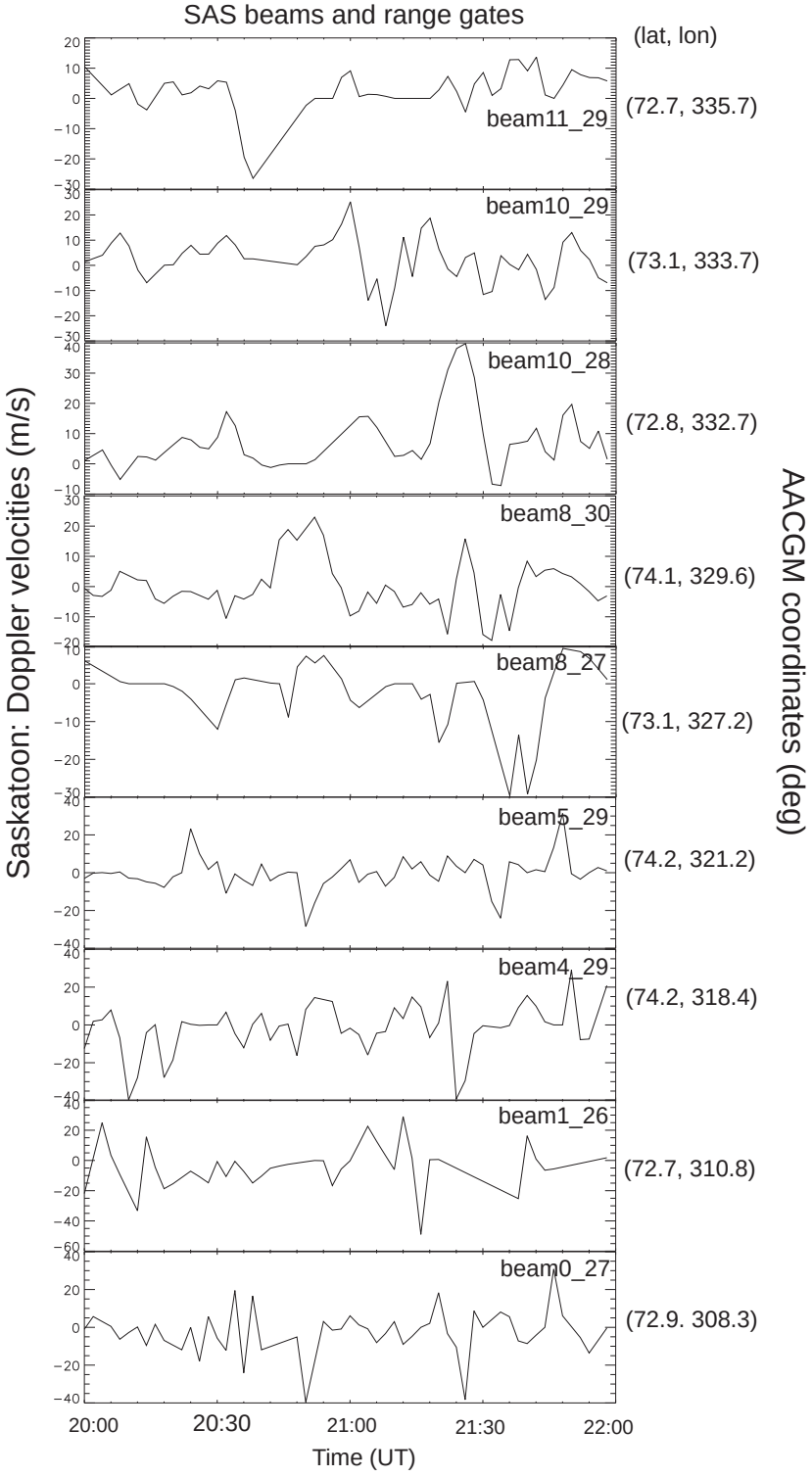

Figure 7.7: Doppler velocities, as functions of time, measured in the indicated beams and range gates of the Saskatoon radar.

The investigation of the Pc5 pulsation event observed on the Goose Bay radar was extended to two other radars in the same magnetic latitudes. Velocity data from 20:00 to 22:00 UT from these three radars were passed through a Fourier analysed to obtain the power

spectra. The results from Goose Bay (GBR), Saskatoon (SAS) and Pykkvibaer (PYK) radars are shown in Figures 7.8, 7.9 and 7.10. The shading highlights peaks in the 2.2-2.5 mHz observed by Saskatoon and Pykkvibaer radars in the beams and range gates plotted in these Figures.

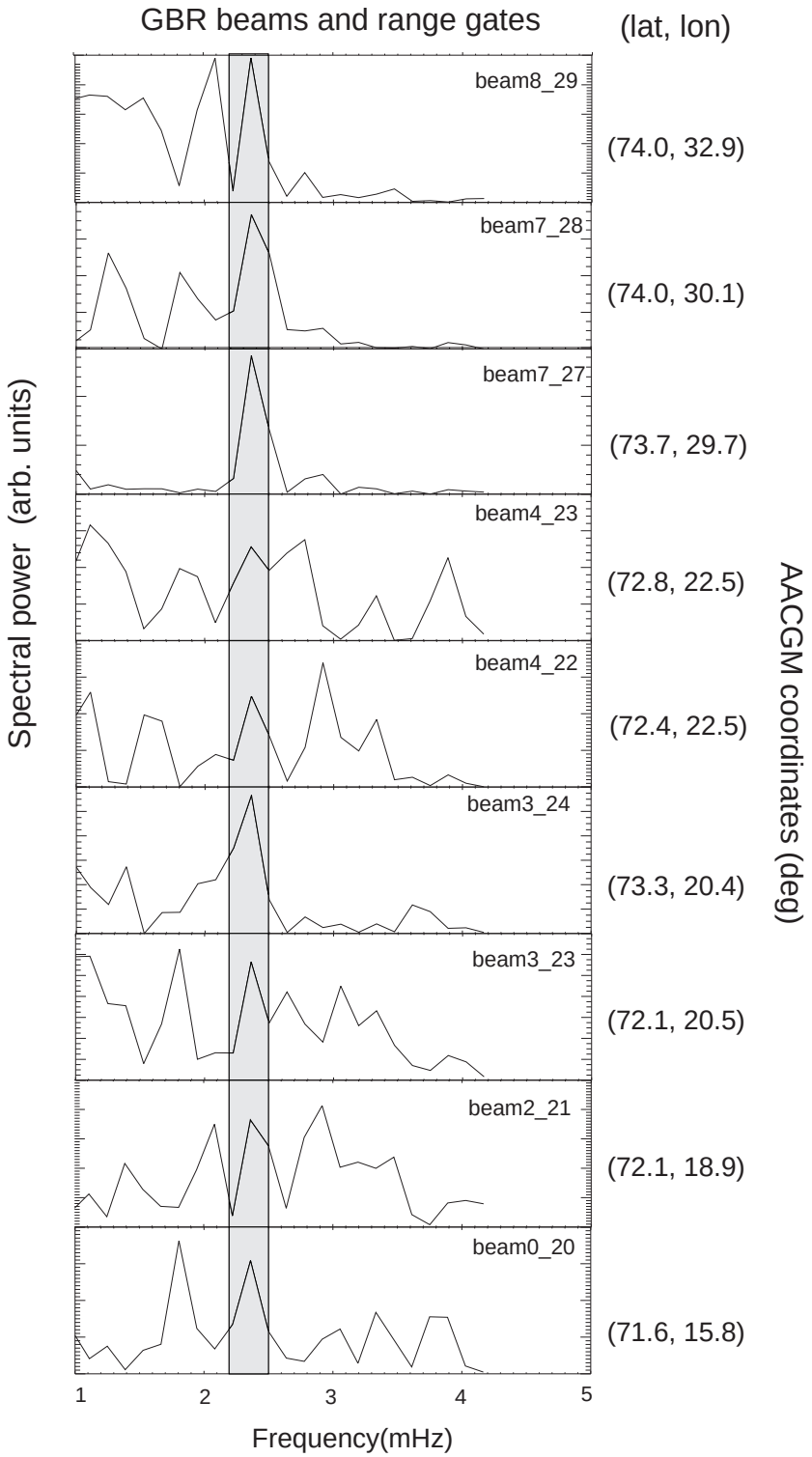

Figure 7.8: Spectral power observed in the indicated beams and range gates of the Goose Bay radar. The geomagnetic coordinates of the centre of each range gate on the right hand side. The shaded frequency range highlights the consistent peak in the 2.2-2.5 mHz band.

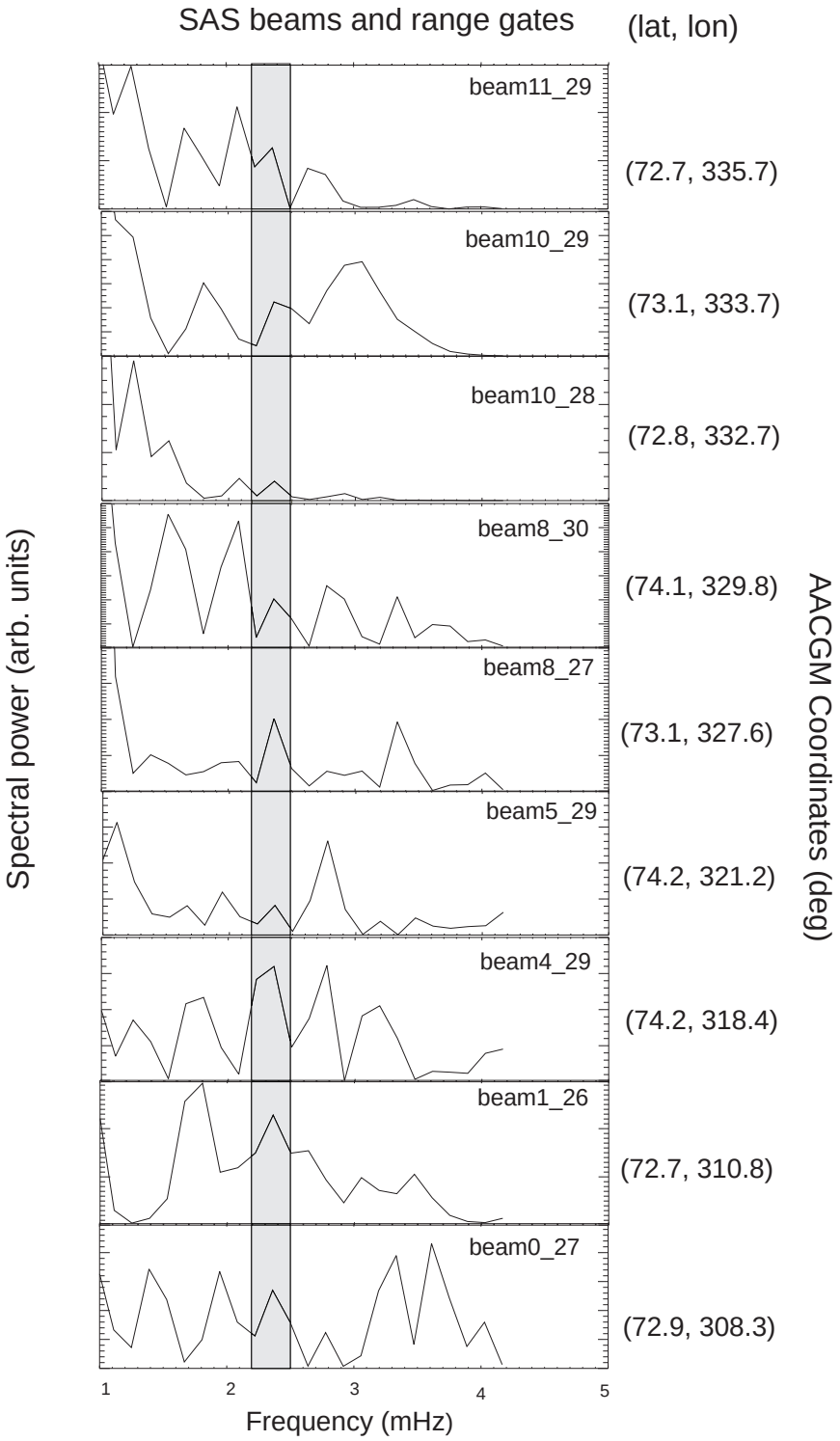

Figure 7.9: Spectral power observed in the indicated beams and range gates of the Saskatoon radar. The geomagnetic coordinates of the centre of each range gate on the right hand side. The shaded frequency range highlights the consistent peak in the 2.2-2.5 mHz band.

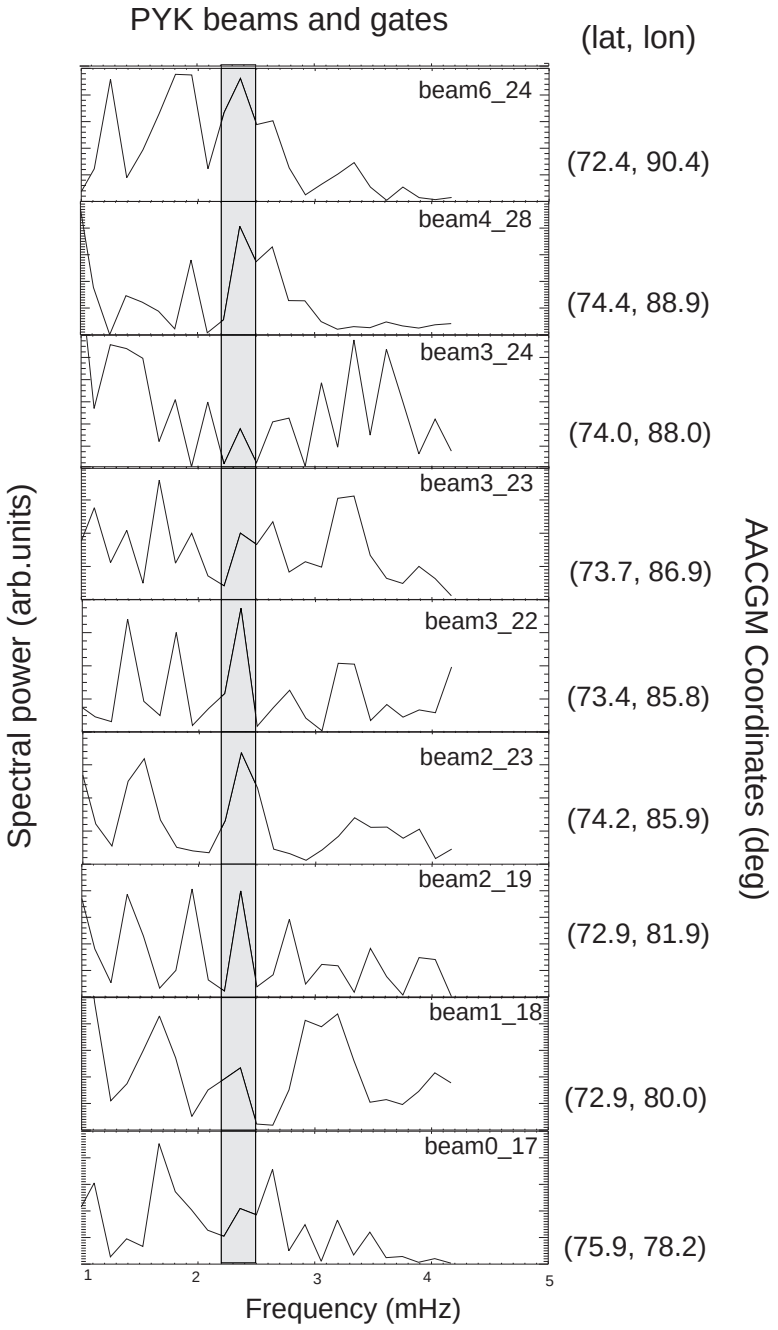

Figure 7.10: Spectral power observed in the indicated beams and range gates of the Pykkvibaer radar. The geomagnetic coordinates of the centre of each range gate on the right hand side. The shaded frequency range highlights the consistent peak in the 2.2-2.5 mHz band.

7.3 The Event of October 06, 2006 (16:00-18:00 UT)

7.3.1 Pulsation finder results

Pc5 pulsation event was observed between 16:00 to 18:00 UT on 06 October 2006. The investigation started by using an Automated Pulsation Finder program [36]. The Pulsation

Finder highlighted a significant peak in beam 9 and range gate 37 of the Goose Bay radar. The temporal resolution of the data used in the pulsation finder is 1 s. The results of the Pulsation Finder are shown in Figure 7.11 which shows the line-of-sight Doppler velocity recorded at the Goose Bay, filtered in the Pc5 band, and the corresponding power spectrum. The red line shows the level at which peaks in the spectrum are significant. The detector recorded a significant resonance in the frequency band 3.2-3.5 mHz in beam 9 in range 37.

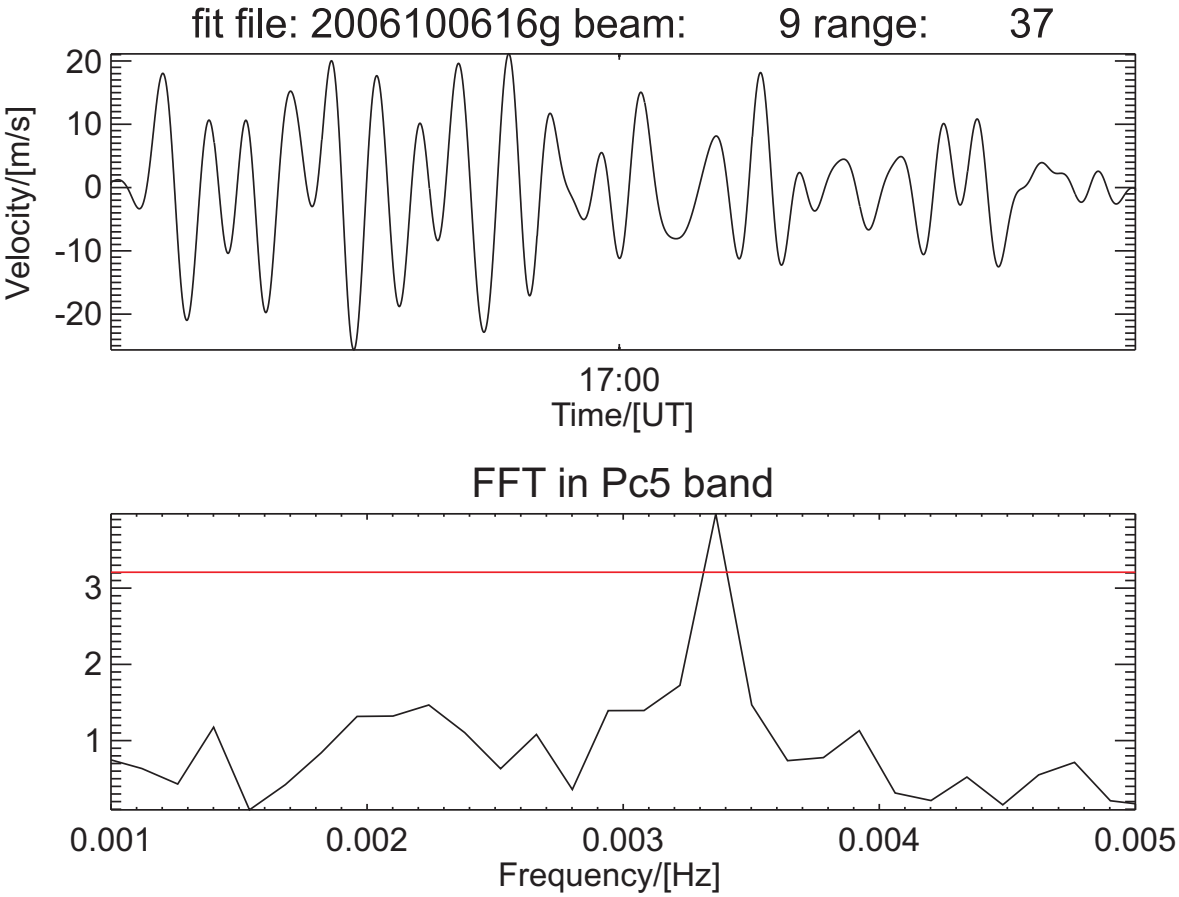

Figure 7.11: The top panel shows Pc5 band filtered data and the bottom shows the corresponding power spectrum and the significant limit level from filtered data. The peak detector recorded the peak in frequency band 3.2-3.5 mHz as significant.

7.3.2 Time range summary plot

The range-time summary plot of line-of-sight Doppler velocity of beam 9 of the Goose Bay radar is shown in Figure 7.13. The velocity is indicated by the colour bar on the right of the figure. Blue indicates velocities moving toward the radar, while red corresponds to the velocities moving away from the radar. The solid rectangle shows the location of pulsation activity in this beam. The ionospheric perturbations visible in the range-time plot as bands of alternating positive and negative (shades of blue and red) Doppler velocities are characteristic of Pc5 pulsations.

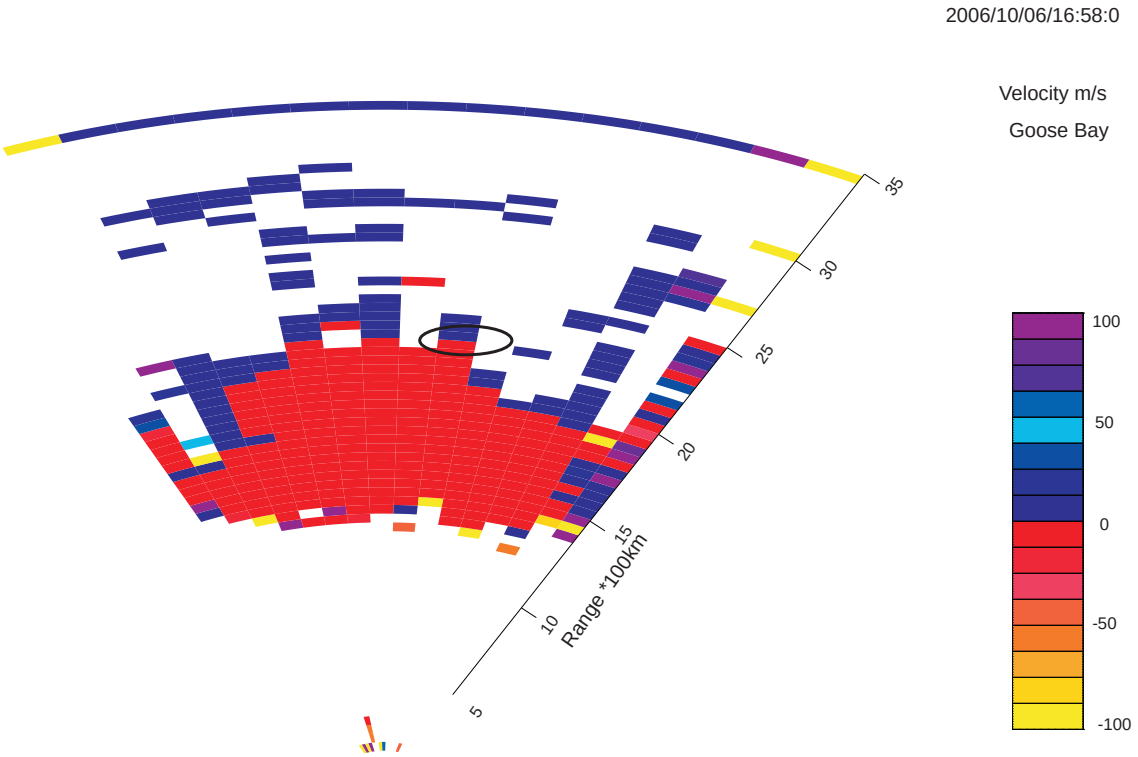

Figure 7.12: A beam-range of Dopper velocity in the field of view of Goose Bay, for the scan at 16:58 UT.

Figure 7.12 shows a full scan of the Goose Bay radar field of view (fov). The range gates are presented in kilometers (km). Doppler velocities are color coded. The beams are numbered from west to east in the field of view of the radar. The solid ellipse indicates the place where the Pc5 pulsation event was first highlighted.

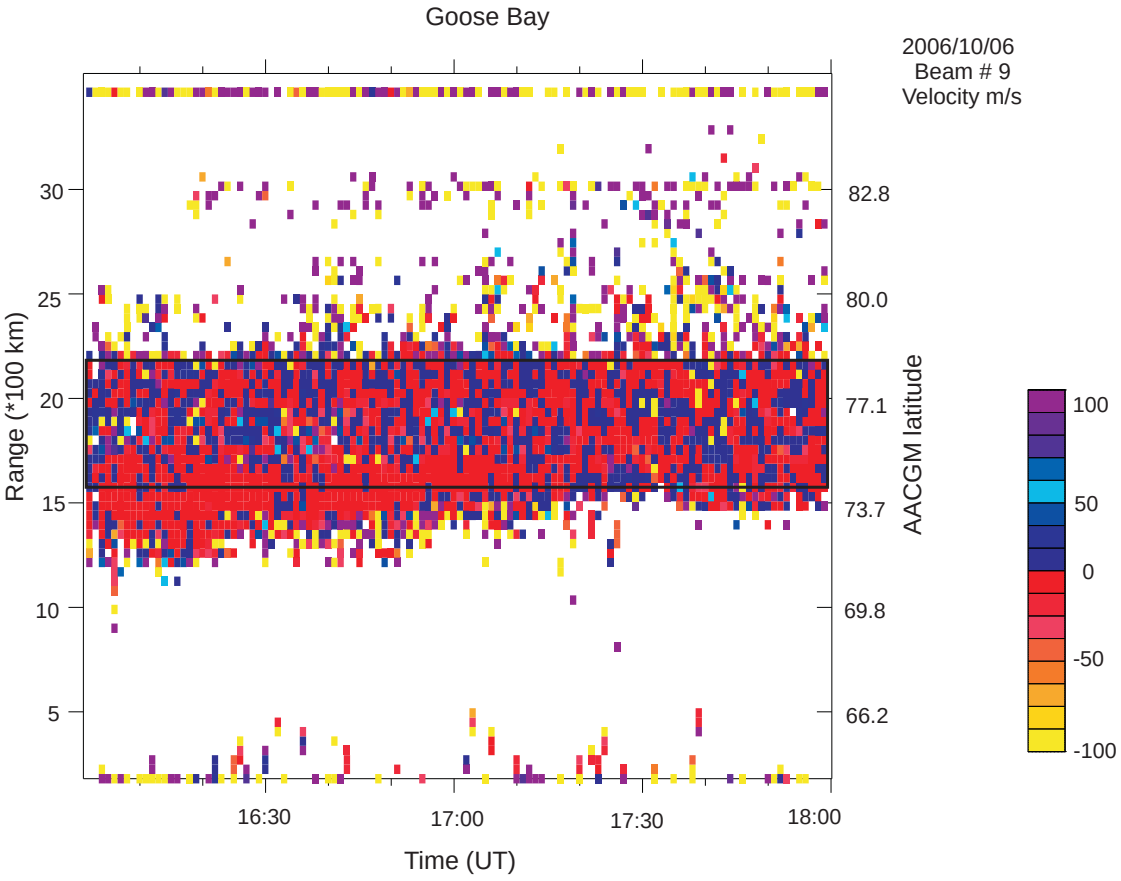

Figure 7.13: A time-range summary plot of Doppler velocity measured by beam 9 showing range and AACGM latitude.

7.3.3 Map of HF radars used

In Figure 7.14, we show a map of the locations of the three SuperDARN radars; Saskatoon, Goose Bay, and Pykkvibaer, and the magnetometer stations of the CARISMA, Greenland and IMAGE arrays. The magnetometer stations will be discussed in the next chapter. These radars have a good spatial resolution over a large range of magnetic latitude and longitude. Once we identified the Pc5 ULF pulsation event in one radar (Goose Bay), we then proceeded to analyse all the beams and range gates of the Saskatoon and Pykkvibaer radars which were located within the same range of magnetic latitudes (i.e. within the solid red lines).

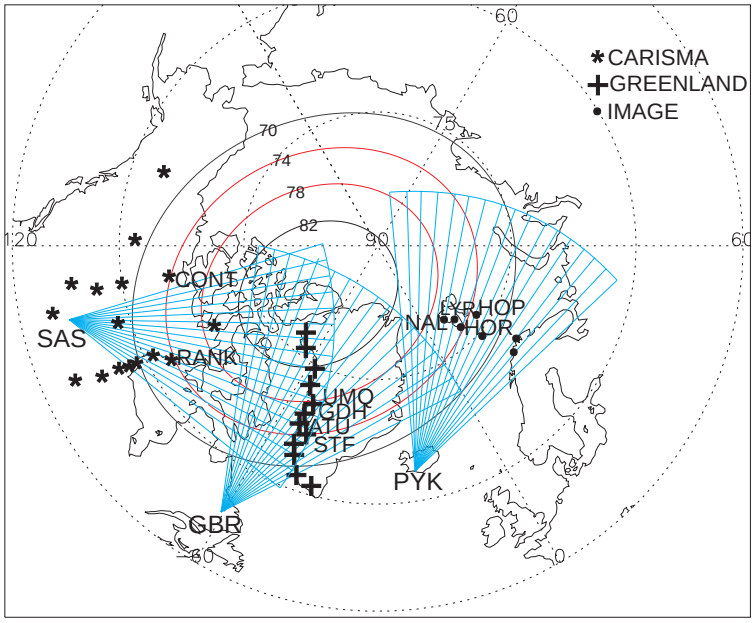

Figure 7.14: Fields of view of the SuperDARN radars at the Saskantoon (SAS), Goose Bay (GBR) and Pykkvibaer (PYK) plotted in geographic coordinates. The solid lines are AACGM magnetic latitude.

7.3.4 Time series and corresponding spectral power

The time series of Doppler velocities for different beams and range gates at the magnetic latitudes of interest of the Goose Bay, Saskatoon and Pykkvibaer radars are shown in Figures 7.15, 7.16 and 7.17. The time series were analysed to obtain power spectra that are similar to the one observed using APF as shown in Figure 7.11. The data used in these plots have a time resolution of 60 s.

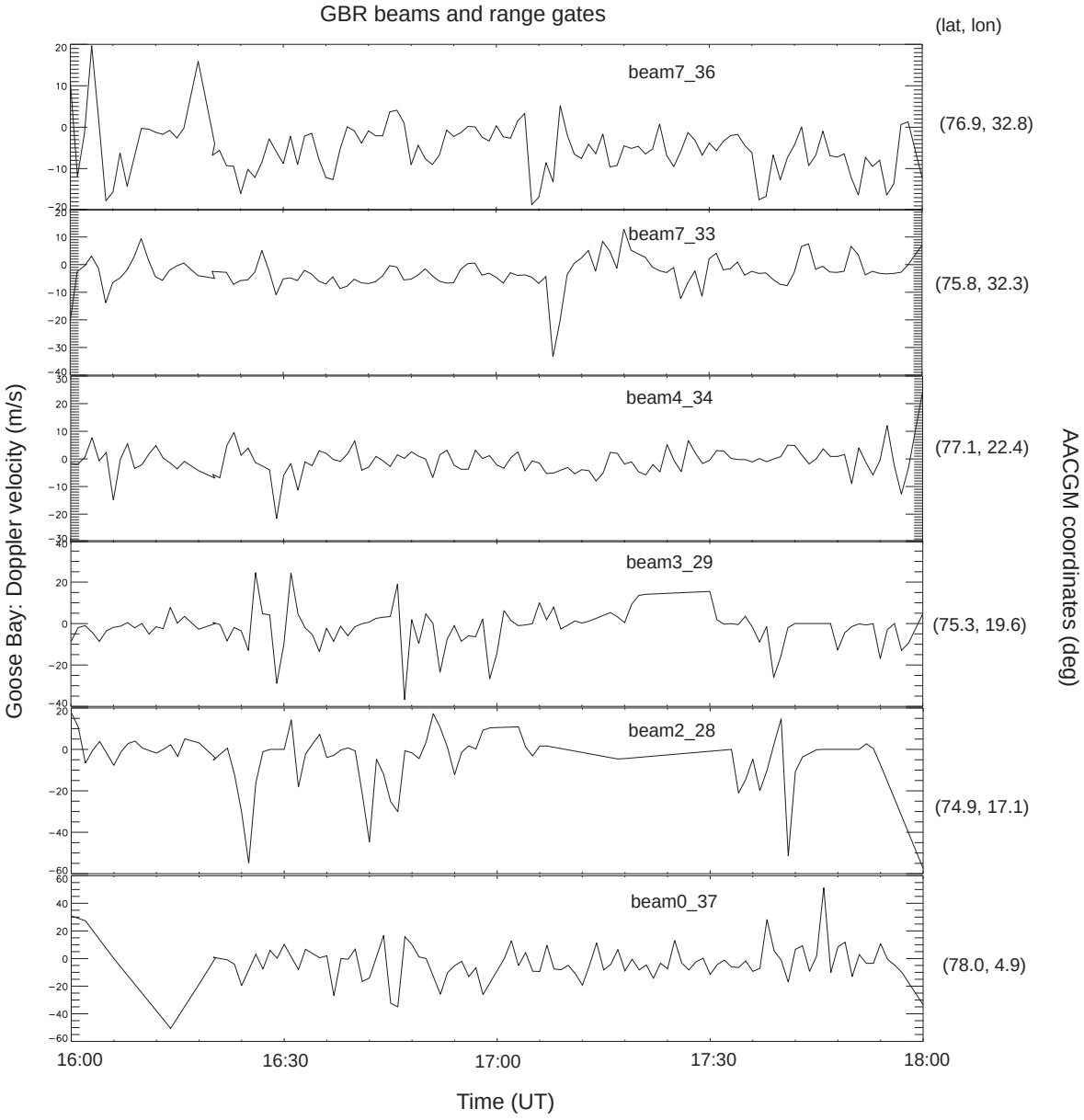

Figure 7.15: Doppler velocities, as functions of time, measured in the indicated beams and range gates of the Goose Bay radar.

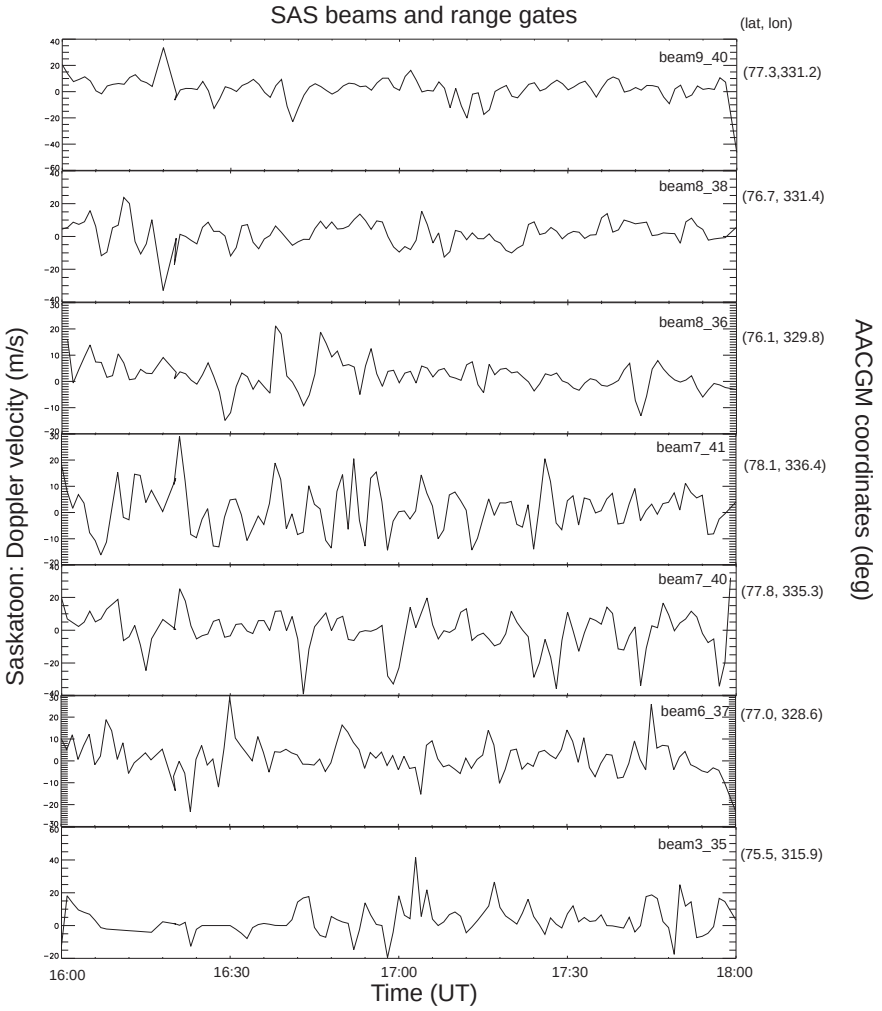

Figure 7.16: Doppler velocities, as functions of time, measured in the indicated beams and range gates of the Saskatoon radar.

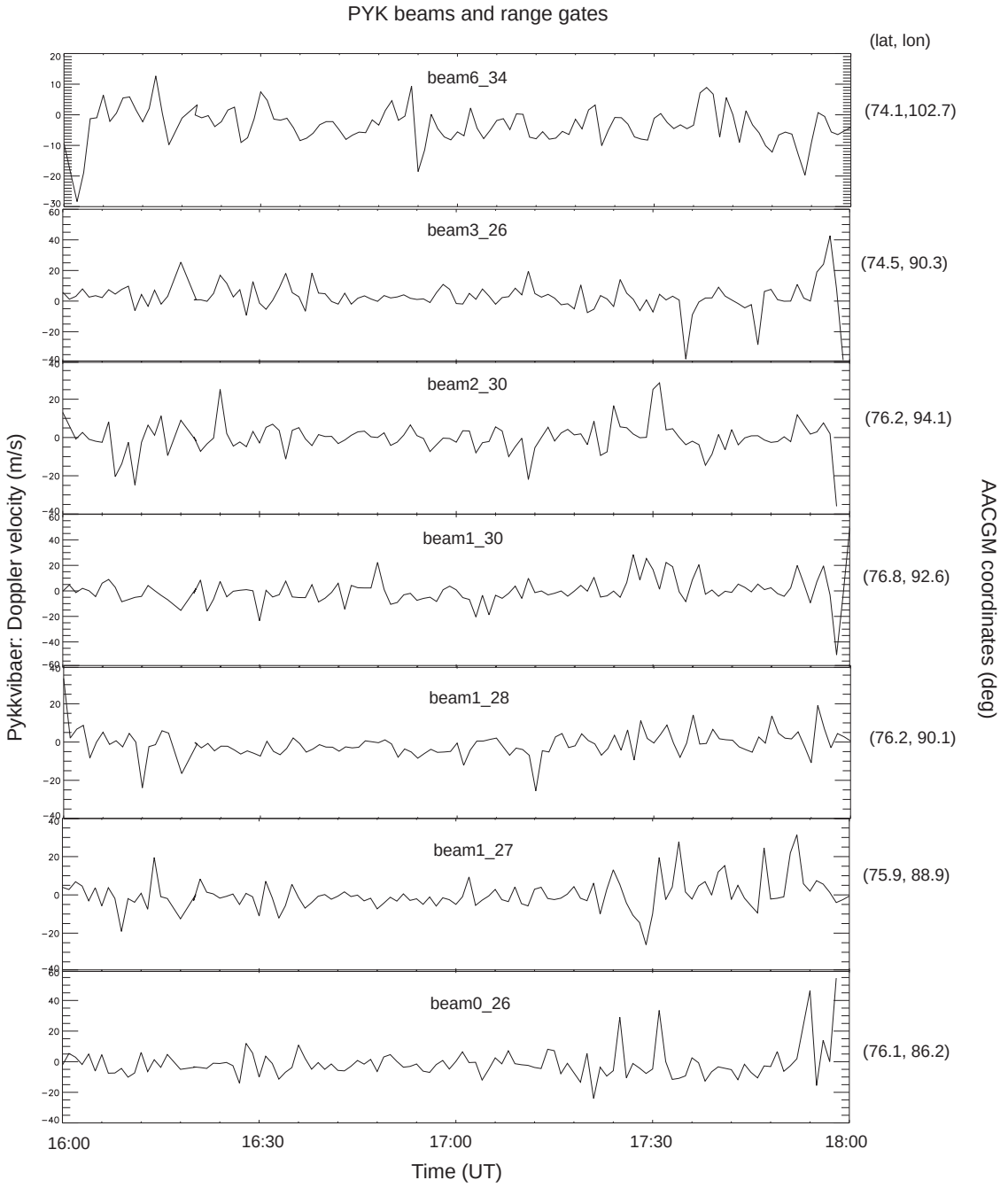

Figure 7.17: Doppler velocities, as functions of time, measured in the indicated beams and range gates of the Pykkvibaer radar.

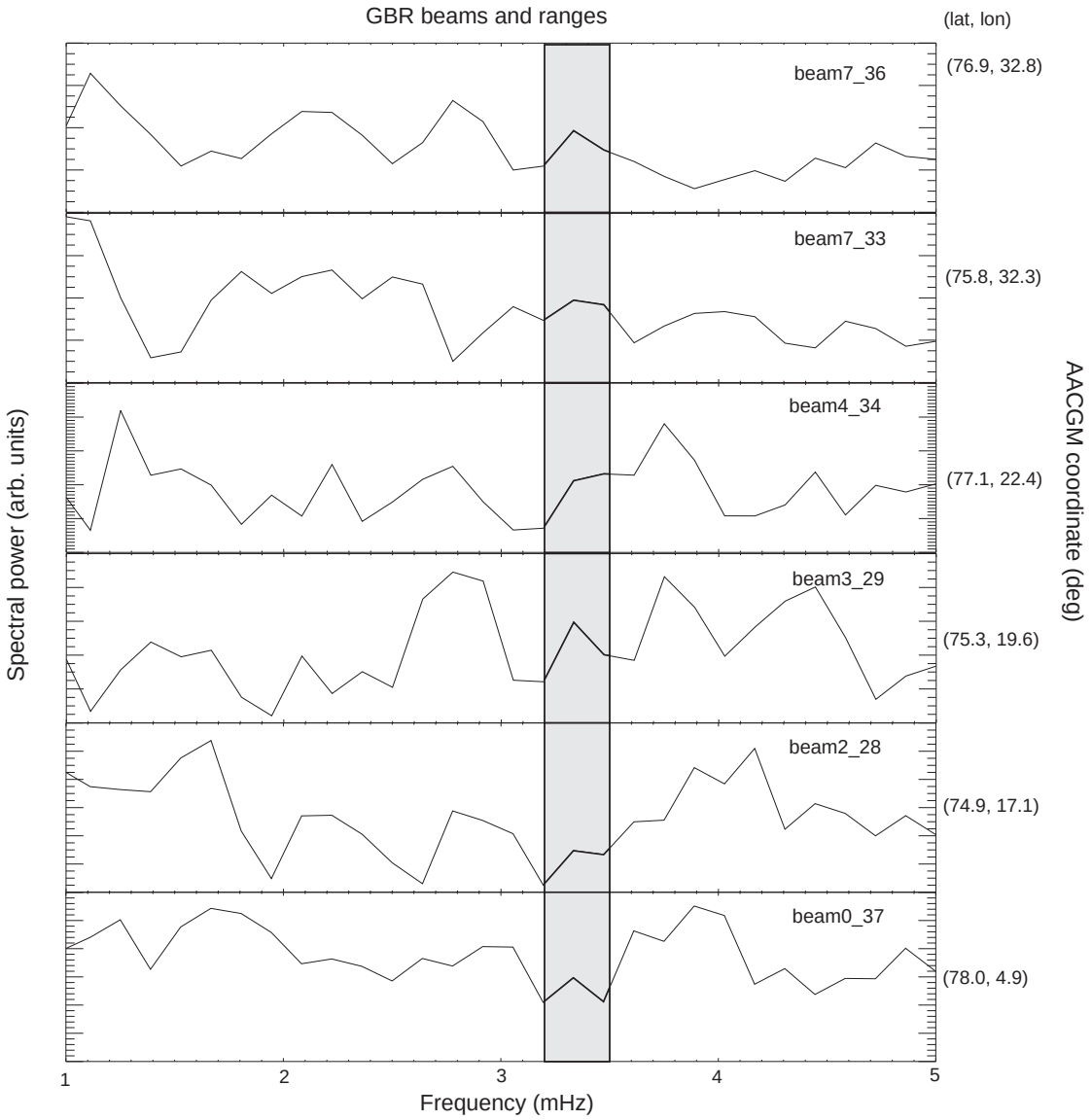

Figure 7.18: Spectral power observed in the indicated beams and range gates of the Goose Bay radar. The geomagnetic coordinates of the centre of each range gate on the right hand side. The shaded frequency range highlights the consistent peak in the 3.2-5.5 mHz band.

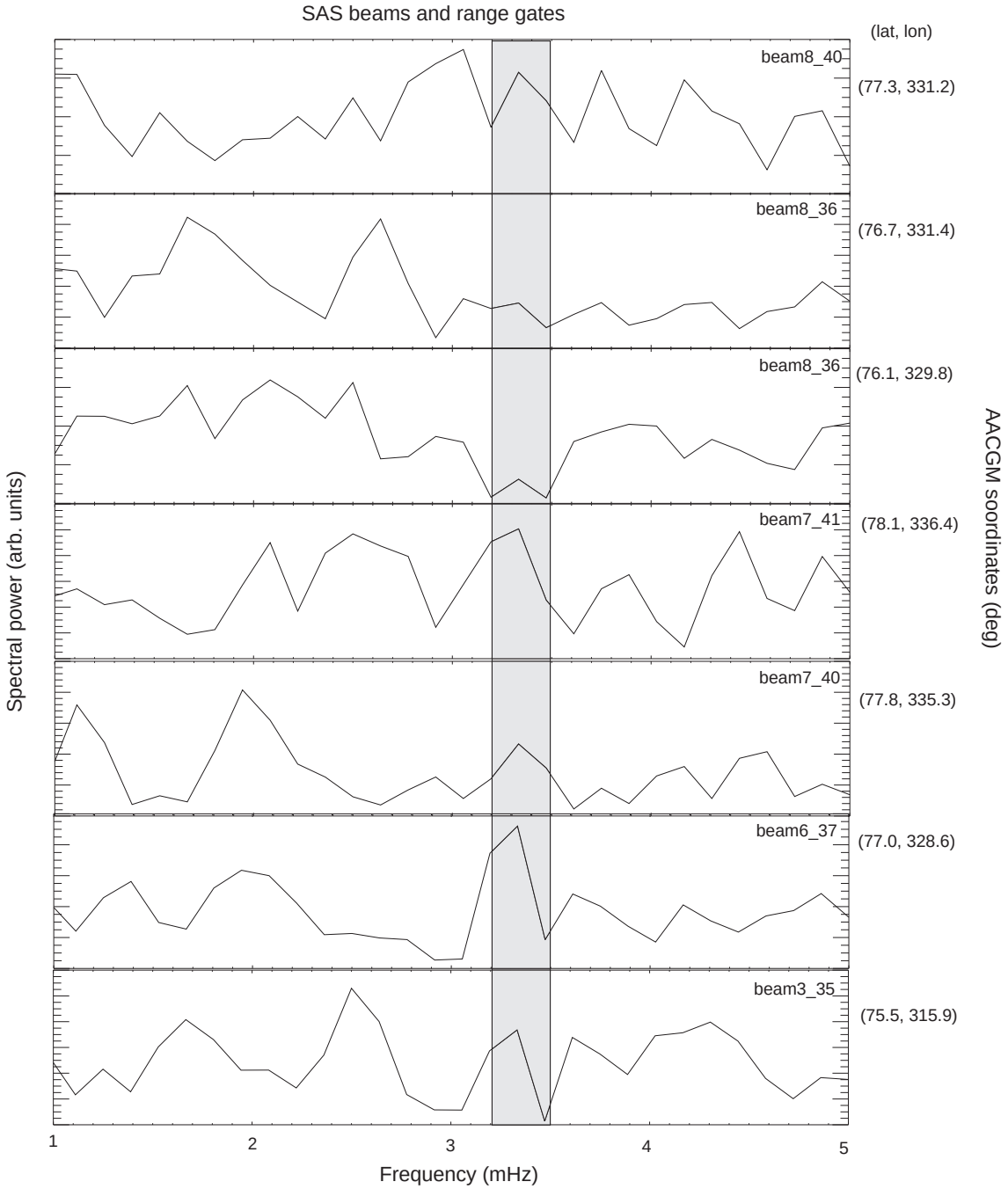

Figure 7.19: Spectral power observed in the indicated beams and range gates of the Saskatoon radar. The geomagnetic coordinates of the centre of each range gate on the right hand side. The shaded frequency range highlights the consistent peak in the 3.2-3.5 mHz band.

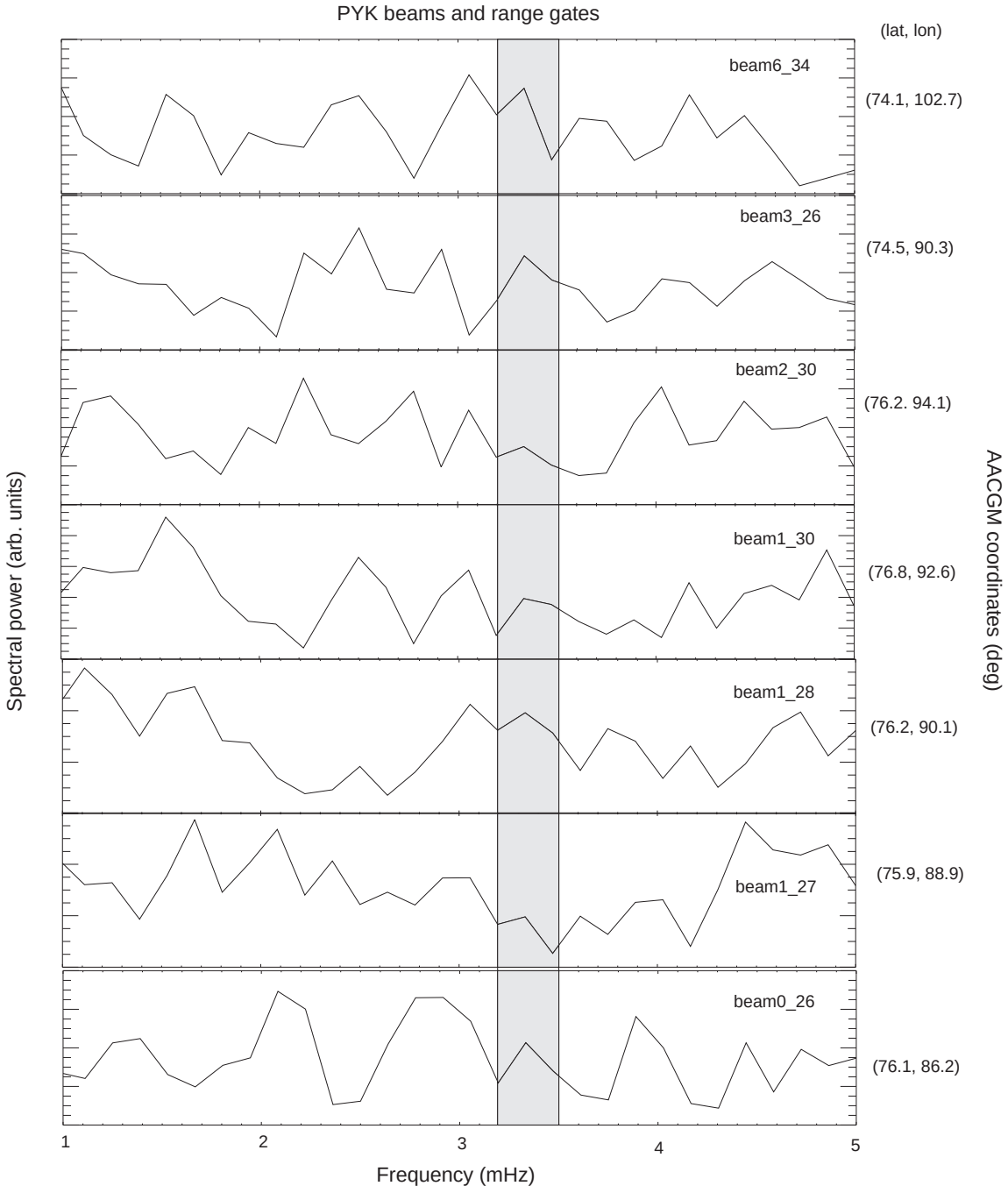

Figure 7.20: Spectral power observed in the indicated beams and range gates of the Pykkvibaer radar. The geomagnetic coordinates of the centre of each range gate on the right hand side. The shaded frequency range highlights the consistent peak in the 2.2-2.5 mHz band.

The investigation of the Pc5 pulsation event observed by Automated Pulsation Finder has been extended to other radars in the same magnetic latitudes. Velocity data from 16:00 to 18: 00 UT from these three radars were passed through a Fourier analysed to obtain the power spectra. The results from, Goose Bay (GBR), Saskatoon (SAS) and Pykkvibaer (PYK) radars are shown in Figures 7.18, 7.19 and 7.20. The shading highlights peaks in the 3.2-3.5 mHz range observed by Goose Bay, Saskatoon and Pykkvibaer radars in the

beams and range gates plotted in these Figures.

7.3.5 Latitude profile of the amplitude and phase of the resonance

Figure 7.21 shows latitude profile of amplitude and phase along beam 2 of Pykkvibaer. This plot is derived from range gate 27 to 31 data excluding 28 from beam 2. This is done using an analytic signal. The solid line represents the fitted curve, which shows the characteristics of field line resonances (FLRs). The region of resonance is clearly visible as a narrow peak in amplitude around 76.2 degree magnetic latitude with a standard phase change with increasing latitude, i.e., a decrease in phase as the resonance is crossed. In the case of the other radars we could not plot the latitude profile of amplitude and phase because there were not enough cell that were magnetic aligned or close to each other.

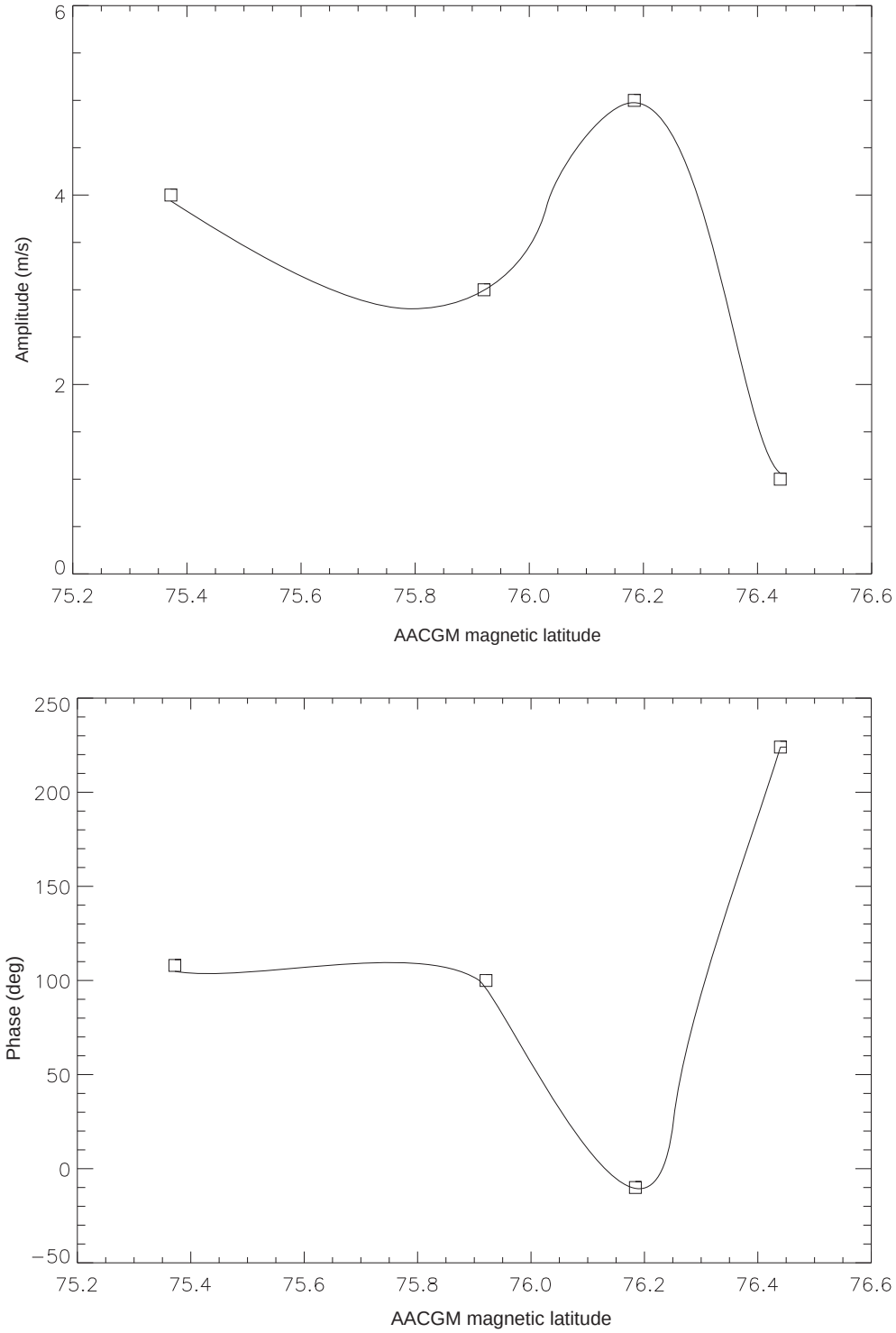

Figure 7.21: Latitude profile of amplitude and phase along beam 2 (beam most aligned with the magnetic meridian) of Pykkvibaer.

7.4 The Event of September 14, 2006 (18:00-20:00 UT)

7.4.1 Pulsation finder results

In this event, the final presented in this work. The Pulsation Finder highlighted a significant peak in beam 10 and range gate 51 of the Goose Bay, in beam 7 and range gate 47 in the Saskatoon (northern hemisphere polar region) and in beam 9 range gate 12 of Sanae (southern hemisphere polar region) radar. The temporal resolution of the data used in the pulsation finder is 1 s. The results of the Pulsation Finder are shown in Figures 7.22, 7.23 and 7.24, which show the line-of-sight Doppler velocity recorded at the Goose Bay, Saskatoon and Sanae filtered in the Pc5 band, and the corresponding power spectrum respectively.

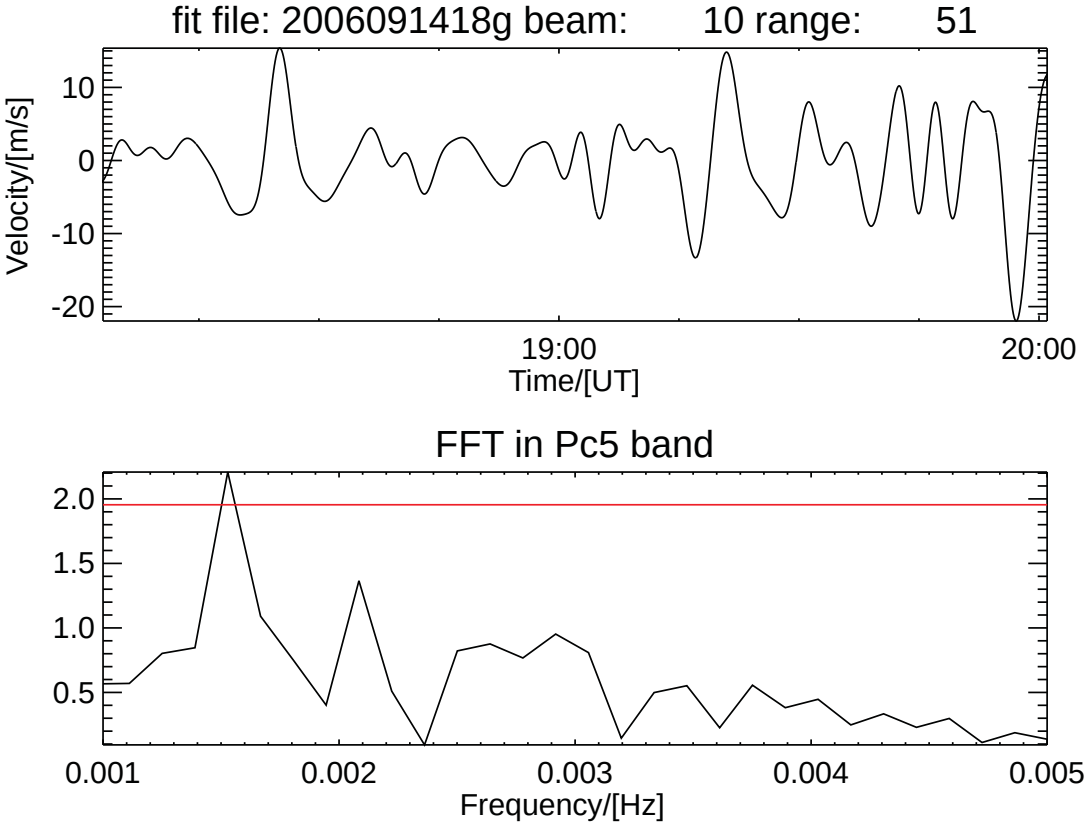

Figure 7.22: The top panel shows Pc5 band filtered data and the bottom shows the corresponding power spectrum and the significant limit level from filtered data. The peak detector recorded the peak in frequency band 1.4-1.7 mHz as significant.

This event is significant in that magnetically conjugate pulsations are detected.

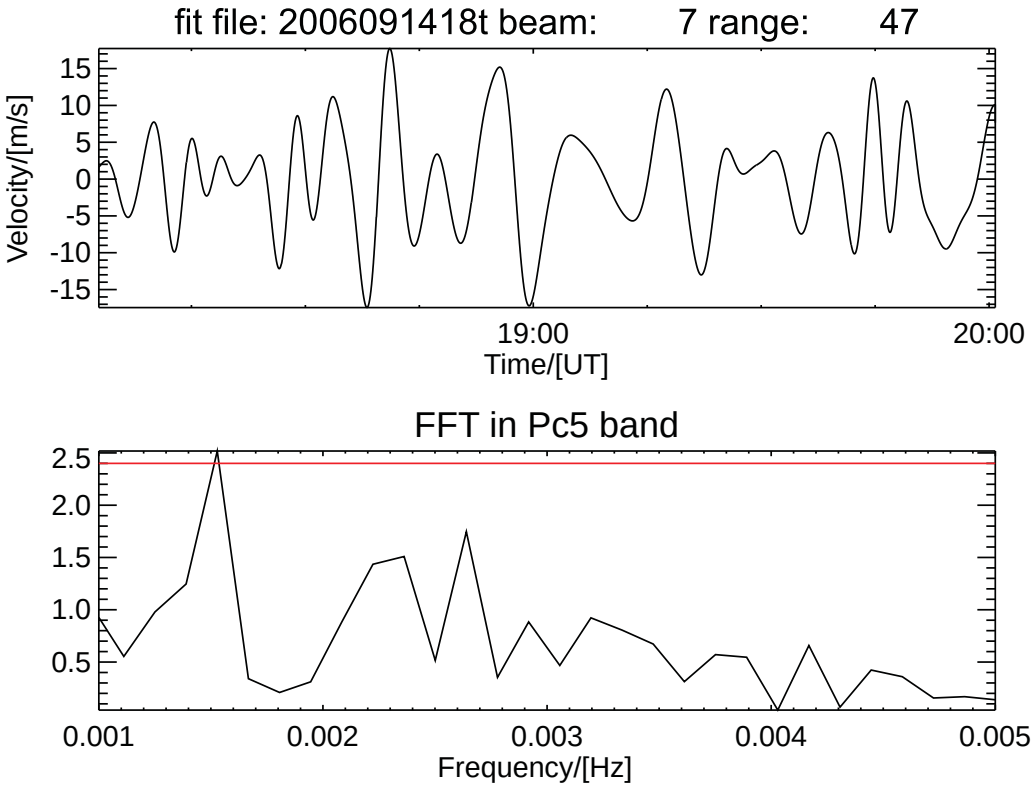

Figure 7.23: The top panel shows Pc5 band filtered data and the bottom shows the corresponding power spectrum and the significant limit level from filtered data. The peak detector recorded the peak in frequency band 1.4 -1.7 mHz as significant.

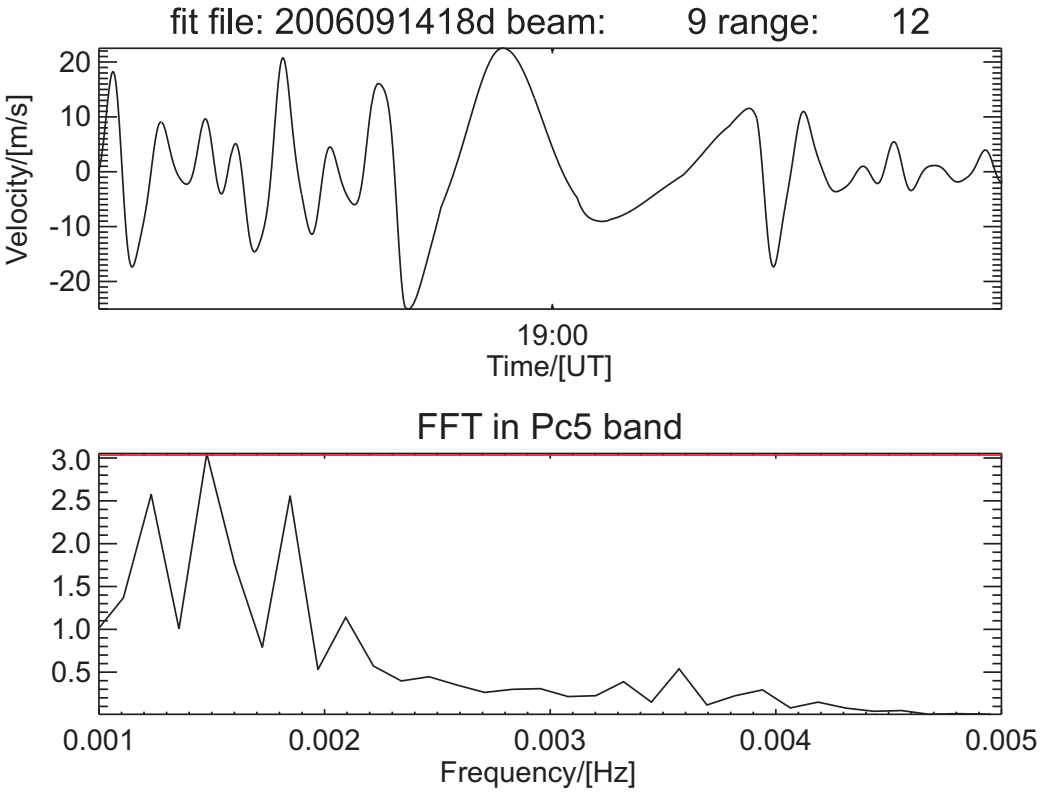

Figure 7.24: The top panel shows Pc5 band filtered data and the bottom shows the corresponding power spectrum and the significant limit level from filtered data. The peak detector recorded the peak in frequency band 1.4-1.7 mHz as significant.

The red line shows the level at which peaks in the spectrum are significant. The detector recorded a significant resonance in the frequency band 1.4-1.7 mHz in all the three mentioned radars.

7.4.2 Time range summary plot

The range-time summary plots of line-of-sight Doppler velocities for these beams are presented in Figures 7.25 (Goose Bay, beam 10) and 7.26 (Saskatoon, beam 7) in which the alternating bands of positive and negative velocities characteristic of pulsations are evident. In the southern hemisphere Sanae radar, we do not show time range summary plot because of poor data. The magnetic latitude of beam 9 for range gate 12 Sanae radar is equivalent to -66.5 degrees. Sanae is conjugate radar for Goose Bay and observed pulsations but these pulsations occurred at different magnetic latitude.

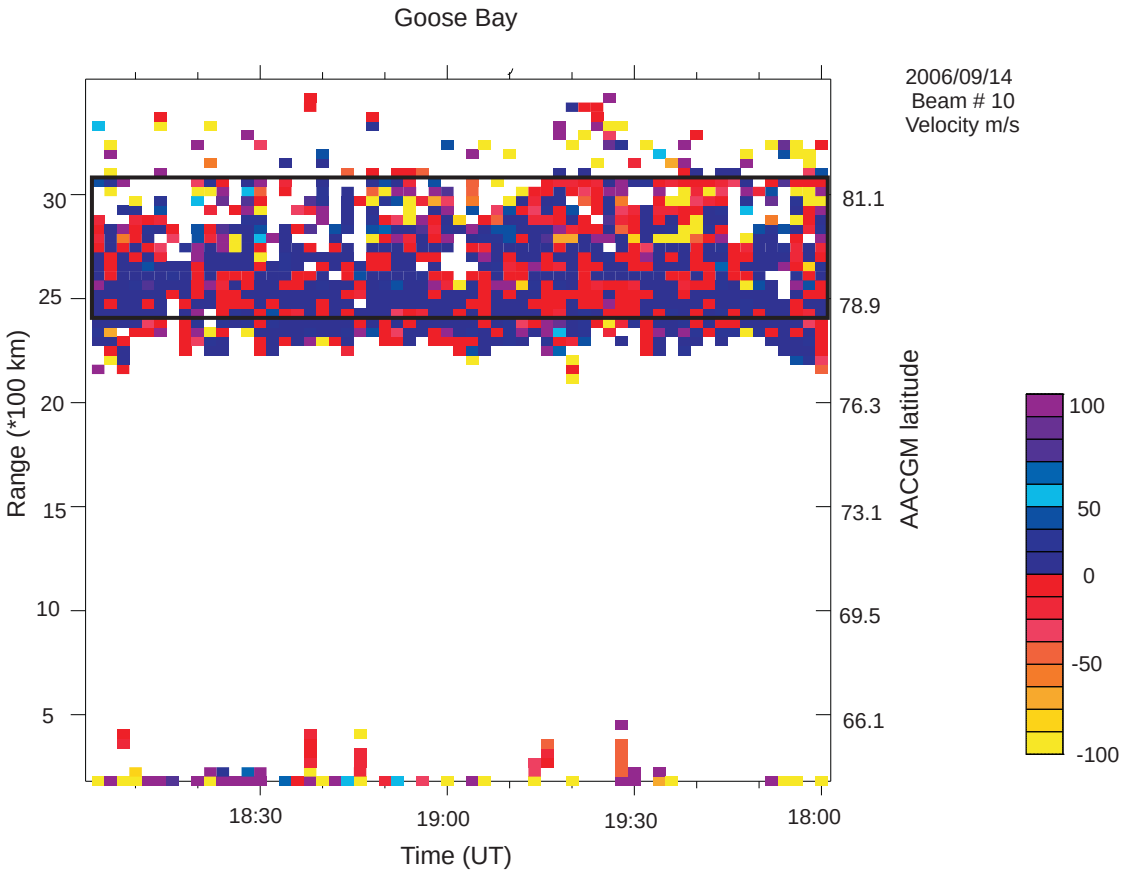

Figure 7.25: A time-range summary plot of Doppler velocity measured by beam 10 showing range and AACGM latitude.

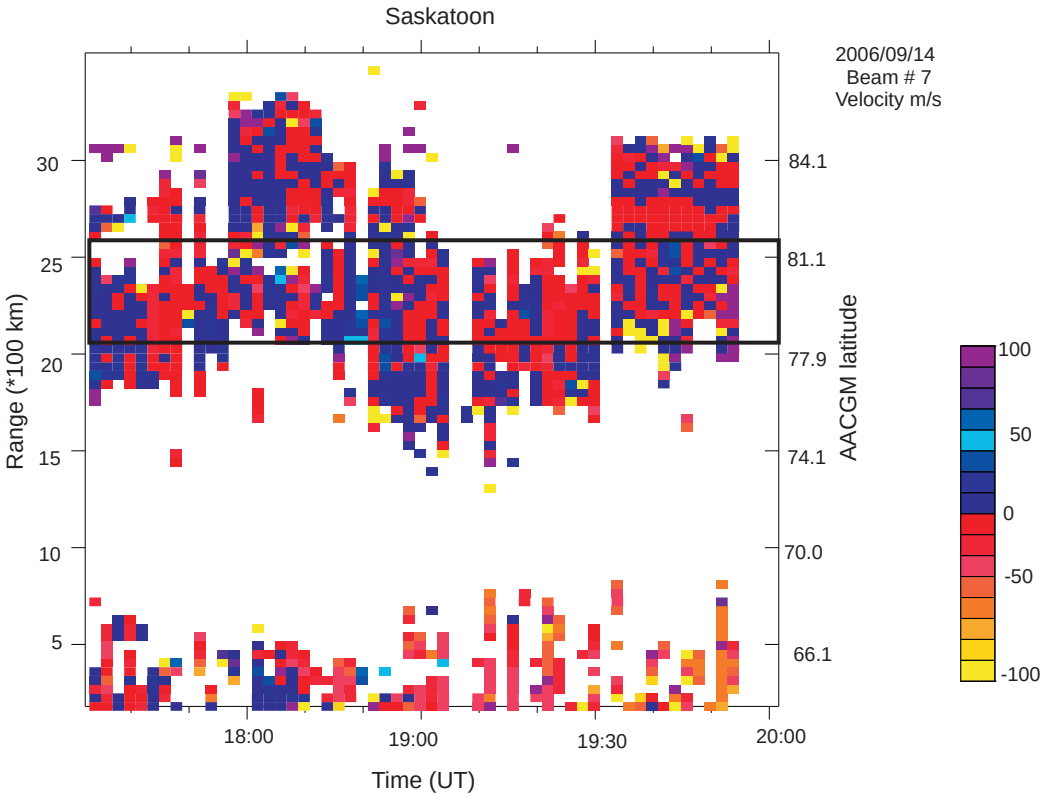

Figure 7.26: A time-range summary plot of Doppler velocity measured by beam 7 showing range and AACGM latitude.

7.4.3 Maps of HF radars used

Figures 7.27 and 7.28 show a geographic map outlining the field of the two SuperDARN radars; Goose Bay and Saskatoon in the northern polar region and Sanae in the southern polar region. These radars have a good spatial resolution over a large range of magnetic latitude and longitude. After identification of the Pc5 pulsation event in one radar (Goose Bay), we proceeded to analyse all beams and range gate of the Saskatoon radar which were located within the same range of magnetic latitudes (i.e. within the solid red lines of Figure 7.27). In the southern hemisphere we observed the similar Pc5 pulsation event at the conjugate radar (Sanae), but not at the same range of magnetic latitudes (see Figure 7.28 within the solid red lines).

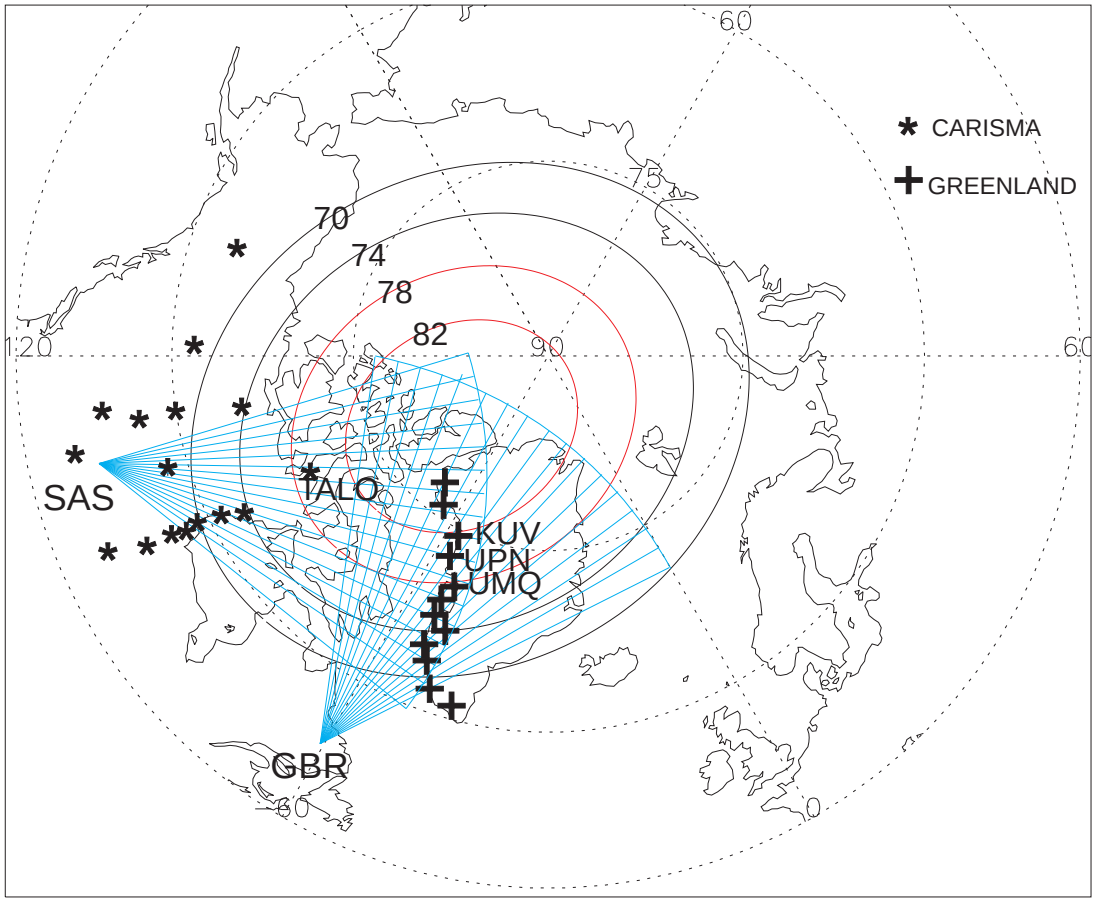

Figure 7.27: Fields of view of the SuperDARN radars at the Saskantoon (SAS) and Goose Bay (GBR) plotted in geographic coordinates. The solid lines are AACGM magnetic latitude.

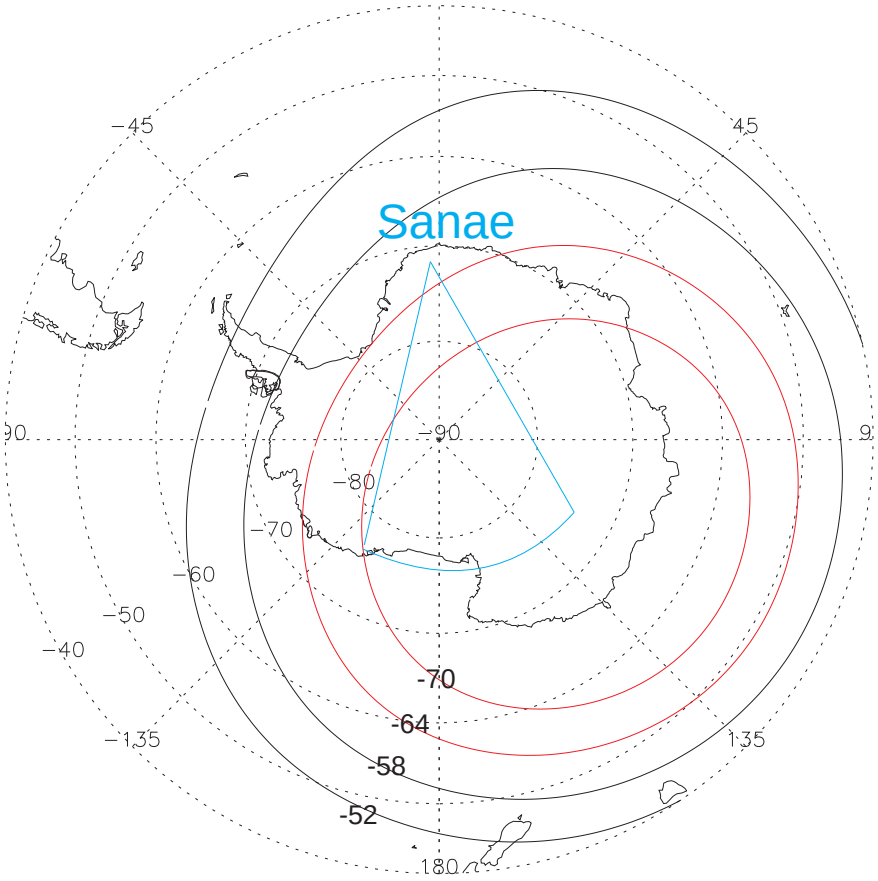

Figure 7.28: Fields of view of the SuperDARN radar at the Sanae (SAN) plotted in geographic coordinates. The solid lines are AACGM magnetic latitude.

7.4.4 Time series and their corresponding spectral peaks

The time series of the Doppler velocities are shown in Figures 7.29 and 7.30, were analysed to obtain power spectra that are similar to the ones observed using APF as shown in Figures 7.22, 7.23 and7.24. Figures 7.31 and 7.32 show spectral peaks for different beams and range gates at the magnetic latitudes of interest of the Goose Bay and Saskatoon radar. The data used in these plots have a time resolution of 120 s. This puts an upper frequency limit of 4.17 mHz on the pulsation that can be observed.

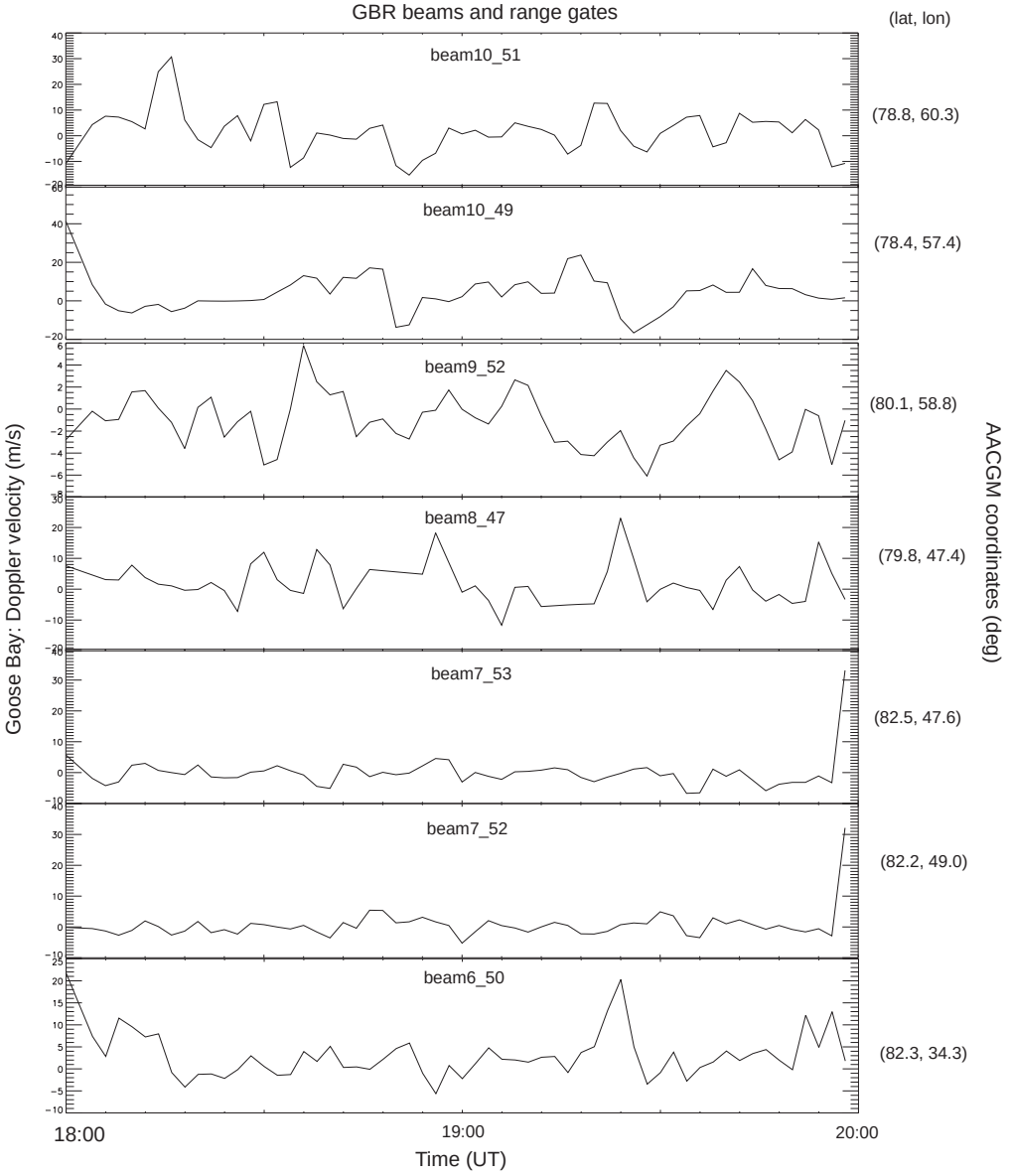

Figure 7.29: Doppler velocities, as functions of time, measured in the indicated beams and range gates of the Goose Bay radar.

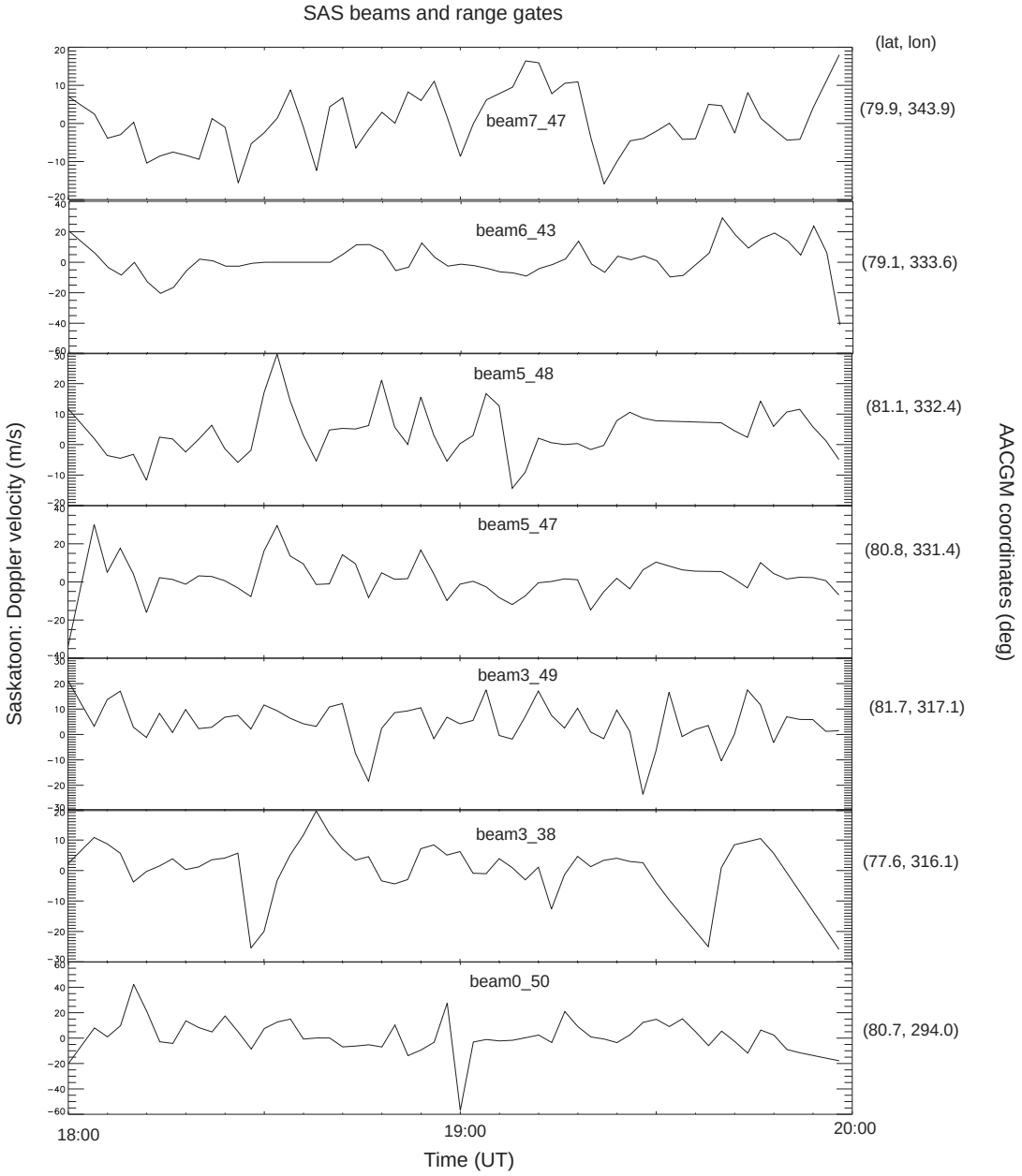

Figure 7.30: Doppler velocities, as functions of time, measured in the indicated beams and range gates of the Saskatoon radar.

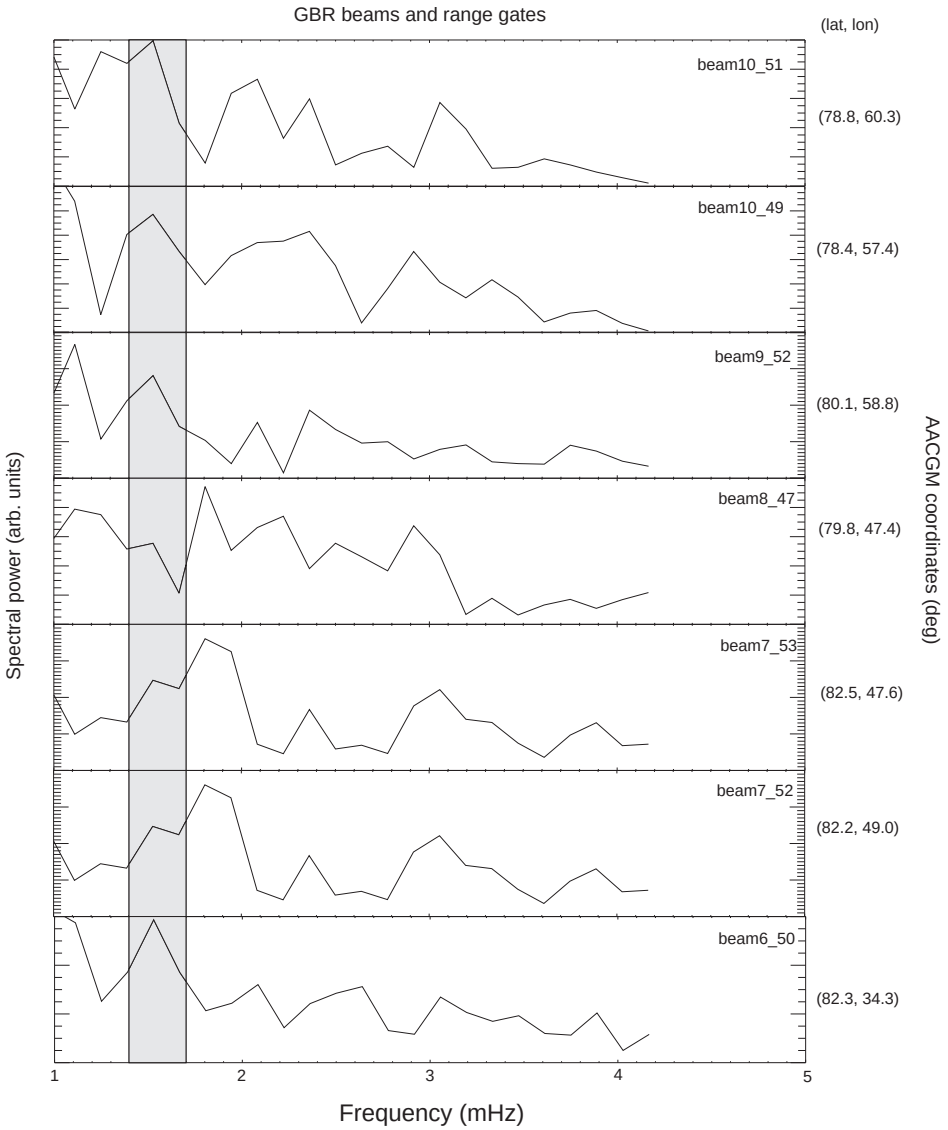

Figure 7.31: Spectral power observed in the indicated beams and range gates of the Goose Bay radar. The geomagnetic coordinates of the centre of each range gate on the right hand side. The shaded frequency range highlights the consistent peak in the 1.4-1.7 mHz band.

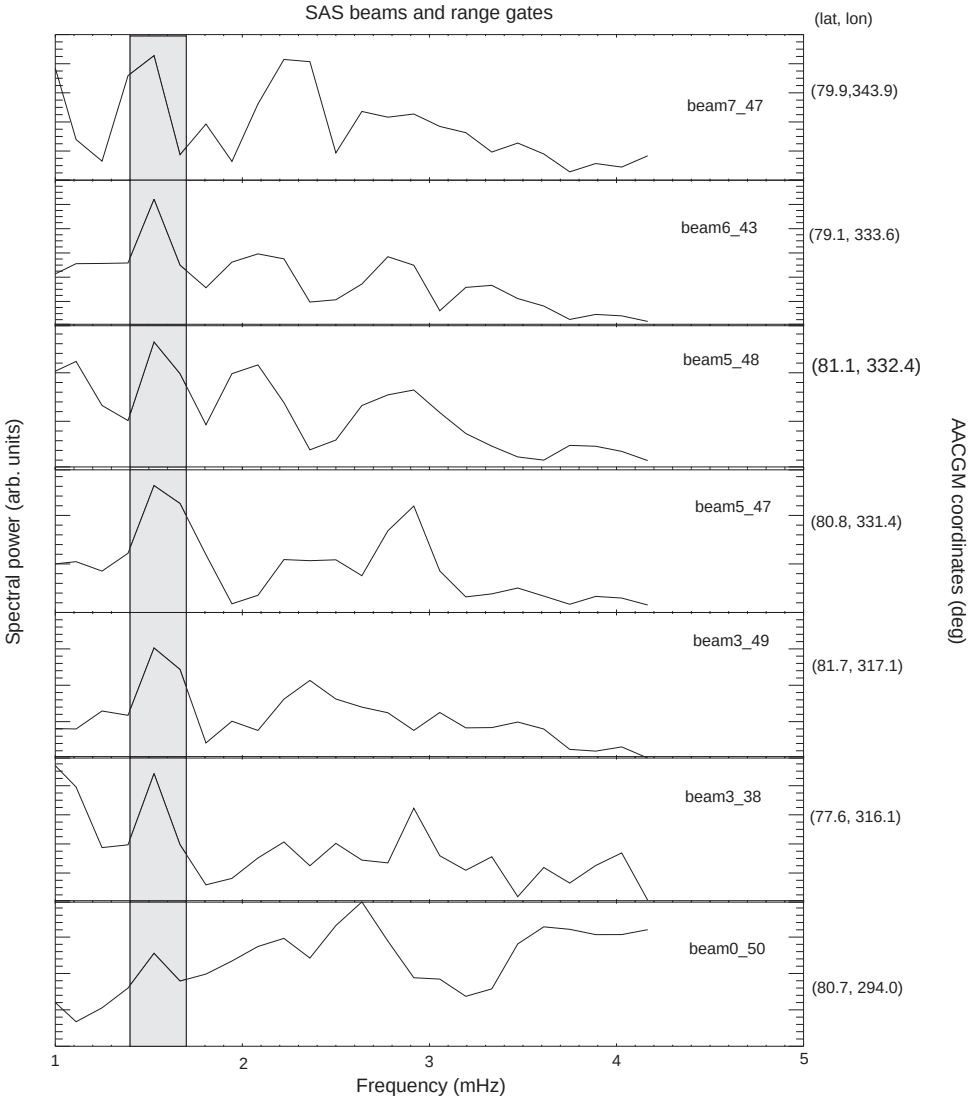

Figure 7.32: Spectral power observed in the indicated beams and range gates of the Saskatoon radar. The geomagnetic coordinates of the centre of each range gate on the right hand side. The shaded frequency range highlights the consistent peak in the 1.4-1.7 mHz band.

7.5 Multitaper spectral analysis

Multitaper spectral estimates arise from the inverse theory solution of the integral equation relating the FT of the available data to that of the ideal sample. Multiple windowing of data with orthogonal discrete prolate spheriodal sequences (DPSS). They are eigenfunctions of the kernel of the integral equation. A reasonable choice of W (should be less than half the width of the peaks of interest) must be made in order to take into account trade-off between leakage and variance. The number of tapers with potentially good bais properties determined by K=2NW t-1. The eigenspectrum from each taper is approximately distributed as chi-square random variable with 2° of freedom. This allows for determination of confidence levels against a null hypothesis of a noisy spectrum (see

Percival equation 258[44]).

This multi taper approach was applied to the Goose Bay radar velocity data for 20:00-22:00 UT on the 6th October 2006 that demonstrated peaks of interest (Figure 7.8 of thesis). The resulting spectral estimates (see Figures included below) show that all the peaks used in subsquent complex demodulation analysis are above the 99% confidence interval. Since peaks from other radars and in other events show similar power characteristics, we feel confident that comparable results would also be achieved in those instances.

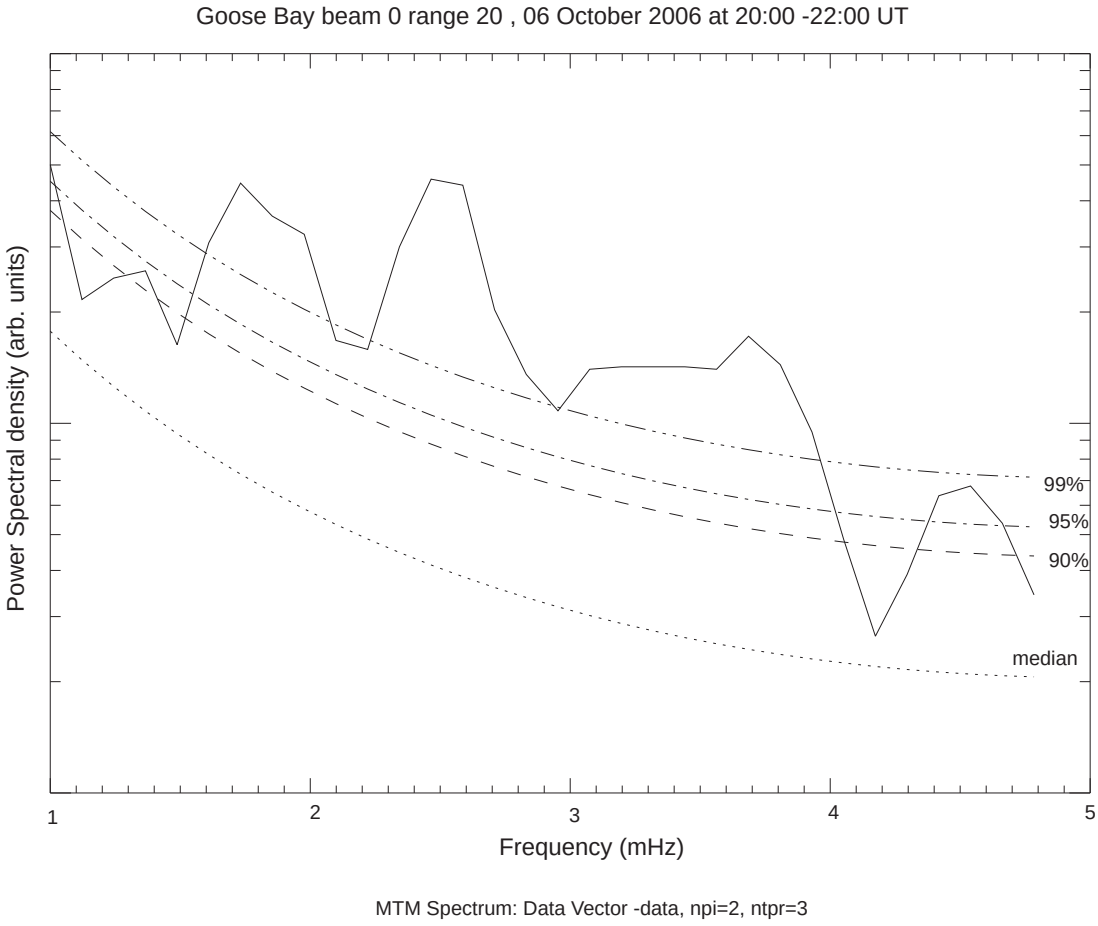

Figure 7.33: Multitaper spectrum observed in the indicated beam 0 and range gate 20 of the Goose Bay radar. The frequency range of interest (2.2-2.5 mHz) band.

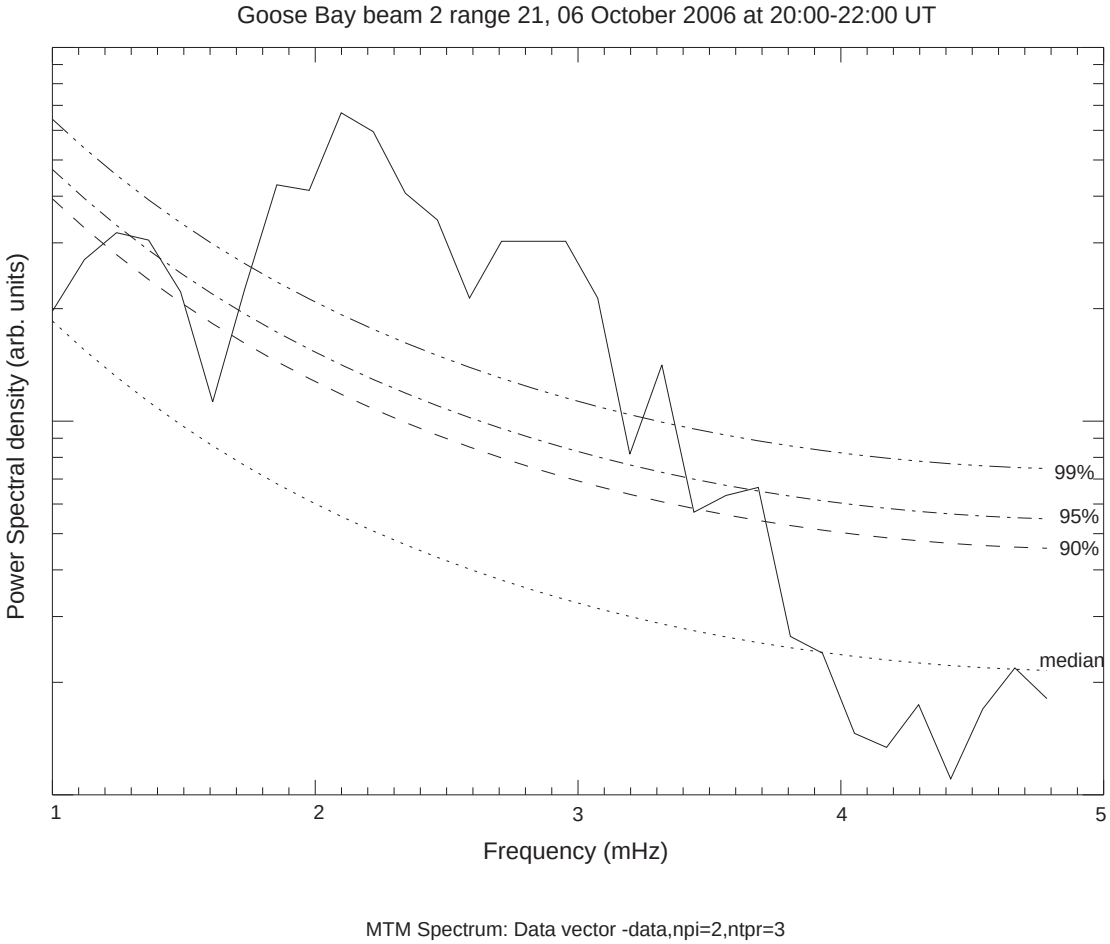

Figure 7.34: Multitaper spectrum observed in the indicated beam 2 and range gate 21 of the Goose Bay radar. The frequency range of interest (2.2-2.5 mHz) band.

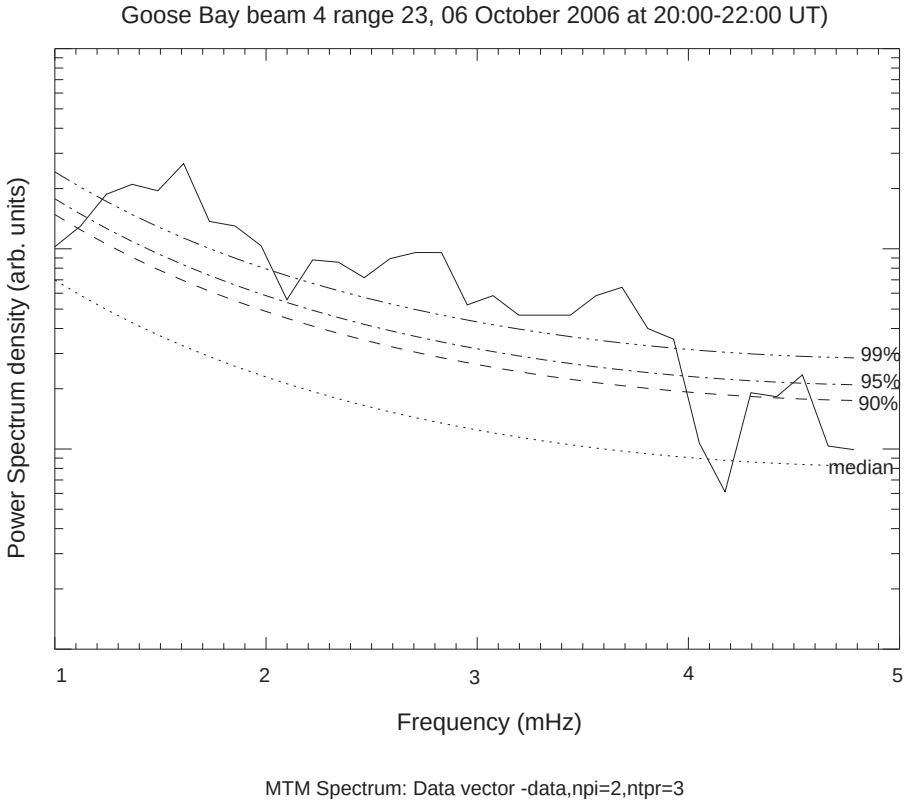

Figure 7.35: Multitaper spectrum observed in the indicated beam 4 and range gate 23 of the Goose Bay radar. The frequency range of interest (2.2-2.5 mHz) band.

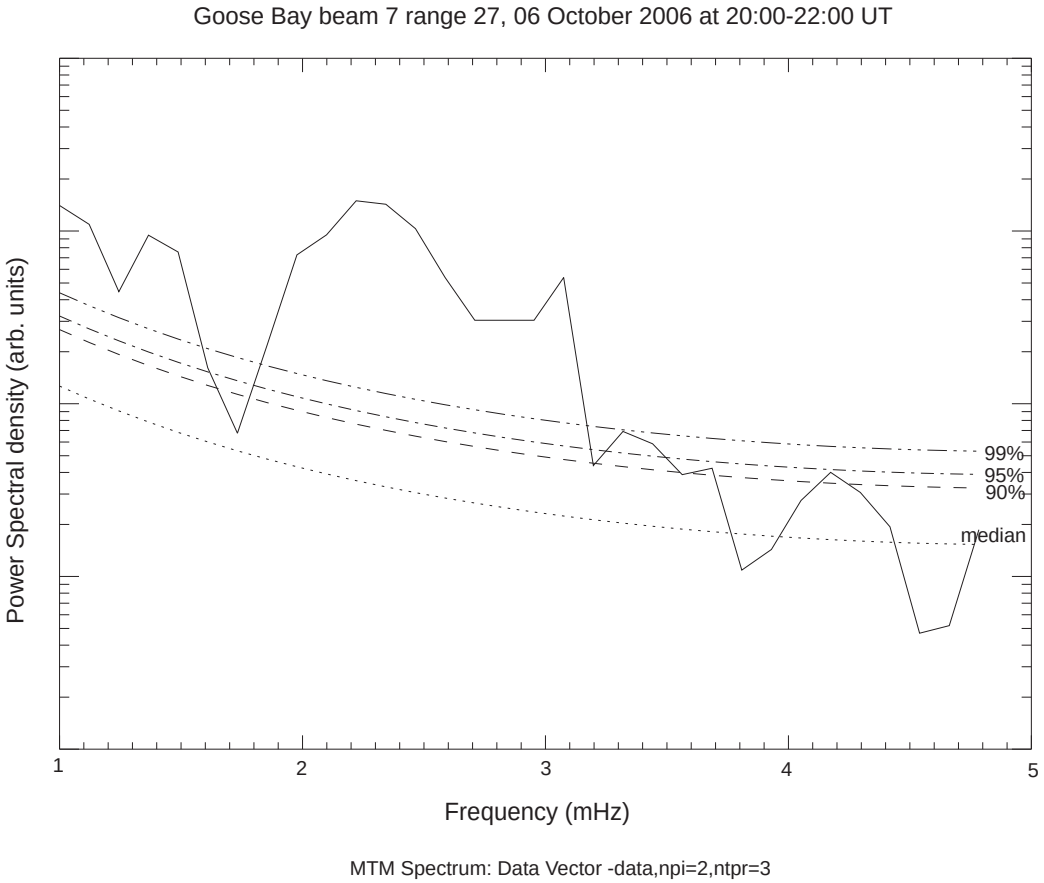

Figure 7.36: Multitaper spectrum observed in the indicated beam 7 and range gate 27 of the Goose Bay radar. The frequency range of interest (2.2-2.5 mHz) band.

7.6 Summary

An automated pulsation finder algorithm was created to search the SuperDARN FIT velocity data to identify pulsation events. The FFT approach was used to calculate the spectra of the data. The Pc5 pulsation events investigated here in the frequency bands 2.2-2.5 mHz, 3.2-3.5 mHz and 1.4-1.7 mHz were highlighted using Automated Pulsation Finder and confirmed by other radars in different beams and range gates. The range-time summary plots have shown the characterictics of pulsations on these events. The latitude profile of amplitude and phase along the mentioned beams have shown characterictics of field line resonances (FLRs). Analysis of the Goose and Pykkvibaer radars beam most aligned with the magnetic meridian demonstrates an amplitude peak over a narrow latitude range and associated phase change across the resonance (see Figure 7.4 and 7.21). The third event could not be determined if it is a field line resonance because the data quality was not good enough. Field line resonances tend to have a lower azimuthal wave number (m) values and thus often have external sources. Azimuthal wave number m values are determined for the pulsation events in Chapter 9.

Chapter 8

Magnetometer observations

8.1 Introduction

Ground-based magnetometer is one of the important instruments used to confirm the Pc5 pulsation events observed using the Automated Pulsation Finder in this study. In this study we carried out a detailed search of the observed Pc5 pulsations using CARISMA, Greenland and IMAGE arrays as mentioned in Chapter 6. The analysis and discussion of the data will focus on the period from 20:00 to 22:00 UT and 16:00-18:00 UT on 06 October 2006 respectively, and from 18:00 to 20:00 UT on 14 September 2006.

8.2 Time series and corresponding spectra

Magnetometer stations that lie within the red lines of latitude shown in Figures 7.5, 7.14 and 7.27 were chosen to be analysed in more detail.

8.2.1 The Event of October 06, 2006 (20:00-22:00 UT)

In this event, the following magnetometer stations are located within or near the field of view of one of these radars: Contwoyto (CONT) - Saskatoon; Sukkertonppen/Maniitsok (SKT) and Nuuk/Godthaab (GHB) - Goose Bay; Hornsund (HOR) - Pykkvibaer. The CONT station is in the same magnetic latitude range as other stations but not in the field of view of the mentioned radars. Figure 8.1 shows the time series plots for the stations. The time series data from 20:00 to 22:00 UT were Fourier analysed to obtain the power spectra. Other magnetometer stations within the field of view have no data while others do not have a significant peak in the 2.2-2.5 mHz band. Those magnetometer stations are not included in this study. The shading highlights peaks in the 2.2-2.5 mHz frequency band, which confirms the Pc5 pulsation event observed by these SuperDARN radars as shown in Figure 8.2. The event observed using the Automated Pulsation Finder appears in other radars and magnetometer chains.

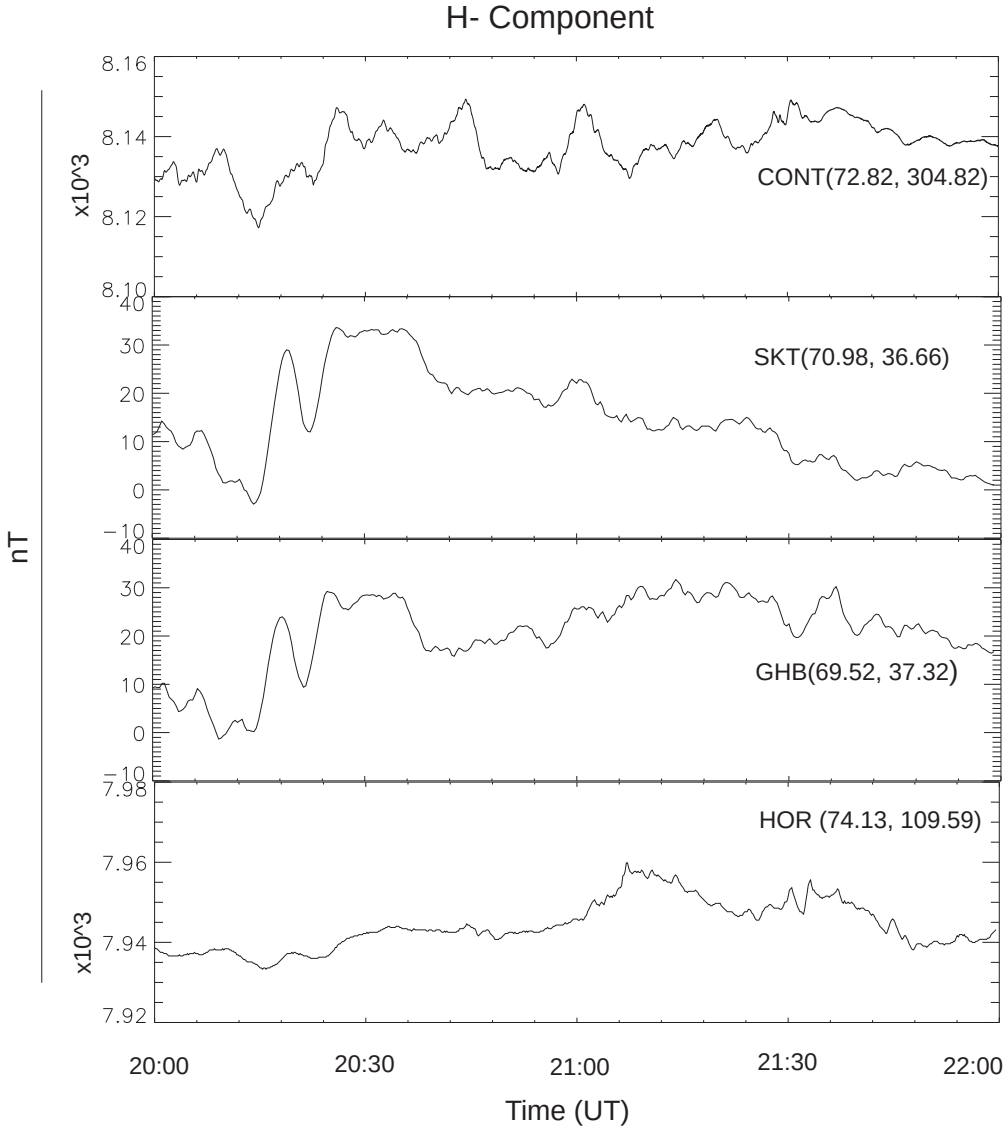

Figure 8.1: Time series observed from CONT (CARISMA), SKT and GHB (Greenland) and HOR (IMAGE).

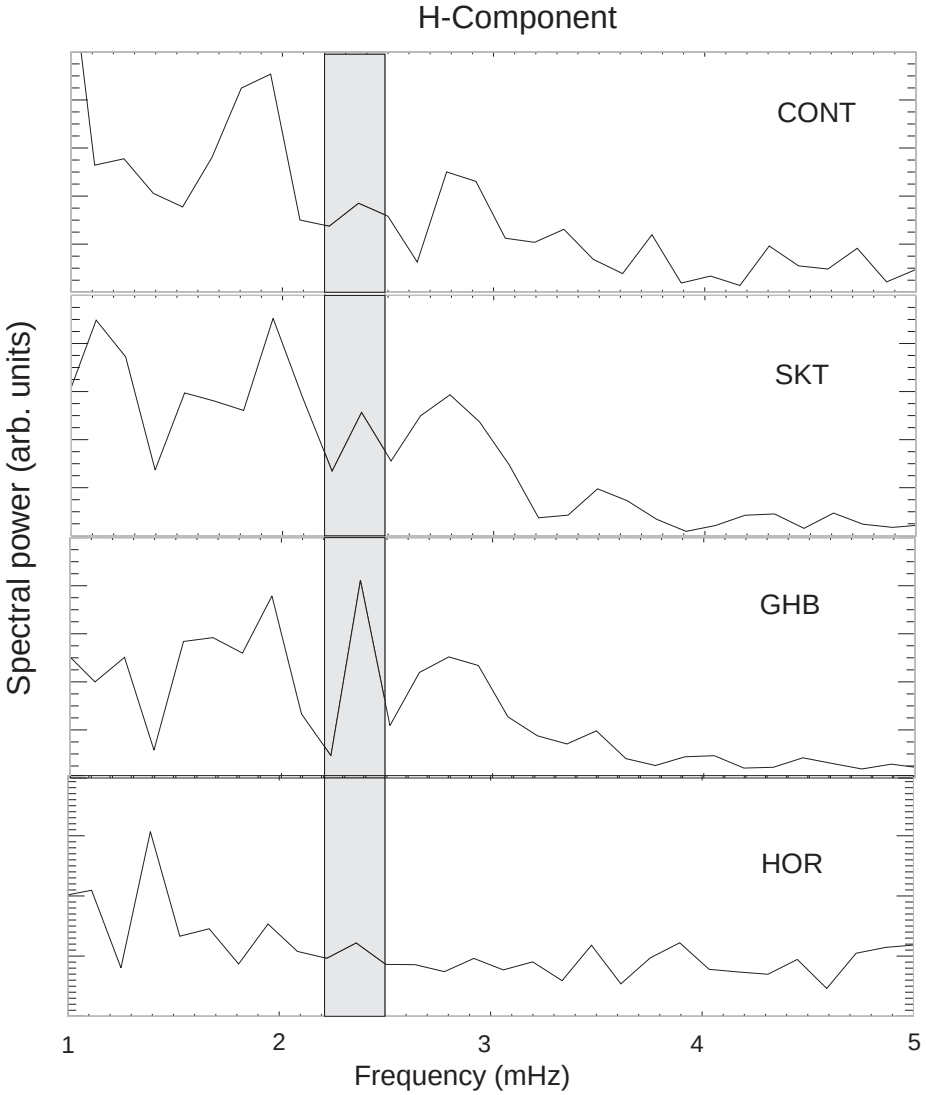

Figure 8.2: The spectral power for the magnetometer stations (CONT, SKT, GHB and HOR). They are plotted so that top to bottom is west to east.

The geographic and geomagnetic coordinates of the pertinent magnetometer stations are given in Table 8.1. These magnetometer stations lie within a narrow magnetic latitude but cover an extensive range (nearly 180 deg) of longitude.

Used Magnetometer stations

Station code	Geo lat.	Geo lon.	CGM lat.	CGM lon.	Instrument
CONT	65.754	248.750	72.82	304.82	CARISMA
SKT	65.42	307.10	70.98	36.66	Greenland
GHB	64.17	308.27	69.52	37.32	Greenland
HOR	77.00	15.60	74.13	109.59	IMAGE

Table 8.1: Geographic and geomagnetic coordinates of Magnetometer stations.

8.2.2 The Event of October 06, 2006 (16:00-18:00 UT)

Magnetometer stations that lie within the red lines shown in Figure 7.14 were chosen to be analysed in more detail. The following magnetometer stations are located within the field of view of one of these radars: Rankin Inlet (RANK) - Saskatoon; Umanaq/Uummannaq (UMQ) - Goose Bay. Figure 8.3 shows the time series for the stations. The time series data from 16:00 to 18:00 UT were Fourier analysed to obtain the power spectra. Some other magnetometer stations within the field of view do not have data while others do not have a significant peak in the 3.2-3.5 mHz band. Those magnetometer stations are not included in the study. The shading highlights peaks in the 3.2-3.5 mHz frequency band, which confirms the Pc5 pulsation event observed by these SuperDARN radars as shown in Figure 8.4. The event observed using the Automated Pulsation Finder appears in other radars and magnetometer chains is a field line resonance, having an H- component amplitude peak and associated phase across the resonant magnetic latitude.

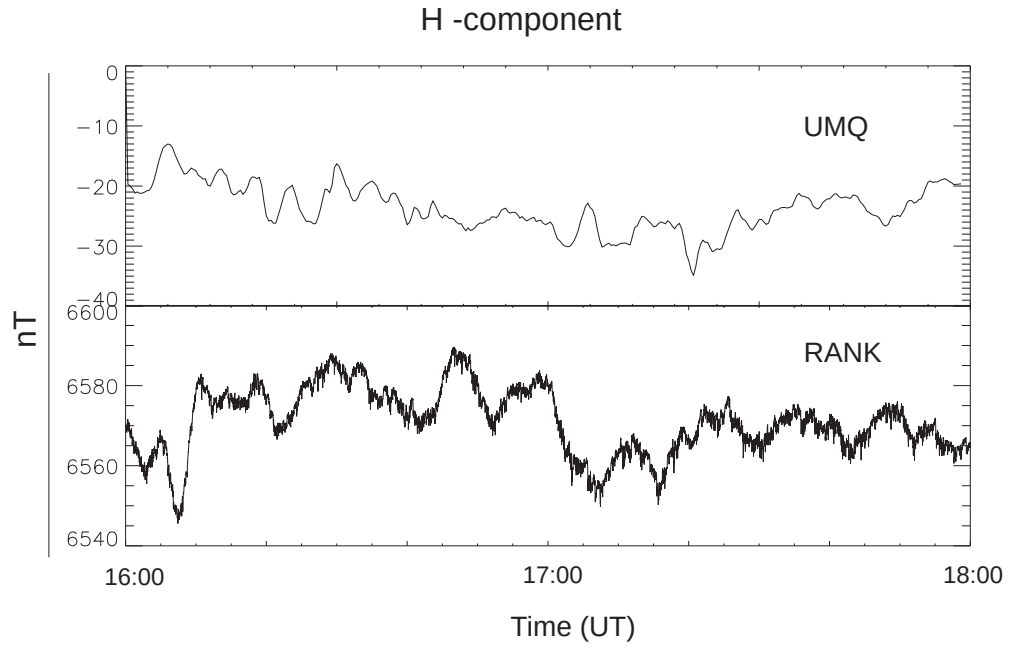

Figure 8.3: Time series observed from RANK(CARISMA) and UMQ (Greenland).

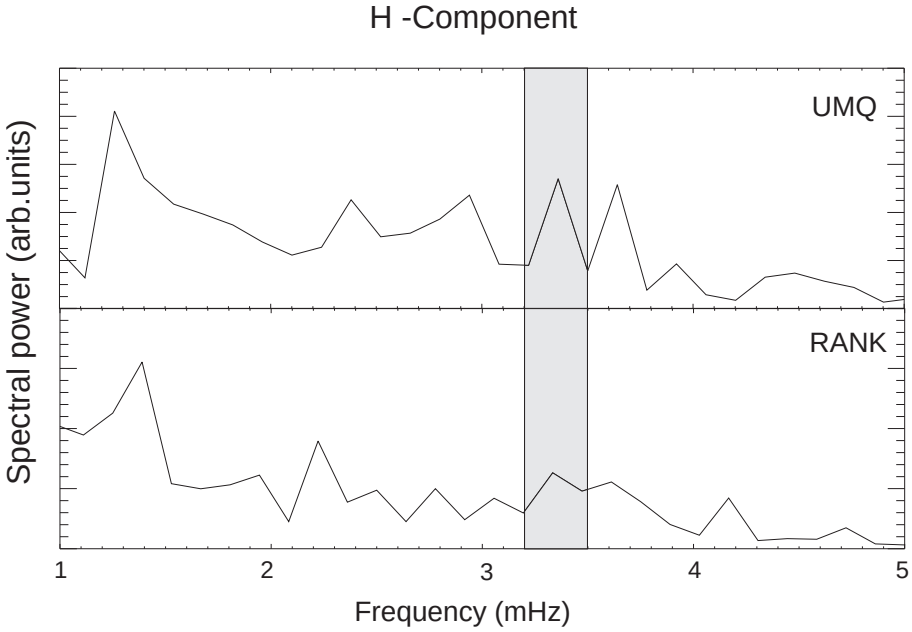

Figure 8.4: The corresponding spectral power for the above magnetometer stations.

The geographic and geomagnetic coordinates of the magnetometer stations used in this study are shown in Table 8.2. These magnetometer stations lie within a narrow magnetic latitude range but cover an extensive range (nearly 180 deg) of longitude.

Used magnetometer

Station code	Geo lat.	Geo lon.	CGM lat	CGM lon	Instrument
UMQ	70.68	307.87	75.97	41.87	Greenland
RANK	62.824	267.890	72.22	335.97	CARISMA

Table 8.2: Geographic and geomagnetic coordinates of Magnetometer stations.

8.2.3 The Event of Septmber 14, 2006 (18:00-20:00 UT)

Unfortunately, in this event, there were few magnetometer stations in the radars field of view and the stations that did fulfill this criterion, do not show significant peaks.

8.3 Magnetometer chains position in the magnetosphere

During the event of October 2006 between 20:00 to 22:00 UT interval the CARISMA, Greenland and IMAGE magnetometer networks were located in the evening (16:00-18:00), (17:00-19:00) and nightside (21:00-23:00) sectors in local time (LT), respectively in the magnetosphere. During the event of October 2006 between 16:00 to 18:00 UT, the CARISMA, Greenland and IMAGE magnetometer networks were located in the dayside (12:00-14:00), (13:00-15:00) and evening (17:00-19:00) sectors in local time (LT) in the magnetosphere.

Multiple radar data allowed us to investigate the spatial behaviour of the wave. Magnetometer observations have confirmed this field line resonances (FLRs) are toroidal mode waves with magnetospheric magnetic perturbations in the azimuthal direction. Due to the rotation effect of the ionosphere the large ionospheric perturbations on the ground are observed in the magnetic H- component [27]. Similarly, poloidal mode waves are characterised by magnetic perturbations in the radial direction which translates to a large perturbation observed in the magnetic D- component in ground magnetometer data. However, no ultra low frequency wave is purely Alfvén in nature; there will always be an accompanying compressional mode component. When identifying field line resonance signatures, one must take into account both the amplitude of H or D component and associated phase change.

8.4 Summary

The magnetometer data-set have been used to confirm pulsations. The magnetometer stations that are within the field of view of the radars and those in the magnetic latitude of radars, have shown some peaks. The H-component peak in both events dominated over D-component. We did not show the D-component because we did not observe the significant peaks although we have seen the amplitude. These peaks have shown characteristic features of the field line resonances and confirm our determination as such using radar data. More discussion about field line resonances including amplitude and associated phase changes is presented in Chapter 9.

Chapter 9

Complex demodulation

9.1 Introduction

In order to analyse the instantaneous characteristics of the signal we applied complex demodulation technique to determine the analytic signal [8]. Bandwidth frequency (Frequency band) in the Doppler velocity and magnetometer spectrum were used in complex demodulation. The analytic signal consists of the envelope, inside of which is the filtered oscillation and this is called the wave-packet structure. This allows the examination of the variation with time of the instantaneous amplitude and phase of a selected frequency band.

The amplitude and phase of the narrowband resonances were determined by the method of complex demodulation whereby the data were bandpass filtered and an analytic signal was determined. The analytic signal $A(t)$ for a time series $f(t)$ is given by

$$A(t) = f(t) - iF(t) \tag{9.1}$$

where $F(t)$ is the Hilbert transform of $f(t)$[9] defined in the usual manner

$$F(t) = \frac{1}{\pi} \int_{\infty}^{\infty} \frac{f(x)}{x - t} dx \tag{9.2}$$

Plotting the amplitude as a function of time gives the envelope of the signal which is called wave packet structure. Information about the amplitude is useful for studying the wave-packet structure of the pulsations as shown in the Figures below and the structure of pulsations as shown in Chapter 7 in Figures 7.4 and 7.21.

In this chapter, we discuss the complex demodulation for the three identified Pc5 pulsation events highlighted using the Automated Pulsation Finder.

9.2 Complex demodulation applied to Pc5 pulsations

This method is an ideal tool for studying instantaneous values of pulsation amplitude, phase and polarization of the selected frequency band.

9.2.1 The Event of October 06, 2006 (20:00-22:00 UT)

9.2.1.1 Wave packet structure

In the analysis of the resonance frequency band 2.2-2.5 mHz, the analytic signal was calculated from different beams and range gates of the radars where a given field line resonance was maximum as shown in Figures 9.1 (Goose Bay) and 9.2 (Saskatoon). Similar analysis of Pykkvibaer radar was performed but not shown here.

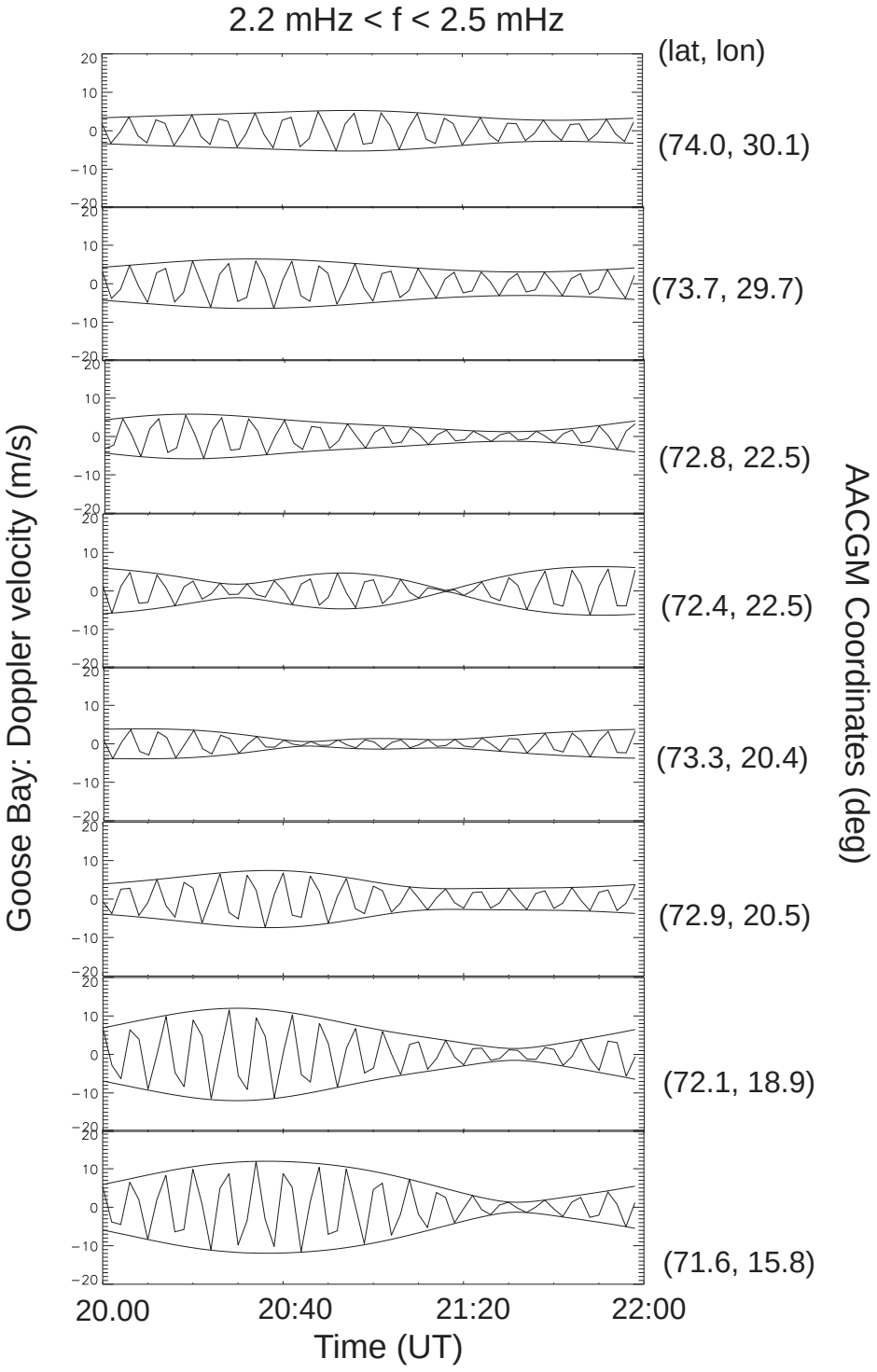

Figure 9.1: Stack plot of the analytic signal amplitude and its envelopes for various beams and range gates of the Goose Bay radar. The magnetic coordinates at the centre of each beam-range gate 'cell' are given on the right hand side.

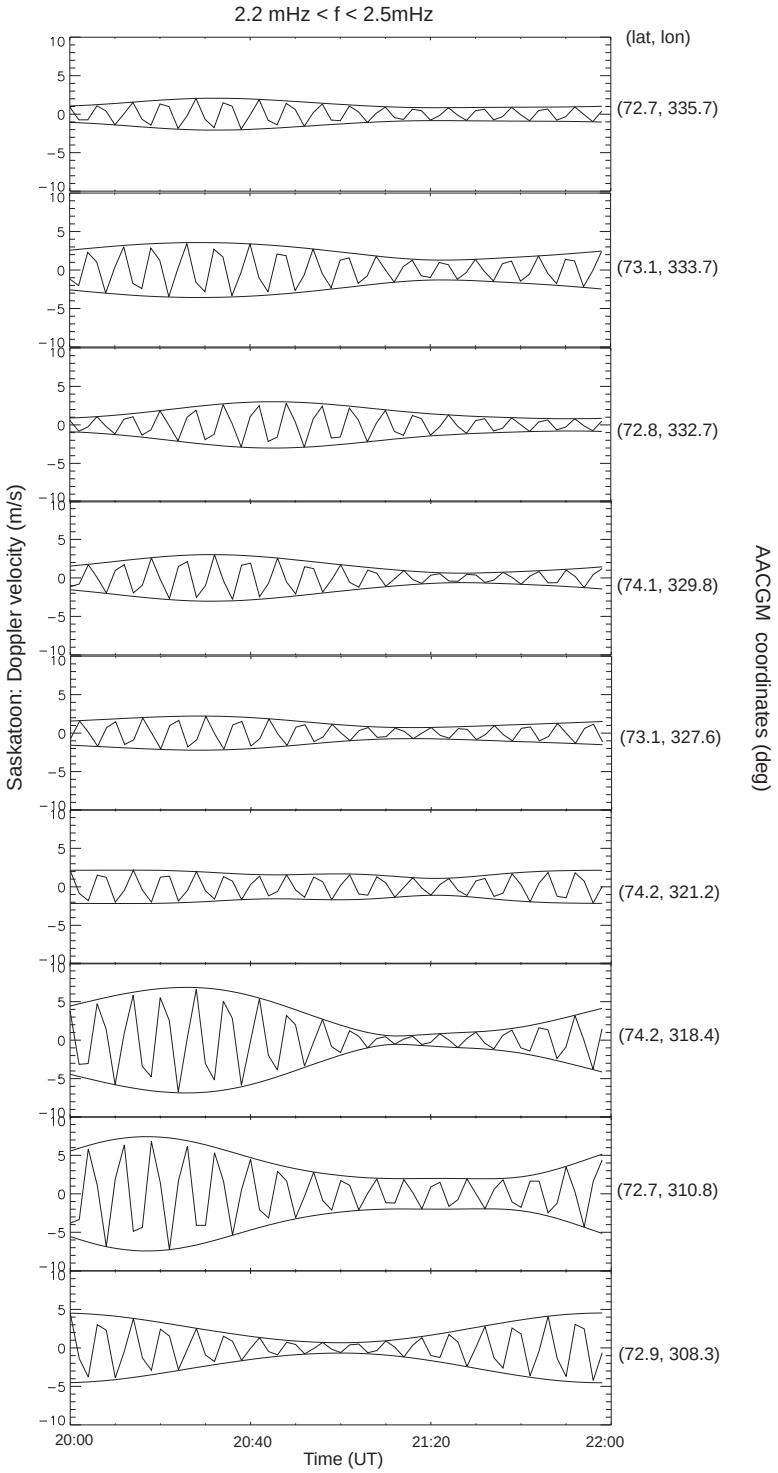

Figure 9.2: Stack plot of the analytic signal amplitude and its envelopes for various beams and range gates of the Saskatoon radar. The magnetic coordinates at the centre of each beam-range gate 'cell' are given on the right hand side.

9.2.1.2 Azimuthal wave number m

An important characteristic of Pc5 pulsations is the azimuthal wave number, m, which presents a relative change in phase with longitude. The phase of the resonance was measured across the field of view at constant magnetic latitude yielding a phase versus longitude relationship as shown in Figures 9.3, 9.4 and 9.5. The slopes of these plots yield the azimuthal wave number, m: 12 ± 2.1 (Saskatoon), 13 ± 2.9 (Goose Bay) and 19 ± 5.0 (Pykkvibaer). The m value and the resonance frequency were used to calculate the azimuthal phase velocities. The m number changes as we cross magnetic longitude. The azimuthal phase velocity is given by $v = \frac{2\pi f R cos\lambda}{m}$, where f is the ULF wave frequency, λ is the geomagnetic latitude, R is Earth's radius and m is the azimuthal wave number. These slopes correspond to westward phase velocities of ~ 2.2, ~ 2.0 and ~ 1.4 km/s, respectively in the ionosphere. This method was previously employed by Fenrich and Samson [22].

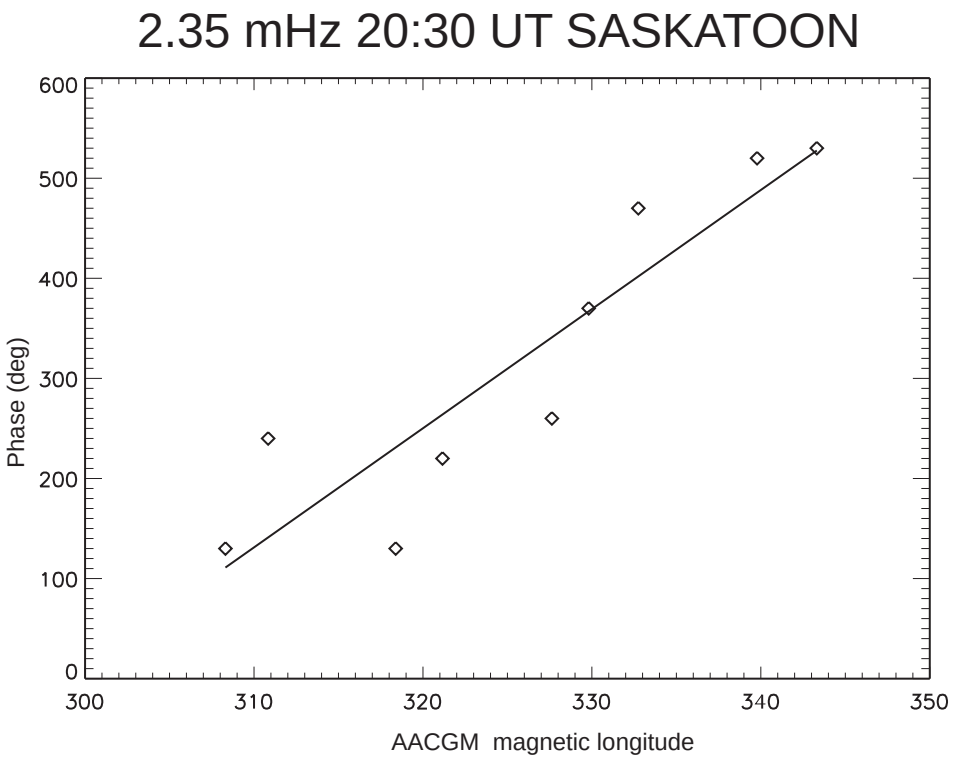

Figure 9.3: Plot of phase versus longitude measured at 20:30 UT for the 2.35 mHz frequency. The slope of this relation yields the azimuthal wave number 12 ± 2.1 correspond to a westward phase velocity at the ionosphere.

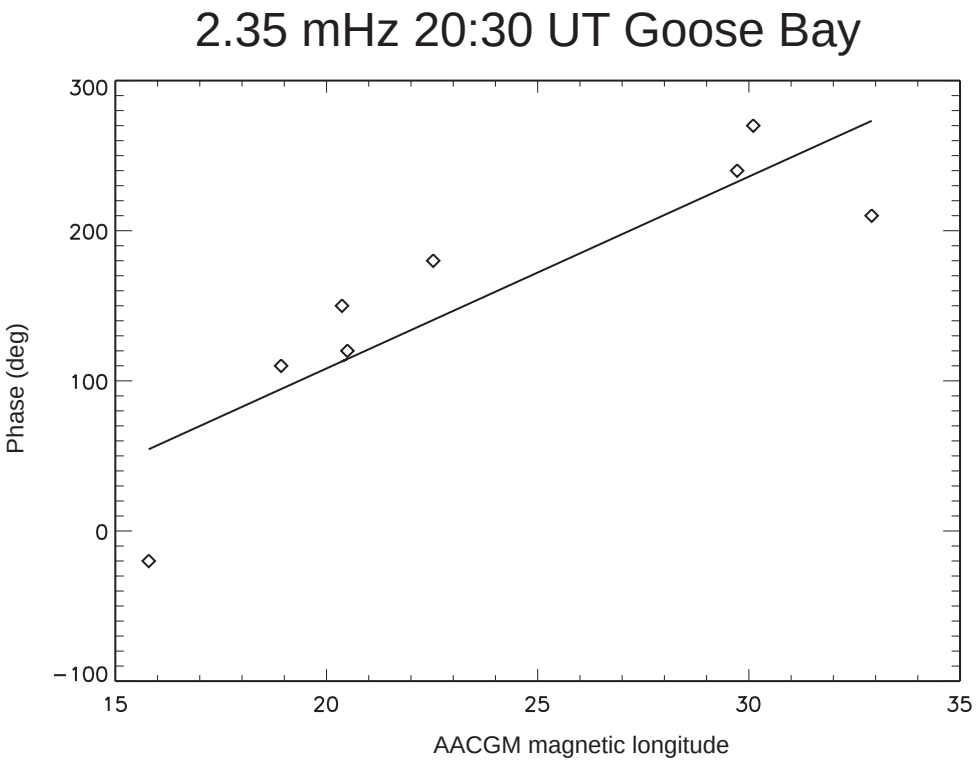

Figure 9.4: Plot of phase versus longitude measured at 20:30 UT for the 2.35 mHz frequency. The slope of this relation yields the azimuthal wave number 13±2.9 correspond to a westward phase velocity at the ionosphere.

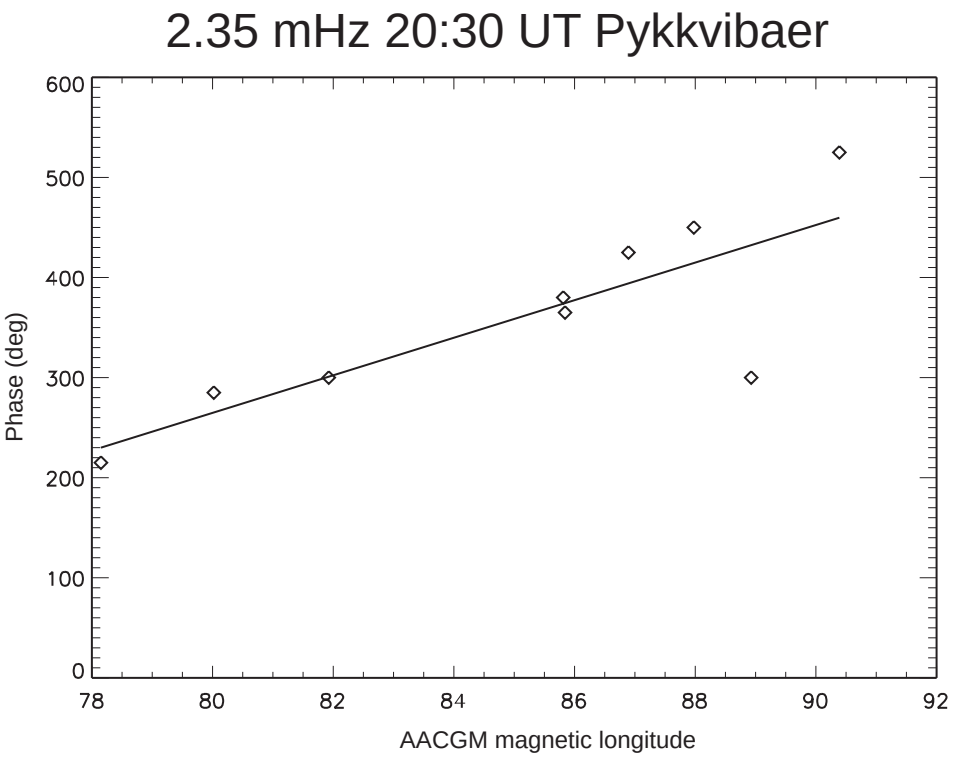

Figure 9.5: Plot of phase versus longitude measured at 20:30 UT for the 2.35 mHz frequency. The slope of this relation yields the azimuthal wave number 19±5.0 correspond to a westward phase velocity at the ionosphere.

9.2.2 The Event of October 06, 2006 (16:00-18:00 UT)

9.2.2.1 Wave packet structure

In the analysis of the resonance frequency band 3.2-3.5 mHz, the analytic signal was calculated from different beams and range gates of the radars where a given field line resonance was maximum as shown in Figures 9.6 (Goose Bay), 9.7 (Saskatoon) and 9.8 (Pykkvibaer).

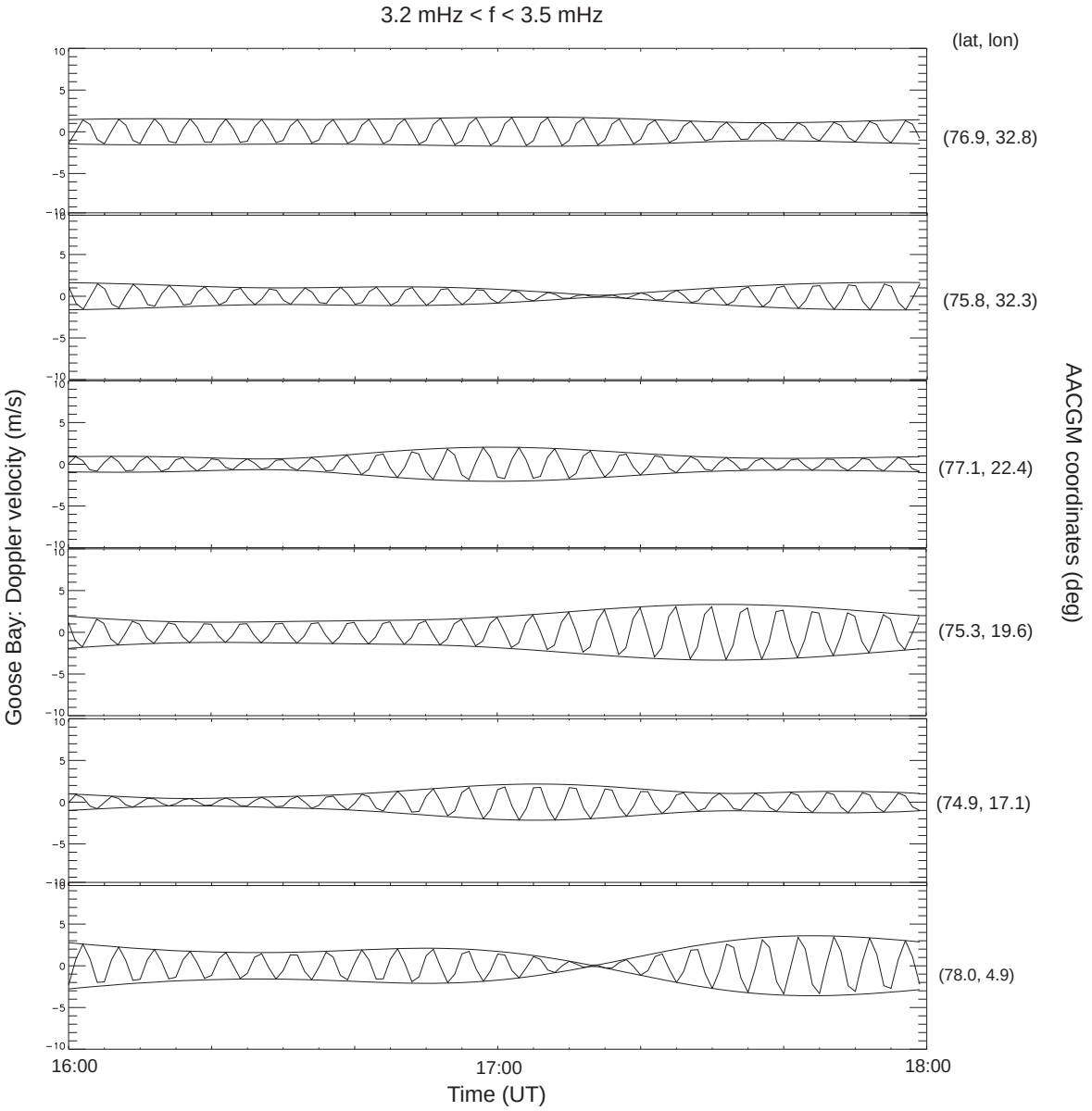

Figure 9.6: Stack plot of the analytic signal amplitude and its envelopes for various beams and range gates of the Goose Bay radar. The magnetic coordinates at the centre of each beam-range gate 'cell' are given on the right hand side.

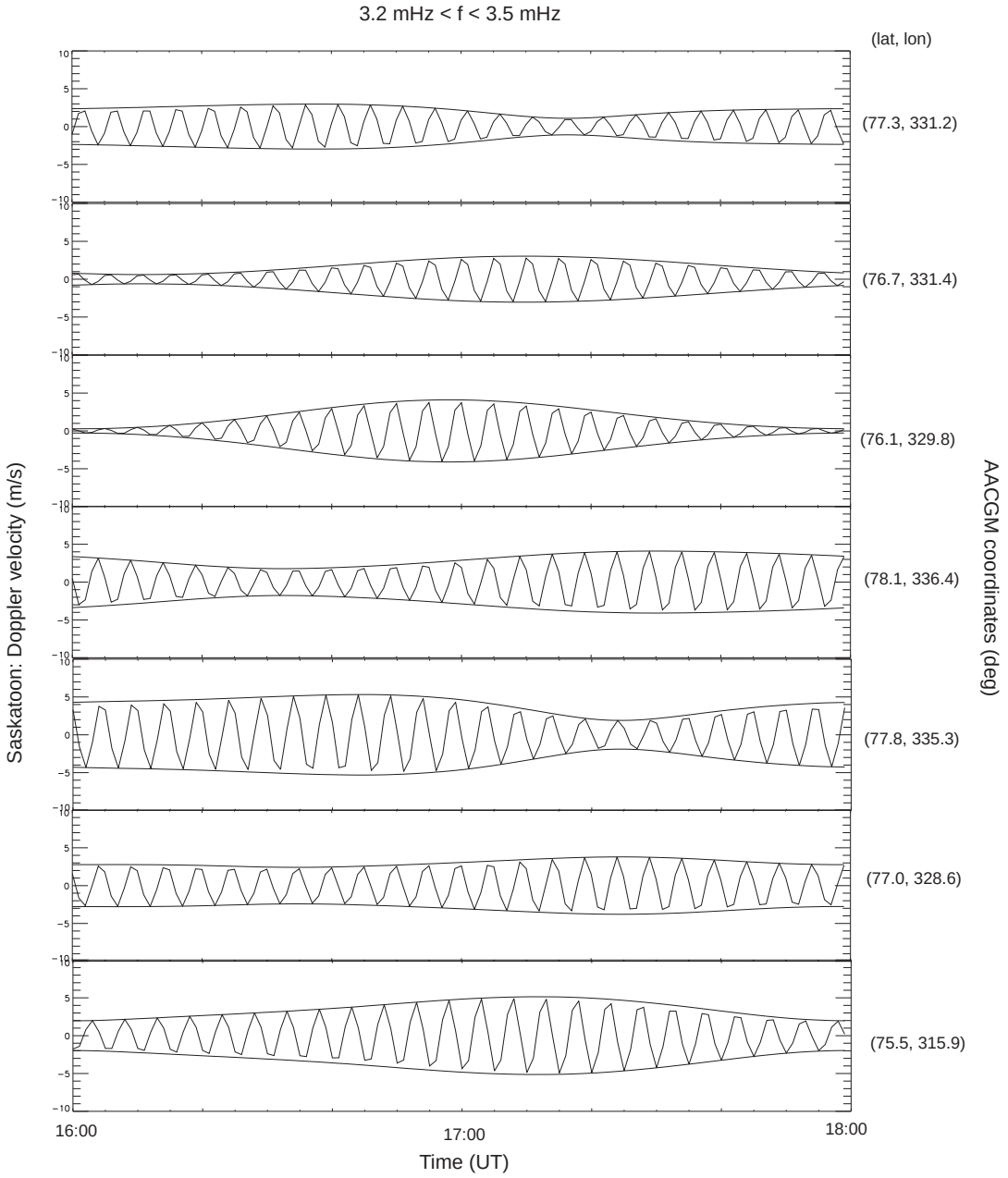

Figure 9.7: Stack plot of the analytic signal amplitude and its envelopes for various beams and range gates of the Saskatoon radar. The magnetic coordinates at the centre of each beam-range gate 'cell' are given on the right hand side.

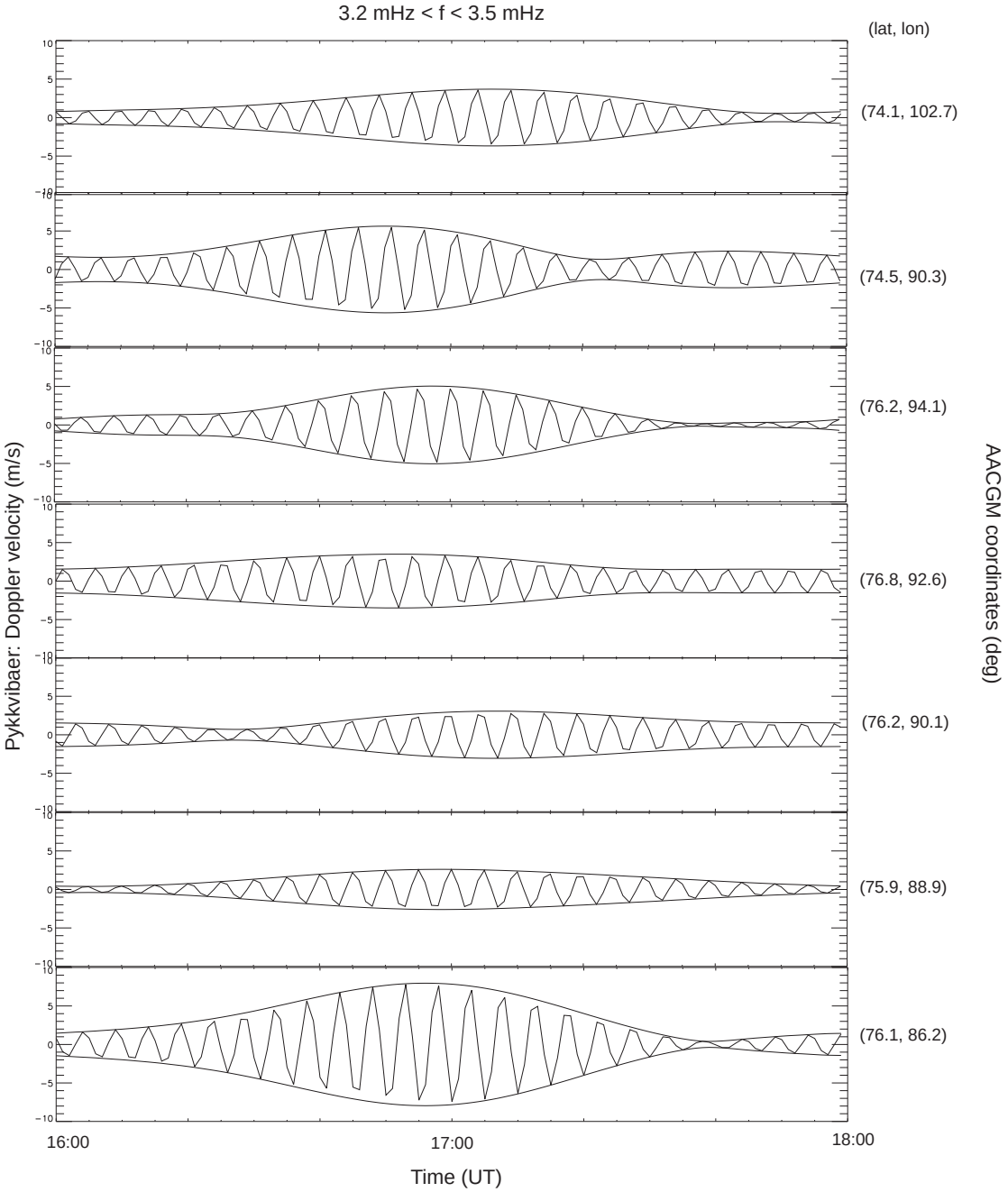

Figure 9.8: Stack plot of the analytic signal amplitude and its envelopes for various beams and range gates of the Pykkvibaer radar. The magnetic coordinates at the centre of each beam-range gate 'cell' are given on the right hand side.

9.2.2.2 Azimuthal wave number m

The phase of the resonance was measured across the field of view at constant magnetic latitude, yielding phase versus longitude relations as shown in Figures 9.9, 9.10 and 9.11. The slopes of these relations yield the azimuthal wave number, m: 9 ± 2.3 (Goose Bay), 7 ± 3.2 (Saskatoon) and 9 ± 4.3 (Pykkvibaer), which correspond to westward phase velocities of ~ 3.4, ~ 4.4 and ~ 3.4 km/s, respectively at the ionosphere.

The m value and the resonance frequency were used to calculate the azimuthal phase velocities. The m number values show some changes and consistency in this event in all radars.

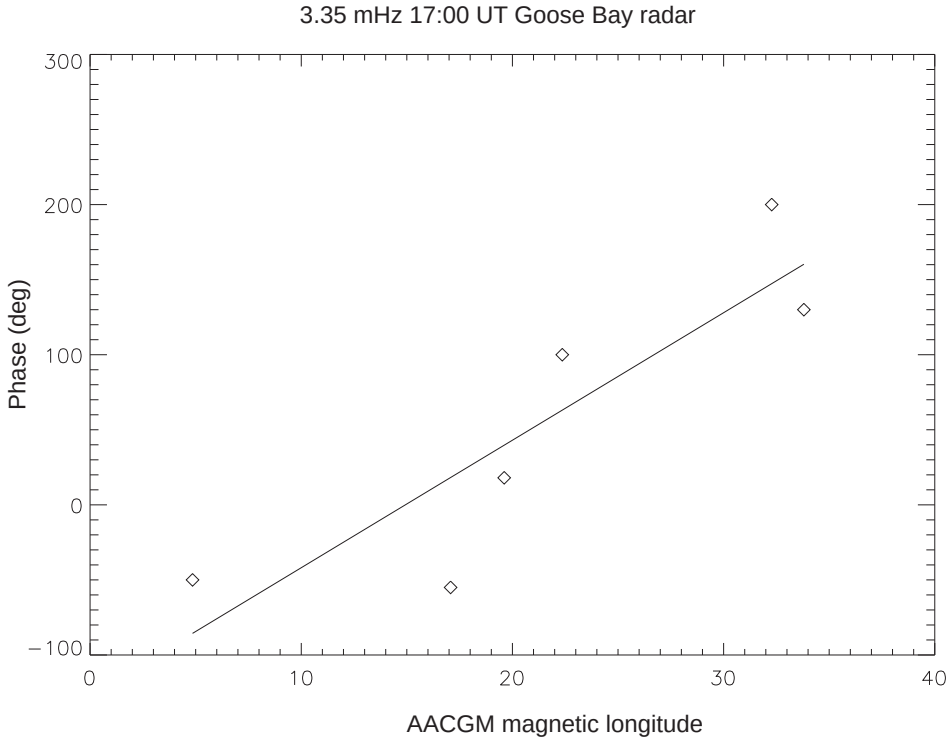

Figure 9.9: Plot of phase versus longitude measured at 17:00 UT for the 3.35 mHz frequency. The slope of this relation yields the azimuthal wave number 9±2.3 correspond to a westward phase velocity at the ionosphere.

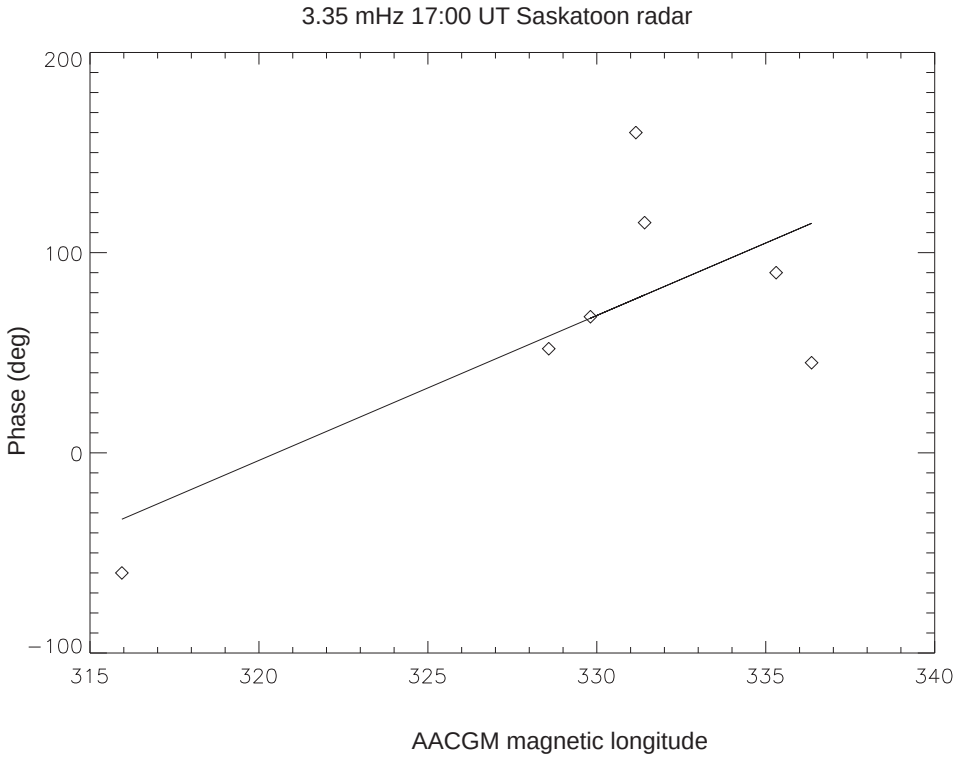

Figure 9.10: Plot of phase versus longitude measured at 17:00 UT for the 3.35 mHz frequency. The slope of this relation yields the azimuthal wave number 9±3.2 correspond to a westward phase velocity at the ionosphere.

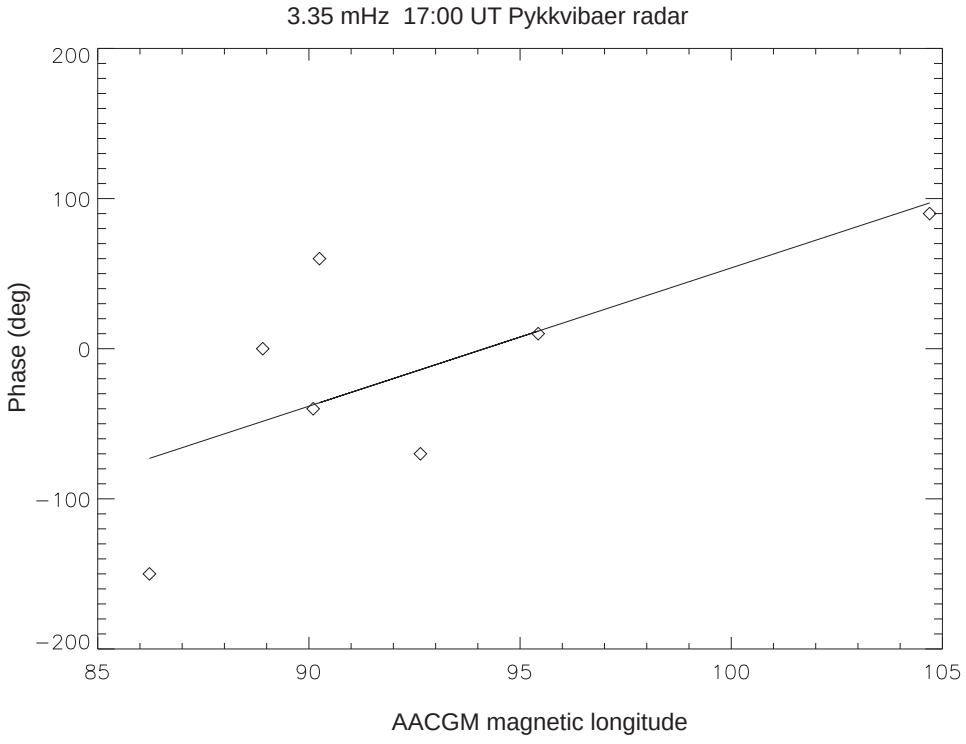

Figure 9.11: Plot of phase versus longitude measured at 17:00 UT for the 3.35 mHz frequency. The slope of this relation yields the azimuthal wave number 9±4.3 correspond to a westward phase velocity at the ionosphere.

9.2.3 The Event of Septmber 14, 2006 (18:00-20:00 UT)

9.2.3.1 Wave packet structure

In the analysis of the resonance frequency band 1.4-1.7 mHz, the analytic signal was calculated from different beams and range gates of the radars where a given field line resonance was maximum as shown in Figures (Goose Bay) and (Saskatoon).

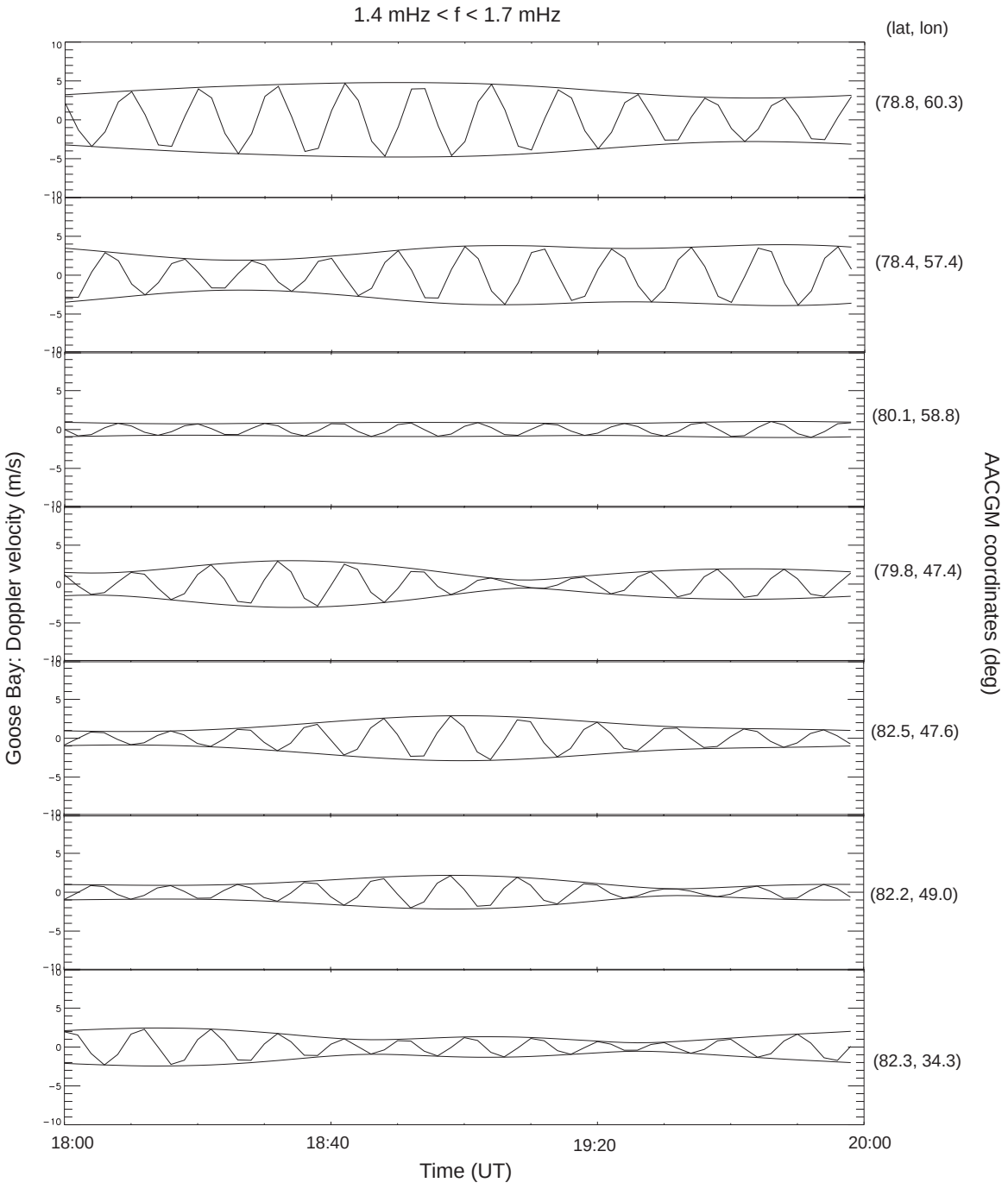

Figure 9.12: Stack plot of the analytic signal amplitude and its envelopes for various beams and range gates of the Goose Bay radar. The magnetic coordinates at the centre of each beam-range gate 'cell' are given on the right hand side.

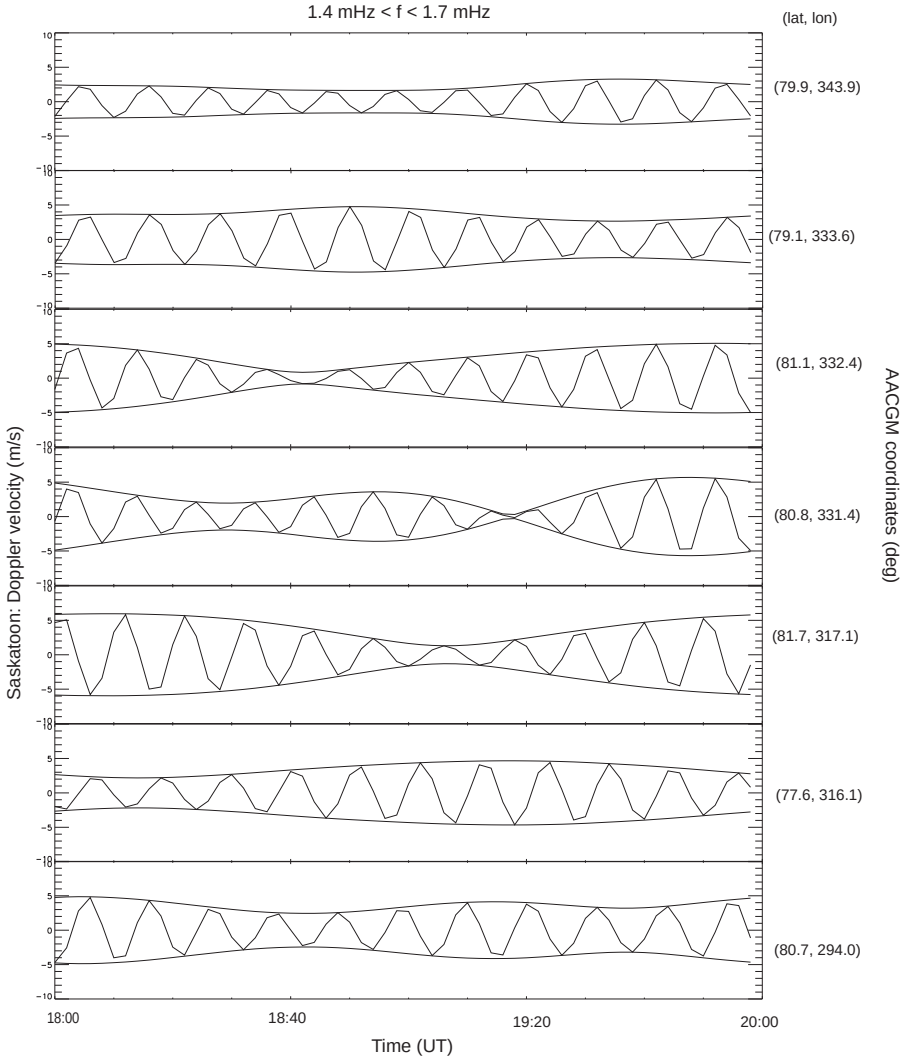

Figure 9.13: Stack plot of the analytic signal amplitude and its envelopes for various beams and range gates of the Saskatoon radar. The magnetic coordinates at the centre of each beam-range gate 'cell' are given on the right hand side.

9.2.3.2 Azimuthal wave number m

The phase of the resonance was measured across the field of view at constant magnetic latitude yielding phase versus longitude relations as shown in Figures 9.14 and 9.15. The slopes of these relations yield the azimuthal wave number, m: 9 ± 4.1 (Goose Bay), 9 ± 2.4 (Saskatoon), which correspond to westward phase velocities of $\sim$ 1.2 and $\sim$ 1.2 km/s, respectively in the ionosphere.

The m value and the resonance frequency were used to calculate the azimuthal phase velocities. The m number values show consistency in this event in all radars.

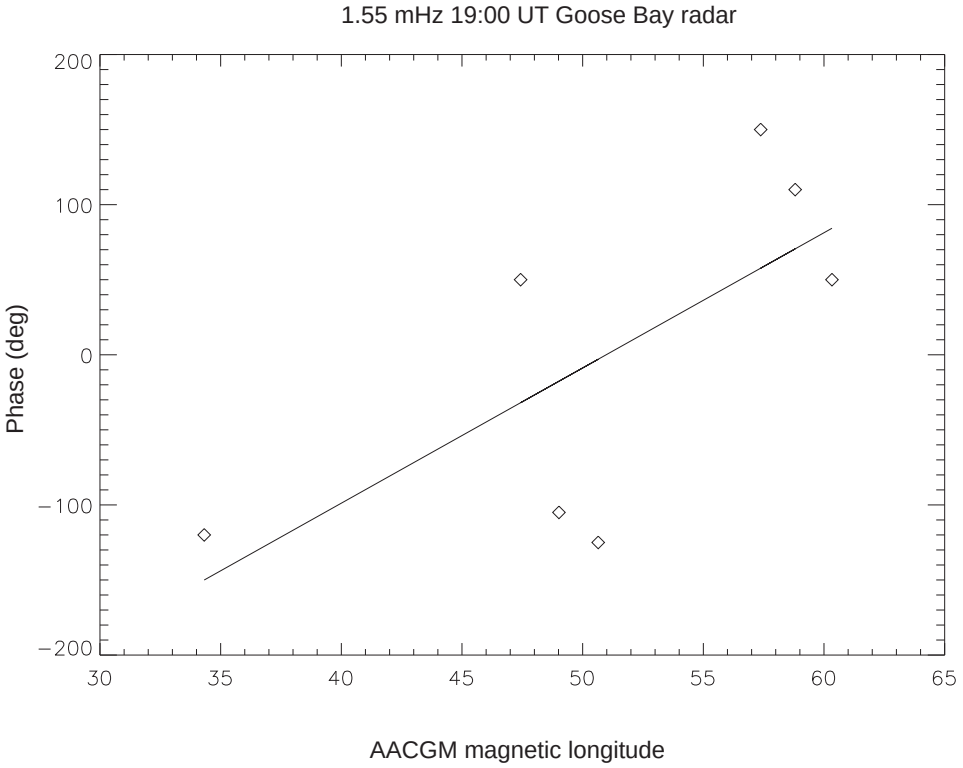

Figure 9.14: Plot of phase versus longitude measured at 19:00 UT for the 1.55 mHz frequency. The slope of this relation yields the azimuthal wave number 9±4.1 correspond to a westward phase velocity at the ionosphere.

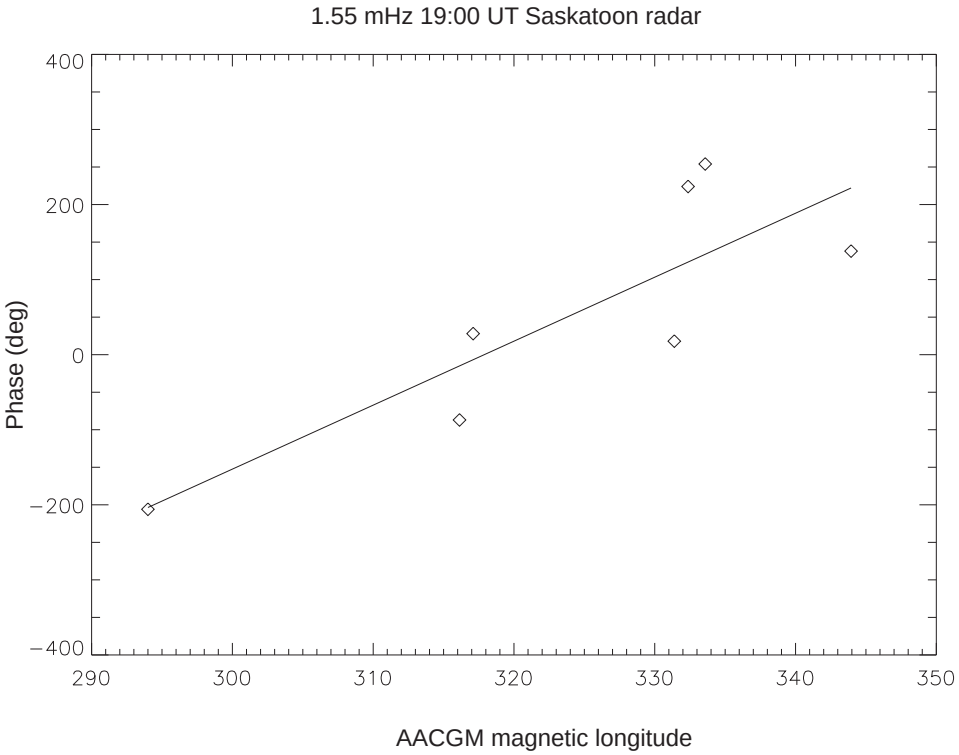

Figure 9.15: Plot of phase versus longitude measured at 19:00 UT for the 1.55 mHz frequency. The slope of this relation yields the azimuthal wave number 9±2.4 correspond to a westward phase velocity at the ionosphere.

9.2.4 Azimuthal wave number m from magnetometer data

Figures 9.16 and 9.17 show the filtered oscillation and its envelope and their phase for SKT and GHB (part of the Greenland network which lies under the field of view of Goose Bay), respectively. The resonance frequency band 2.2-2.5 mHz were used complex demodulation. The selected magnetometer stations have a peak in the frequency band 2.2-2.5 mHz. The signal has a packet structure with amplitude growing and decaying with time. In some cases, the phase may change abruptly between packets where amplitude is small.

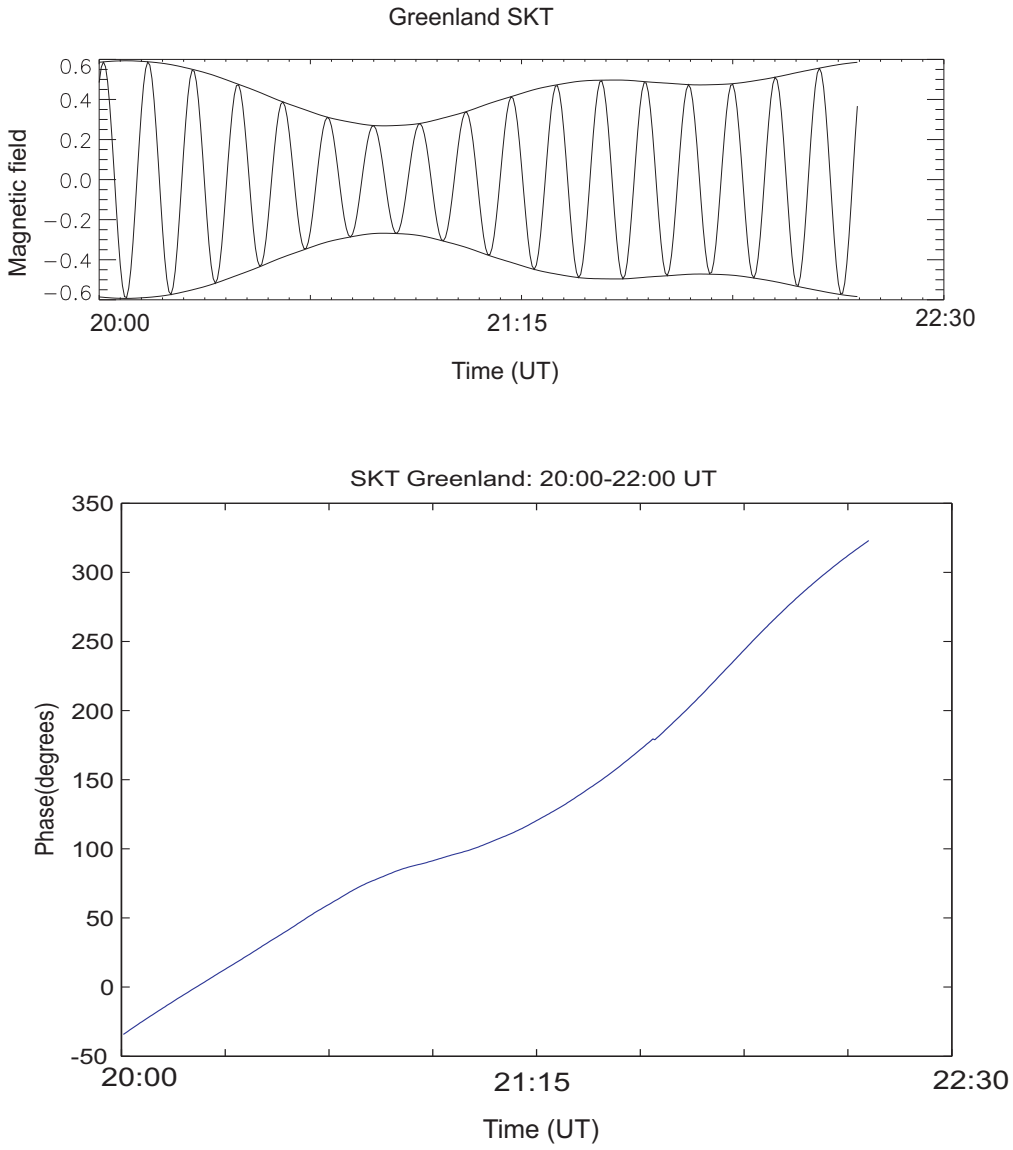

Figure 9.16: Filtered oscillation and its envelope and their phase for SKT station from Greenland.

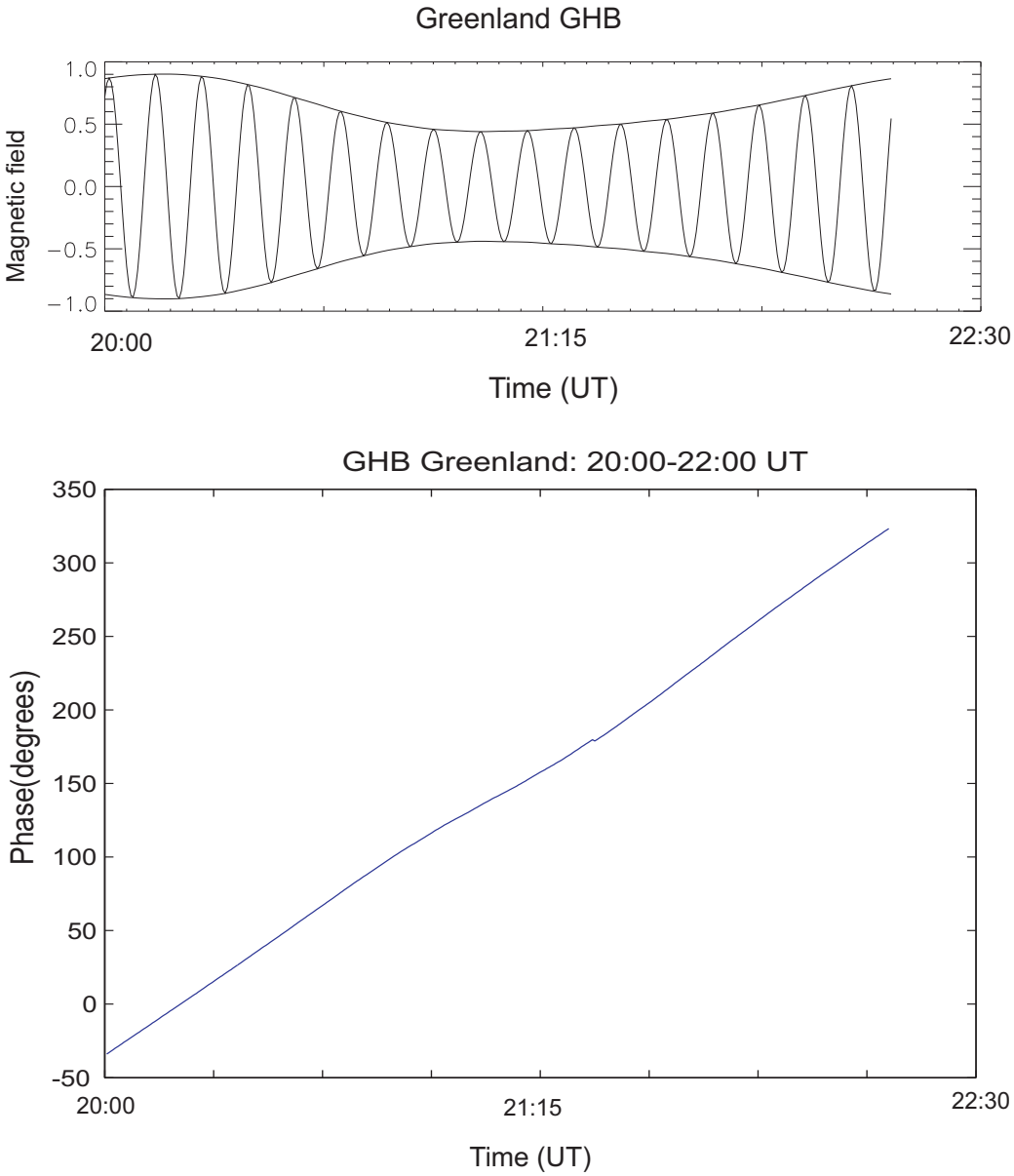

Figure 9.17: Filtered oscillation and its envelope and their phase for GHB station from Greenland.

In magnetometer data we are using phase difference to observe the azimuthal wave number m. The azimuthal wave number value is calculated using differenes in the H-component phase. The values are given by: $m = \frac{\Delta\phi}{\Delta\lambda}$, where $\Delta\phi$ is the phase difference of the H-component between two stations and $\Delta\lambda$ is their geomagnetic longitude difference. The coordinates of the relevant stations are provided in Table 8.1. We used the above magnetometer stations (GHB and SKT) to calculate the azimuthal wave number m and we observed $m = 11$. The positive m values represent waves with westward phase propagation while negative m values represent waves with eastward phase propagation. The m value of ~ 11 represents wave with westward phase propagation.

9.3 Summary

The resonance frequencies first observed in a radar data using the Automated Pulsation Finder, also appear in other radars, but not with the same dominant peak. The selected beams and range gates in all four radars analysed here show significant peaks. During the event of October 06 2006 between 20:00 to 22:00 UT, the wave number m increases from 12, 13 to 19 as one moves eastward across the field of view. It is not surprising that the m value is different across the field of view (fov) because the constant m value would assume cylindrical symmetry. There is no reason to assume the wave would have this property. These m values correspond with westward phase velocities at the ionosphere. During the event of 06 October 2006 between 16:00 to 18:00 UT, m values show changes and some consistency as one moves across the field of view in all the three radars, which correspond with westward phase velocities at the ionosphere. During the event of 14 September 2006 between 18:00 to 20:00 UT, the wave number m values show the good consistency as one moves the field of view. All these m values correspond with westward phase velocities at the ionosphere. The observed azimuthal wave number m from magnetometer stations are smaller than azimuthal wave numbers observed from SuperDARN radars. In general, the azimuthal wave values deduced from ground measurements should be smaller than the ionospheric radar values, and they are dependent on the ionospheric ULF amplitude and phase distribution in both latitude and longitude. This could be attributed to the ionospheric distribution of Hall current, having a finite scale size in longitude, which would imply then that azimuthal wave m numbers measured by ground-based magnetometers will be different compared with the values in the ionosphere [46].

Chapter 10

Conclusion

In this study, we have identified three Pc5 pulsation events from SuperDARN data using Automated Pulsation Finder. These Pc5 pulsation events were observed in the high latitude ionosphere ($\sim$ 70-82° magnetic latitude) by several SuperDARN HF radars and ground-based magnetometer chains. In a many instances, the ground-based magnetometer stations were within the field of view (fov) of the SuperDARN HF radars, which provided complementary data sets. These Pc5 pulsation events observed in the F-region plasma flows were detected in the measured line-of-sight Doppler velocities. We used the range-time summary plots to check pulsation activity. The ionospheric perturbations are visible in the range time summary plots as bands of alternating positive and negative (shades of blue and red) Doppler velocities with periods which are characteristic of Pc5 pulsations. The investigation of Pc5 pulsation events observed by Automated Pulsation Finder was extended to other radars in the same magnetic latitudes. The observations for the selected events have been shown in Chapter 7. Ground-based magnetometer stations that lie within the field of view of the radars were chosen and analysed in more detail. The stations that are in the same magnetic latitude range as other stations but not in the field of view of the mentioned radars were chosen and analysed in more detail. The magnetometer stations, that were included in the study, have shown significant peaks at the same frequency band.

The structure of the Pc5 pulsations have been determined using latitude profiles of amplitude and phase along beam 10 of Goose Bay and along beam 2 of Pykkvibaer radars for the first two events. These plots provide evidence that the Pc5 pulsation events being investigated here are field line resonances (FLRs). Analysis of the Goose Bay and Pykkvibaer radar beams most aligned with the magnetic meridian demonstrates an amplitude peak over a narrow latitude range and associated phase change across resonance (see Figures 7.4 and 7.21).

The Pc5 pulsation events, identified as the field line resonances, were analysed in more detail using an analytic signal technique. The azimuthal wave number of the pulsation has been calculated using phase and longitude relationship for each radar included in the study. During the event of 06 October 2006 between 20:00 to 22:00 UT, the azimuthal

wave number m increased from 12, 13 and 19 as one moves eastward across the field of view. During the event of 06 October 2006 between 16:00 to 18:00 UT, m values have shown changes and consistency as one moves across the field of view for all the three radars. The m values show consistency for different radars as one moves across the field of view during the event of 14 September 2006 between 18:00 to 20:00 UT. Different radars do not necessary need to produce the same m because constant m value would assume cylindrical symmetry. There is no reason to assume the wave would have this property.

The observed m values and resonance frequencies were used to calculate the azimuthal phase velocities. The relatively low azimuthal wave numbers m appear to be understandable in purely MHD terms as for example Alfvén field line resonances driven by compressional fast mode [53], which in turn are probably excited by external sources. Field line resonances tend to have lower azimuthal wave number m values and thus often have external sources. In addition, pulsations excited by external source have phase velocities that are anti-sunward. However, in the instance of a Pc5 pulsation event on 06 October 2006 at 20:00-22:00 UT, the field line resonance is sunward propagating with a relatively high azimuthal wave number. This may be more consistent with drift resonance source. However, a resonance generation mechanism is more commonly associated with a compessional oscillation. It has been shown that the drift resonance can be associated with field line resonance in a study of a properties of high m Alfvén waves by Ozeke and Mann [43]. In their study, they developed a model that can explain the characteristics of high- m waves observed in the magnetosphere and can provide a possible explanation of their observed dawn-dusk asymmetry. The model predicted that the fundamental (N=0) resonance can excite Pc5 ULF waves over a continuous range of L shells, each with different m value, the lower m, the close to Earth the waves will be excited and the smaller their period will be. In their model they found that the waves driven by this resonance were similar to the properties of 'storm-time' Pc5 ULF waves observed by the satellites in the afternoon sector. It predicted that the waves will be excited once the protons on open orbits have left the magnetosphere and bump-on-tail distribution has been created at the open-closed orbit boundary.

The last two Pc5 pulsation events are propagating sunward with low azimuthal wave number m. The event of 14 September 2006 between 18:00 to 20:00 UT has shown a consistently low azimuthal wave number m in all the two radars and phase velocities. The low azimuthal wave number m values suggest that the pulsations are excited by external sources. However, the waves appear to propagate sunward. Eriksson et al.[20], have presented observations on the Pc5 pulsations with low azimuthal wave number m, which was consistent with a toroidal mode and the wave was propagating sunward. In their study, they mainly focus on measurements from the Cluster spacecraft. They used data from electric field and fluxgate magnetometer instrument. They also include solar wind observations from the ACE spacecraft. The solar wind speed was approximately 400 km/s during the interval, which shows that the event occurred during relatively quiet magneto-

sphere. The Pc5 pulsation was observed in the post-midnight magnetotail flank by Cluster spacecraft. The wave appeared propagation sunward which was established by the sign of the azimuthal wave number (postive sign) m. Previous studies have suggested the magnetotail source of Pc5 pulsations theoretically by Allan and Wright [7] and experimentally by Mathews et al.[37]. These tail-waveguide eigenmodes were thought to be generated by Earthward flows of the magnetotail plasma. The low azimuthal wave values propagating sunward could lead us to suspect the source in the magnetotail. This will be the subject of our following publication to be submitted in the near future.

10.1 Future work

We will embark on further investigation of the pulsation events presented in this thesis. An important question has not been attempted here: what is their generation mechanism? We intend to attempt to answer this question with the input of data from pertinent satellites in the solar wind, magnetopause and magnetotail. Stephenson and Walker [58] have studied the coherence between radar observations of field line resonances and discrete oscillations in the solar wind. They employed the multitaper analysis, which can help in determining the phase and amplitude coherence. In addition, Eriksson et al.[21] have reported correlated observations between HF radar and solar wind pressure oscillations. In another study conducted by Fenrich and Waters [23] reported a high degree of phase coherence between SuperDARN Kodiak HF radar and ACE density observations utilizing FFT and wavelet cross-phase measurements. We intend to do similar work, which might help us to identify the excitation mechanism of these pulsations.

Appendix A

Glossary

AACGM	Altitude Adjusted Corrected Geomagnetic
ACF	Autocorrelation function
APF	Automated Pulsation Finder
CANOPUS	Canadian Auroral Network for the Open Program Unified Study
CARISMA	Canadian Array for Realtime Investigations of Magnetic Actvity
CCW	Counter Clockwise
CGM	Corrected Geomagnetic
DARN	Dual Auroral Radar Network
FFT	Fast Fourier Transform
FIT	extension of the file containing the ACF fitted parameters
HF	High Frequency
IAGA	International Association of Geomagnetic and Aeronomy
IDL	Interactive Data Language
IMAGE	International Monitor for Auroral Geomagnetic Effects
MHD	Magnetohydrodynamics
PACE	Polar Anglo-American Conjugate Experiment
RF	Radio Frequency
STARE	Scandinavian Twin Auroral Radar Experiment
SuperDARN	Super Dual Auroral Radar Network

UT	Universal Time
WKBJ	Wentzel-Kramers-Brillouin-Jeffreys

Appendix B

Symbols

ρ	Density
$\mathbf{v} = v_x\hat{\mathbf{x}} + v_y\hat{\mathbf{y}} + v_z\hat{\mathbf{z}}$	Perturbation velocity
p	Pressure
B	Magnetic field strength
$\mathbf{B}$	Magnetic field vector
$\mathbf{E}$	Electric field vector
μ_0	Permeability of free space
γ	Ratio of specific heats
$\mathbf{b} = b_x\hat{\mathbf{x}} + b_y\hat{\mathbf{y}} + b_z\hat{\mathbf{z}}$	Perturbed magnetic field
$\mathbf{V}_A$	Alfvén velocity
V_s	Sound velocity
i	imaginary operator
$\mathbf{k} = k_x\hat{\mathbf{x}} + k_y\hat{\mathbf{y}} + k_z\hat{\mathbf{z}}$	wave number
m	Azimuthal wave number
ω	perturbation frequency
v_T	Transverse component of the perturbation velocity
v_L	Longitudinal component of the perturbation velocity
ξ	Perturbation displacement normal to $\hat{\mathbf{y}}$ and $\mathbf{B}$
η	Perturbation displacement perpendicular to $\hat{\mathbf{x}}$ and $\mathbf{B}$

ψ	Generalised perturbation pressure
x_T	Turning point in the magnetosphere
x_R	Resonance point in the magnetosphere
ζ	x coordinate transformation near the turning and resonance points
$\mathbf{J}$	Current density vector
μ	dipole coordinate in the direction of the magnetic field
ν	dipole coordinate perpendicular to the magnetic field
λ	geomagnetic latitude
K_0	Resonant normalised frequency

References

[1] CARISMA magnetometer array online. http://www.cssdp.ca. or www.carisma.ca. Accessed 2013.

[2] Greenland magnetometer array online. http://www.space.dtu.dk. Accessed 2013.

[3] IMAGE magnetometer array online. http://space.fmi.fi/image. Accessed 2013.

[4] Magnetosphere online. https://perswww.kuleuven.be/ 0052182/weather/les2/node4.html. Accessed 2013.

[5] SuperDARN Radar locations online. http://www.superdarn.jhaupl.edu. Accessed 2013.

[6] W Allan, SP White, and El M Poulter. Impulse-excited hydromagnetic cavity and field-line resonances in the magnetosphere. *Planetary and space science*, 34(4):371–385, 1986.

[7] W Allan and Andrew N Wright. Magnetotail waveguide: Fast and alfvén waves in the plasma sheet boundary layer and lobe. *Journal of Geophysical Research*, 105(A1):317–328, 2000.

[8] D Beamish, HW Hanson, and DC Webb. Complex demodulation applied to Pi2 geomagnetic pulsations. *Geophysical Journal of the Royal Astronomical Society*, 58(2):471–493, 1979.

[9] RN Bracewell. *The Fourier transform and its applications*. McGraw-Hill New York, 1979.

[10] G Bryson, W Bristow, Parris T, and the SuperDARN Group at the Geophysical Institute at the university of Alaska Fairbanks. An introduction to Radar and the Super Dual Auroral Radar Network* online. http://www.superdarn.gi.alaska.edu/tutorials/index.html. Accessed 2013.

[11] L Chen and A Hasegawa. A theory of long-period magnetic pulsations: 1. Steady state excitation of field line resonance. *Journal of Geophysical Research*, 79(7):1024–1032, 1974.

[12] L Chen and A Hasegawa. On magnetospheric hydromagnetic waves excited by energetic ring-current particles. *Journal of Geophysical Research*, 93(A8):8763–8767, 1988.

[13] G Chisham, M Lester, SE Milan, MP Freeman, WA Bristow, A Grocott, KA McWilliams, JM Ruohoniemi, TK Yeoman, Peter Lawrence Dyson, et al. A decade of the super dual auroral radar network (SuperDARN): Scientific achievements, new techniques and future directions. *Surveys in Geophysics*, 28(1):33–109, 2007.

[14] G Chisham and IR Mann. A Pc5 ULF wave with large azimuthal wavenumber observed within the morning sector plasmasphere by sub-auroral magnetometer network. *Journal of Geophysical Research*, 104(A7):14717–14727, 1999.

[15] G Chisham and D Orr. A statistical study of the local time asymmetry of Pc5 ULF wave characteristics observed at midlatitudes by SAMNET. *Journal of Geophysical Research*, 102(A11):24339–24, 1997.

[16] WD Cummings, RJ O'sullivan, and PJ Coleman. Standing alfvén waves in the magnetosphere. *Journal of Geophysical Research*, 74(3):778–793, 1969.

[17] JW Dungey. Electrodynamics of the outer atmosphere. In *Physics of the Ionosphere*, volume 1, page 229, 1955.

[18] JW Dungey. The structure of the exosphere or adventures in velocity space. *In Geophysics: the Earth's Environment, eds. C Dewitt, J Hieblot and A Lebeau, Gordon and Breach,*, pages 505–550, 1963.

[19] M Engebretson, K-H Glassmeier, M Stellmacher, W J Hughes, and H Lühr. The dependence of high-latitude Pc5 wave power on solar wind velocity and on the phase of high-speed solar wind streams. *Journal of Geophysical Research*, 103(A11):26271–26283, 1998.

[20] PTI Eriksson, LG Blomberg, S Schaefer, and K-H Glassmeier. Sunward propagating Pc5 waves observed on the post-midnight magnetospheric flank. In *Annales Geophysicae*, volume 26, pages 1567–1579. Copernicus GmbH, 2008.

[21] PTI Eriksson, ADM Walker, and JAE Stephenson. A statistical correlation of pc5 pulsations and solar wind pressure oscillations. *Advances in Space Research*, 38(8):1763–1771, 2006.

[22] FR Fenrich, JC Samson, G Sofko, and RA Greenwald. ULF high-and low-m field line resonances observed with the Super Dual Auroral Radar Network. *Journal of Geophysical Research*, 100(A11):21535–21547, 1995.

[23] FR Fenrich and CL Waters. Phase coherence analysis of a field line resonance and solar wind oscillation. *Geophysical Research Letters*, 35(20), 2008.

[24] N Fukushima. Equivalence in ground geomagnetic effect of Chapman-Vestine's and Birkeland-Alfven's electric current-systems for polar magnetic storms(Chapman-Vestine and Birkeland-Alfven electric current systems equivalence in ground geomagnetic effect explained for polar magnetic storms). *Report of Ionosphere and Space Research in Japan*, 23:219–227, 1969.

[25] RA Greenwald, KB Baker, JR Dudeney, M Pinnock, TB Jones, EC Thomas, J-P Villain, J-C Cerisier, C Senior, C Hanuise, et al. DARN/SuperDARN. *Space Science Reviews*, 71(1-4):761–796, 1995.

[26] WJ Hughes. The effect of the atmosphere and ionosphere on long period magnetospheric micropulsations. *Planetary and Space Science*, 22(8):1157–1172, 1974.

[27] WJ Hughes. Hydromagnetic waves in the magnetosphere. *Reviews of Geophysics*, 21(2):508–520, 1983.

[28] WJ Hughes and DJ Southwood. The screening of micropulsation signals by the atmosphere and ionosphere. *Journal of Geophysical Research*, 81(19):3234–3240, 1976.

[29] JA Jacobs, Y Kato, S Matsushita, and VA Troitskaya. Classification of geomagnetic micropulsations. *Journal of Geophysical Research*, 69(1):180–181, 1964.

[30] L Kepko and HE Spence. Observations of discrete, global magnetospheric oscillations directly driven by solar wind density variations. *Journal of Geophysical Research*, 108(A6), 2003.

[31] M G Kivelson, J Etcheto, and J G Trotignon. Global compressional oscillations of the terrestrial magnetosphere: The evidence and a model. *Journal of Geophysical Research*, 89(A11):9851–9856, 1984.

[32] M G Kivelson and D J Southwood. Resonant ULF waves: A new interpretation. *Geophysical Research Letters*, 12(1):49–52, 1985.

[33] MG Kivelson and CT Russell. *Introduction to space physics*. Cambridge university press, 1995.

[34] EA Lee, IR Mann, TM Loto'aniu, and ZC Dent. Global Pc5 pulsations observed at unusually low L during the great magnetic storm of 24 March 1991. *Journal of Geophysical Research*, 112(A5), 2007.

[35] M Lester. HF coherent scatter radar observations of ionospheric convection during magnetospheric substorms. *Adv. Polar Upper Atmos. Res*, 14:179–201, 2000.

[36] LG Magnus. *An analysis of Pc5 pulsations observed in the SuperDARN data*. PhD thesis, School of Physics, University of KwaZulu-Natal, 2009.

[37] JT Mathews, IR Mann, IJ Rae, and J Moen. Multi-instrument observations of ulf wave-driven discrete auroral arcs propagating sunward and equatorward from the poleward boundary of the duskside auroral oval. *Physics of Plasmas*, 11(4):1250–1259, 2004.

[38] RA Mathie and IR Mann. Observations of Pc5 field line resonance azimuthal phase speeds: A diagnostic of their excitation mechanism. *Journal of Geophysical Research*, 105(A5):10713–10728, 2000.

[39] RA Mathie and IR Mann. On the solar wind control of Pc5 ULF pulsation power at mid-latitudes: Implications for MeV electron acceleration in the outer radiation belt. *Journal of Geophysical Research*, 106(A12):29783–29796, 2001.

[40] RA Mathie, IR Mann, FW Menk, and D Orr. Pc5 ULF pulsations associated with waveguide modes observed with the IMAGE magnetometer array. *Journal of Geophysical Research*, 104(A4):7025–7036, 1999.

[41] RL McPherron. Magnetic pulsations: their sources and relation to solar wind and geomagnetic activity. *Surveys in Geophysics*, 26(5):545–592, 2005.

[42] SH Mthembu, SB Malinga, ADM Walker, and L Magnus. Characterization of ultra low frequency (ULF) pulsations and the investigation of their possible source. In *Annales Geophysicae*, volume 27, pages 3287–3296, 2009.

[43] LG Ozeke and IR Mann. Modeling the properties of high-m Alfvén waves driven by the drift-bounce resonance mechanism. *Journal of Geophysical Research*, 106(A8):15583–15597, 2001.

[44] DB Percival and AT Walden. Spectral analysis for physical applications: multitaper and conventional univariate techniques (cambridge up, cambridge, uk). 1993.

[45] PV Ponomarenko, Frederick W Menk, and Colin L Waters. Visualization of ULF waves in SuperDARN data. *Geophysical Research Letters*, 30(18), 2003.

[46] PV Ponomarenko, CL Waters, MD Sciffer, BJ Fraser, and JC Samson. Spatial structure of ULF waves: Comparison of magnetometer and Super Dual Auroral Radar Network data. *Journal of Geophysical Research*, 106(A6):10509–10517, 2001.

[47] G Provan and TK Yeoman. A comparison of field-line resonances observed at the Goose Bay and Wick radars. In *Annales Geophysicae*, volume 15, pages 231–235. Springer, 1997.

[48] JM Ruohoniemi, RA Greenwald, KB Baker, and JC Samson. HF radar observations of Pc5 field line resonances in the midnight/early morning MLT sector. *Journal of Geophysical Research*, 96(A9):15697–15710, 1991.

[49] JC Samson, RA Greenwald, JM Ruohoniemi, TJ Hughes, and DD Wallis. Magnetometer and radar observations of magnetohydrodynamic cavity modes in the Earth's magnetosphere. *Canadian Journal of Physics*, 69(8-9):929–937, 1991.

[50] JC Samson, RA Greenwald, JM Ruohoniemi, TJ Hughes, and DD Wallis. Magnetometer and radar observations of magnetohydrodynamic cavity modes in the Earth's magnetosphere. *Canadian Journal of Physics*, 69(8-9):929–937, 1991.

[51] JC Samson, BG Harrold, JM Ruohoniemi, RA Greenwald, and ADM Walker. Field line resonances associated with MHD waveguides in the magnetosphere. *Geophysical Research Letters*, 19(5):441–444, 1992.

[52] JC Samson, JA Jacobs, and G Rostoker. Latitude-dependent characteristics of long-period geomagnetic micropulsations. *Journal of Geophysical Research*, 76(16):3675–3683, 1971.

[53] DJ Southwood. Some features of field line resonances in the magnetosphere. *Planetary and Space Science*, 22(3):483–491, 1974.

[54] DJ Southwood. A general approach to low-frequency instability in the ring current plasma. *Journal of Geophysical Research*, 81(19):3340–3348, 1976.

[55] DJ Southwood, JW Dungey, and RJ Etherington. Bounce resonant interaction between pulsations and trapped particles. *Planetary and Space Science*, 17(3):349–361, 1969.

[56] DJ Southwood and WJ Hughes. Theory of hydromagnetic waves in the magnetosphere. *Space Science Reviews*, 35(4):301–366, 1983.

[57] JAE Stephenson and ADM Walker. HF radar observations of Pc5 ULF pulsations driven by the solar wind. *Geophysical Research Letters*, 29(9):1297, 2002.

[58] JAE Stephenson and ADM Walker. Coherence between radar observations of magnetospheric field line resonances and discrete oscillations in the solar wind. In *Annales Geophysicae*, volume 28, pages 47–59, 2010.

[59] B Stewart. On the great magnetic disturbance which extended from August 28 to September 7, 1859, as recorded by photography at the Kew Observatory. *Philosophical Transactions of the Royal Society of London*, pages 423–430, 1861.

[60] Y Taroyan and R Erdélyi. Steady state excitation of field line resonances by global waveguide modes in the magnetosphere. *Journal of Geophysical research*, 108(A7):1301, 2003.

[61] ADM Walker. The Kelvin-Helmholtz instability in the low-latitude boundary layer. *Planetary and Space Science*, 29(10):1119–1133, 1981.

[62] ADM Walker. Radar studies of magnetosphere dynamics. *Astrophysics and Space Science*, 230(1-2):415–430, 1995.

[63] ADM Walker. The SHARE Radar at SANAE, Antarctica: Antarctic research. *South African Journal of Science*, 98:257–263, 2002.

[64] ADM Walker. Excitation of field line resonances by sources outside the magnetosphere. In *Annales Geophysicae*, volume 23, pages 3375–3388, 2005.

[65] ADM Walker. *Magnetohydrodynamic Waves in Geospace: The Theory of ULF Waves and Their Interaction With Energetic Particles in the Solar-Terrestrial Environment.* Institute of Physics Publishing Bristol and Philadephia, 2005.

[66] ADM Walker, RA Greenwald, WF Stuart, and CA Green. STARE auroral radar observations of Pc5 geomagnetic pulsations. *Journal of Geophysical Research*, 84(A7):3373–3388, 1979.

[67] ADM Walker, JM Ruohoniemi, KB Baker, RA Greenwald, and JC Samson. Spatial and temporal behavior of ULF pulsations observed by the Goose Bay HF radar. *Journal of Geophysical Research*, 97(A8):12187–12202, 1992.

[68] CL Waters, BG Harrold, FW Menk, JC Samson, and BJ Fraser. Field line resonances and waveguide modes at low latitudes: 2. A model. *Journal of Geophysical Research*, 105(A4):7763–7774, 2000.

[69] JA Wild, TK Yeoman, and CL Waters. Revised time-of-flight calculations for high-latitude geomagnetic pulsations using a realistic magnetospheric magnetic field model. *Journal of Geophysical Research*, 110(A11), 2005.

[70] AN Wright. Dispersion and wave coupling in inhomogeneous MHD waveguides. *Journal of Geophysical Research*, 99(A1):159–167, 1994.

[71] CWS Ziesolleck and DR McDiarmid. Auroral latitude Pc5 field line resonances: Quantized frequencies, spatial characteristics, and diurnal variation. *Journal of Geophysical Research*, 99(A4):5817–5830, 1994.